Electron Transfer in Solution: Nonadiabatic Dynamics and Applications to Catalysis

by

Michael G. Mavros

B.S., University of Florida (2011)

Submitted to the Department of Chemistry
in partial fulfillment of the requirements for the degree of

Doctor of Philosophy

at the

MASSACHUSETTS INSTITUTE OF TECHNOLOGY

June 2016

Author .....
Department of Chemistry
April 28, 2016

Certified by .....
Troy Van Voorhis
Haslam and Dewey Professor of Chemistry
Thesis Supervisor

Accepted by .....
Robert W. Field
Chairman, Departmental Committee on Graduate Students

This doctoral thesis has been examined by a Committee of the Department of Chemistry as follows:

Professor Jianshu Cao .....
Chairman, Thesis Committee
Professor of Chemistry

Professor Troy Van Voorhis .....
Thesis Supervisor
Haslam and Dewey Professor of Chemistry

Professor Moungi G. Bawendi .....
Member, Thesis Committee
Lester Wolfe Professorship in Chemistry

Electron Transfer in Solution: Nonadiabatic Dynamics and Applications to Catalysis

by

Michael G. Mavros

Submitted to the Department of Chemistry
on April 28, 2016, in partial fulfillment of the
requirements for the degree of
Doctor of Philosophy

Abstract

A mechanistic understanding of electron transfer in solution will advance our understanding of many chemical processes, including heterogeneous redox catalysis and photochemistry–processes which are fundamental in energy storage and solar energy conversion, among other applications. In this thesis, we first apply density functional theory (DFT) to study the mechanistic intermediates of the oxygen evolution reaction (OER) on metal-oxide redox catalysts. From these thermodynamic calculations, we are able to gain insight into catalytic design principles. Afterwards, we study nonadiabatic electron transfer in solution. After benchmarking various resummations of a fourth-order perturbation theory expansion of a generalized master equation memory kernel for the spin-boson model, we apply our theoretical understanding to study the short-time dynamics of electron transfer beyond the Condon approximation in aqueous iron(II) / iron(III) electron self-exchange. We discuss the application of this method to identify conical intersections in condensed-phase photochemistry. Finally, we examine the range of validity of electron couplings predicted by constrained density functional theory with configuration interaction (CDFT-CI). The nonadiabatic electron transfer methods developed and applied in this work will contribute to a relatively sparse computational toolkit for studying challenging problems in photochemical electron transfer, such as the prediction of nonradiative decay rates from first principle; these, in turn, will contribute to the design of catalytic materials for solar energy conversion.

Thesis Supervisor: Troy Van Voorhis
Title: Haslam and Dewey Professor of Chemistry

Acknowledgments

First and foremost, I extend my deepest gratitude to my Ph.D. advisor, Troy Van Voorhis, on both a personal and a professional level. From the start of my career at MIT when he taught me how to approach problems scientifically and procedurally, to the very end when he supportively helped me find my footing towards the next step of my life, Troy has shown nothing but care for my scientific, personal, and professional development. Troy is the type of advisor who does not forget the meaning of that title: he advises. He is the type of advisor all other advisors should aspire to be, I will deeply miss working for him.

I thank other faculty members at MIT and beyond: Jianshu Cao and Moungi Bawendi, my thesis committee members, for helpful scientific discussions; Keith Nelson, Steve Lippard, Patti Christie, Chris Voigt, Heather Kulik, Mike Stopa, and Gabriela Schlau-Cohen for all of the wonderful teaching opportunities which helped me decide on a career in science education; and David Micha and Dmitri Kilin, for helpful (and continuing!) research mentorship during my undergraduate years.

Thanks to my colleagues in The Zoo: Tim Kowalczyk, Ben Kaduk, Shane Yost, Eric Hontz, Oleg Vydrov, Jiahao Chen, Helen Xie, Dave McMahon, Shuhao Wen, Alex Kohn, Nadav Geva, Tianyu Zhu, Nathan Ricke, James Shepherd, Valerie Vaissier, Piotr de Silva, Zhou Lin, Diptarka Hait, Hongzhou Ye; Liam Cleary, Arend Dijkstra, Jeremy Moix, Javier Cerillo, Jianlan Wu, Chern Chuang, Evan Piephoff, Thanasak Sathiwitayakul; John Kattirzi, Liang Shi, Sucheol Shin, Eric Alt, Chee Kong Lee, Elizabeth Lee, Paul Teichen, and Kaitlyn Dwelle. It's been a pleasure working with you! Also, thanks to Li Miao and Peter Guinta for all of the administrative help over the years!

Thanks in particular to two zoo members, with whom I started my Ph.D. with almost five years ago. Matt Welborn: Your terrible puns, Olecito deliveries, gym encouragement, scientific advice, and (most importantly) our mutual understanding that MIT is the second-best college football team of all time have made life at work significantly more pleasant. Thomas Avila: Your insatiable appetite and interest in both coffee breaks and mooching off my cable subsription for sports has been a wonderful way to break up many a day and evening. Additionally, thanks to Alex Zhukhovitskiy for being such a wonderful and productive experimental collaborator throughout my time at MIT.

My friends outside of work have been a wonderful support network during this time at MIT. I thank in particular Kurt Cox for long chats in the living room of our apartment after particularly rough days; your optimistic outlook never failed to cheer me up! Wankyu, Jenny, Phoom, Kenny, Whitney, Igor, Steph, Jess, Paul, Andrew, and Sam: Thanks for all of the fun memories you've helped create at MIT! Michael, Andrew, Rafael, Carly, Kevin, Francisco, Alan, John, and Manny: Our discussions always keep me grounded at work. Jillian, Jamie, Sam, Jennifer, Chris, Steven, and Michelle: Our catch-up phone-calls always put me in a bright mood after a long day. Phil, Matt, Jamie, and Kristin: Our annual Applebee's trip has given me something to perpetually look forward to! And to everyone else I ran out

of room to explicitly mention: Thank you! You are not forgotten.

I briefly want to thank all of my teachers from elementary school through high school for being such supportive academic mentors on this long, arduous journey. Mrs. Taylor, Mr. Fretz, and Mr. Copp: I consider you two of my primary inspirations to follow a career in science and math. Mr. Buettner and Mr. Reed: I credit you with my development as a writer and a communicator. Mrs. Williams and Mr. Hartley: you have each in your own ways inspired me with a lifelong love of public service. Thank you!

Finally, I would be remiss without thanking the four most important people in my life. To my mom, dad, and grandma: You've always been there for me, right from the start. Thank you for always pushing me to do my best, and being around to talk when my best wasn't good enough. And, finally, to Lauren: I honestly don't know how I would be here without you. You talked me out of quitting; you were there to listen to me lovingly after the hard days; and you provided more than a bit of levity on the good ones. If I had the space, I could spend pages listing off all of the ways each of you have supported me over the years and still not have a complete list; I am forever grateful. With all my love, this thesis is dedicated to all of you.

Contents

List of Figures

List of Tables

Chapter 1

Introduction

Energy drives the global economy in the 21st century. As the world population increases but our fossil fuel reserves remain constant, the energy needs of the world outstrip the supply of traditional energy sources. Many alternative technologies have been proposes based extracting energy from the sun, the wind, volcanic activity inside earth, and nuclear forces, among others; none is yet as efficient and cost-effective as extracting and burning oil, coal, and natural gas. A cheap and efficient technology for the production of useful fuel from sustainable energy sources like the sun is the object of much contemporary scientific research across many disciplines.

The first step in most solar energy conversion technologies is the absorption of sunlight by a chromophore [1, 2, 3]; however, electronic excitations are very short-lived, necessitating a mechanism for longer-term energy storage. One quite popular proposal is to store the solar energy in chemical bonds, using sunlight to split water and produce hydrogen gas as a fuel. This reaction can then be reversed, oxidizing hydrogen gas in a fuel cell to produce water [4]. Artificial water splitting has received considerable attention recently, and several reviews discuss its significance and summarize challenges [5, 6]. Effective catalyst designs range from small molecule transition metal complexes [7, 8] to amorphous cobalt oxides [9] and perovskite materials [10, 11, 12], operating under several different mechanisms. The structures rely on catalytic intermediates with thermodynamics and kinetics that are interesting in their own right.

The problem in solar energy storage thus relies on two central questions: (1) How can energy storage mechanisms like the water splitting reaction be carried out with minimal loss mechanisms? And (2) How can energy from the sun be efficiently turned into charge transfer to mediate the redox activity of these catalysts? The photochemical charge transfer question (2) is of great interest in other areas of energy storage and device manufacturing, as well: upon excitation, nonradiative charge transfer is in competition with radiative decay, which is a loss mechanism in photovoltaic devices [13, 1, 14] and the desired outcome in light-emiting diodes (LEDs) [15]. These processes are of particular interest in organic devices, where photochemical charge-transfer is a common occurrence [16, 17].

Theoretical and computational modeling is today ubiquitous and essential in understanding many aspects of solar energy conversion. Computation has been used to great success in mechanistic studies in catalytic oxygen evolution [18, 19] and carbon dioxide reduction [20], allowing us to understand and improve upon the conversion of solar energy to fuel. It has also been used to model the structure [21, 22, 23] and energy transfer dynamics [24, 25] of photosynthetic complexes, allowing us to understand the inner workings of the best solar energy conversion device in existence.

Computation additionally allows us to screen materials computationally before making them experimentally. Computational high throughput screening for materials design is increasingly a reality, since computing power and memory have increased to the point where materials can be treated with sufficient accuracy in reasonable amounts of time [26]. Industrial applications of such techniques are rapidly becoming routine, with substantial progress being made in the design of lithium batteries [27]; polymerization catalysts [28]; carbon sequestration [29]; and photovoltaic cells [30, 31, 32]. The route to success in each case relies upon the identification of certain descriptors that are indicative of efficiency or catalytic activity whilst being straightforwardly calculable: excitation, emission, and nonradiative decay properties of photovoltaics; electron transfer barrier heights; catalyst-substrate bond strengths; and more. Density functional theory calculations for these applications are now widespread, and stability analyses via thermodynamic quantities are often sufficient to discover reaction mechanisms [33, 34].

Prominent successes have, therefore, been made in designing redox catalysts for a wide variety of reactions. For instance, catalyst selectivity in hydrogenation reactions was enhanced by using the far-cheaper Zn-Ni alloy in place of the Ag-Pt catalyst; this result was screened for computationally and then verified experimentally [35]. Another success screened hydrogen evolution catalysts using hydrogen adsorbtion energies as the descriptor, and following screening showed that Bi, which can poison Pt catalysts, could be alloyed with the Pt to produce a catalyst with a modestly improved rate [36]. A wide variety of dopants can be added to TiO_2 to produce new catalysts for oxygen evolution reactions, in particular Cr/Mo/Mn/Ir [37]. This is in contrast to the far more expensive RuO_2 or IrO_2 catalysts. In similar work on oxygen reducing reactions (ORR), a volcano plot analysis was used to predict that Pt_3Y and Pt_3Sc would be superior catalysts to bare Pt [38]. This claim was then verified experimentally and up to a 10-fold rate enhancement was seen. Finally, it was also found that CO oxidation was enhanced by doping TiO_2 [39, 40]. In general, therefore, computational tools can be used to predict the thermodynamics and kinetics of electron transfer, which can be used to screen materials implicated in energy conversion for efficiency based on their mechanisms.

In this thesis, we look at quantum mechanical modeling of the two central questions in energy storage raised above. Many of the observations regarding catalytic mechanisms can be transferred to other processes, such as oxygen reduction [38] and carbon dioxide reduction [41, 29]. Additionally, many of the theoretical tools developed to study photochemical charge transfer can be transferred to model

other problems in chemistry involving diabatic states. Such problems include: the modeling of proton transfer dynamics and the prediction of pKa values from first principle [42]; keto-enol tautomerization of biochemical molecules like DNA bases [43, 44]; characterization of charge and energy transfer in photosynthetic complexes [45]; and the *ab initio* prediction of quantum yields, important in the design of organic photovoltaics and LEDs [46].

In this introductory chapter, we review the theoretical framework underlying condensed phase electron transfer, starting with Marcus theory and moving on to more contemporary system-bath model approaches. In particular we examine conical intersections, which are implicated in many photochemical decay processes. We then examine some of the computational tools used, largely based on DFT, and various ways to computationally model solvent. Finally, we outline the structure of the remainder of this thesis.

1.1 Theoretical models for electron transfer in solution

1.1.1 The diabatic picture

Typically, we tend to think of electronic states in chemistry as *adiabatic states*—the states that diagonalize the molecular Hamiltonian. In the language of photochemistry, closed-shell molecules live in the ground state S_0, and are excited to higher singlet excited states such as S_1 and S_2 upon absorption of a photon. The molecule can then decay radiatively back to the ground state or nonradiatively through several pathways such as internal conversion (from a higher singlet state to a lower singlet state) and intersystem crossing (through a triplet state).

The adiabatic picture is useful for describing much of chemistry; however, it is not intuitive for describing charge-transfer excitations. Adiabats inherently *delocalize* electron density. The simplest example of this is the case of the adiabats of H_2—its σ and σ^* molecular orbitals. The ground state of H_2 is symmetrically delocalized over both hydrogen atoms, whereas the excited state is antisymmetrically delocalized over both atoms. When considering charge transfer, we are often interested in the question: How much charge comes from one spatially-localized region in a molecular system and ends up on another spatially-localized region, and how long does this process take? In order to consider states which are localized—or, more precisely, states that do not change in chemical character along a generalized reaction coordinate—we will abandon the concept of adiabatic states in favor of an alternative picture: the diabatic picture.

In the diabatic picture, electronic states by definition do not change change character moving from left to right along a reaction coordinate [47]. One diabat may, for example, correspond to charge localization on the left molecule in a dimer; the other diabat, charge localization on the right molecule. In the diabatic picture, the Hamiltonian describing the electronic system is not diagonal; the off-diagonal matrix elements

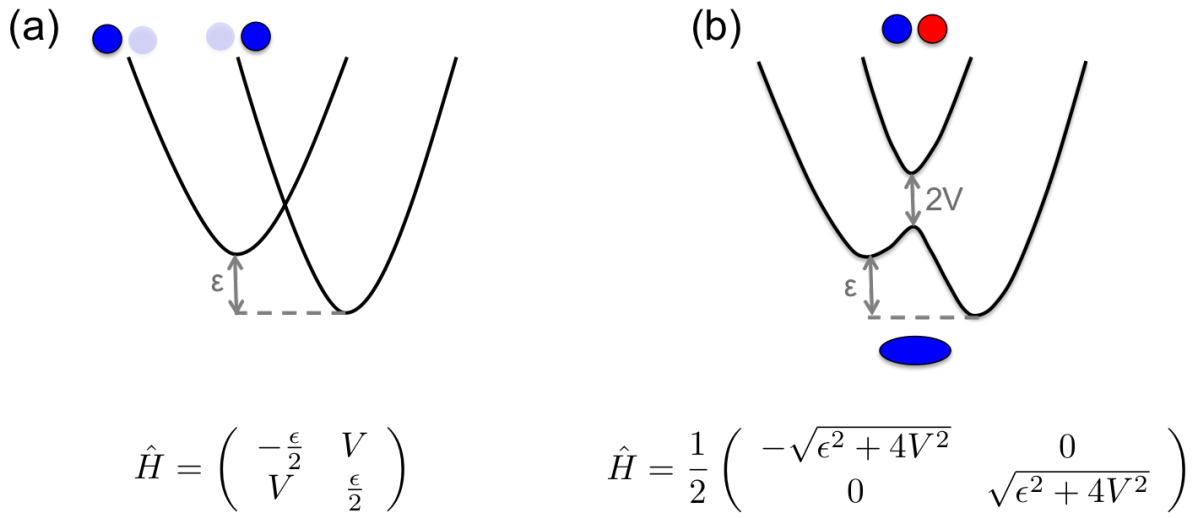

Figure 1-1: (a) In the diabatic picture, the Hamiltonian is not diagonal. Each electronic state has the same chemical character across the entire potential energy surface; in the case pictured, the left state corresponds to electron on the left atom, and the right state the electron on the right atom. (b) In the adiabatic picture, the Hamiltonian is diagonal. As one moves along an electron state, the chemical character of the state changes. In the case pictured, the ground state changes character from "electron on the left" to "electron on the right" moving from left to right along the pictured reaction coordinate.

are known as *diabatic couplings* or *electron couplings*; they determine how population transfers from one state to another. A summary of the diabatic basis and adiabatic basis is presented in Figure 1-1.

Due to the nature of charge-transfer, the diabatic basis is a natural one: in the gas phase, one must only know the intrinsic energy difference between the states and the diabatic coupling between the states to fully describe charge-transfer. In the condensed phase, however, things become more complicated, as we also require some information about how the solvent influences charge transfer. In the following sections, we take into account the role of solvent and discuss various theoretical models based on diabatic states that are used to describe condensed-phase charge transfer.

1.1.2 Marcus Theory

Since its proposal [48, 49] and Nobel Prize citation [50], the electron transfer theory of Marcus has become the canonical theory for describing condensed-phase electron transfer kinetics. The insight provided by Marcus is that the electron transfer rate in solution is caused by solvent fluctuations. When the solvent is in its equilibrium configuration (i.e. its nuclear dipoles and electron polarization are aligned to stabilize excess charges; Figure 1-2(a), top-left panel), the energetic cost of electron transfer is too high. The timescale of electron transfer is much faster than the timescale of nuclear solvent rearrangement due to the difference in mass between electrons and nuclei; as such, instantaneously moving an electron from one molecule to another would require large solvent reorganization (Figure 1-2(b), top-left panel).

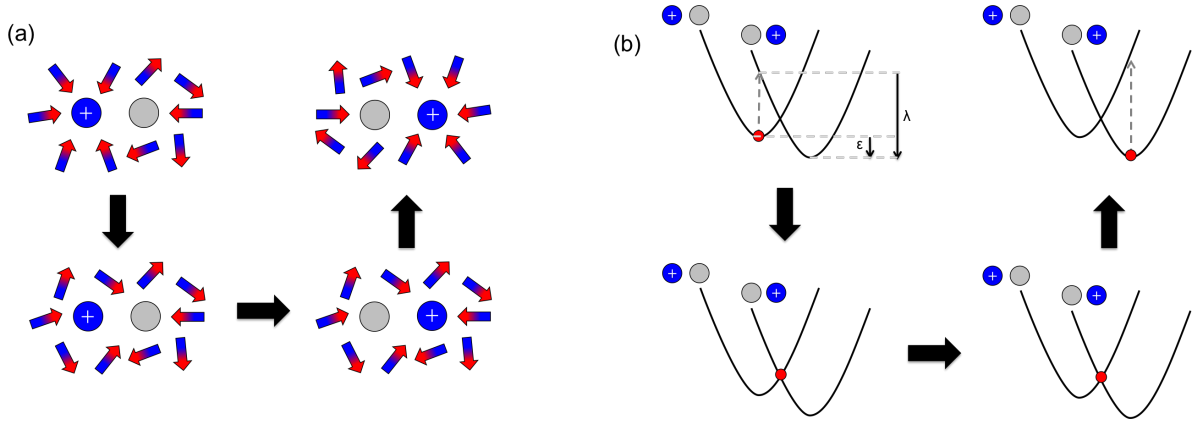

Figure 1-2: Marcus theory dictates charge-transfer rates in the diabatic, slow-bath limit. (a) In the Marcus model, charge cannot transfer when the solvent is in its equilibrium configuration; the energetic cost for solvent reorganization is too high. Instead, the charge-transfer rate is governed by solvent fluctuations: when the solvent fluctuates to a configuration such that charge on either donor or acceptor is isoenergetic, charge can transfer and the solvent can relax. (b) Pictured are two diabatic energy surfaces as a function of a collective coordinate describing solvent polarization. Solvent fluctuations correspond to fluctuations in the energy gap ΔE—the difference in energy between the two diabats at a given solvent configuration. As the solvent explores various configurations around the minimum of each parabolic potential energy surface, the energy gap shrinks and grows accordingly. The two thermodynamics parameters associated with the Marcus rate (Equation 1.1; the bias ϵ and the reorganization energy λ) are labeled.

Instead of an instantaneous transfer at equilibrium, Marcus proposal that electron transfer in solution follows the path outlined in Figure 1-2: due to temperature, the solvent dipoles and electron polarizations fluctuate until the two diabats have the same energy. Then, and only then, is electron transfer energetically feasible. The electron may then quickly switch diabats (before the solvent has a chance to move, again due to the timescale difference), at which point the solvent can relax into a new equilibrium configuration.

Based on geometric arguments as well as an application of Fermi's Golden Rule [51], Marcus showed that the electron transfer rate is given as

$$k_{ET} = \frac{2\pi}{\hbar} \frac{|V|^2}{\sqrt{4\pi\lambda k_B T}} \exp\left[-\frac{(\lambda+\epsilon)^2}{4\lambda k_B T}\right] \tag{1.1}$$

where V is the diabatic coupling between the states, T is the temperature, $\hbar$ is Planck's constant, k_B is the Boltzmann constant, and ϵ and λ are two thermodynamics parameters of the electron transfer, called the *electronic bias* and the *reorganization energy*, respectively. The electronic bias is defined as the energetic different between the minima of the two diabats involved in electron transfer; the reorganization energy, the energy required to move the solvent from the equilibrium configuration of one diabat to the equilibrium configuration of the other diabat. Both quantities are labeled in Figure 1-2(b).

Marcus theory predicts three distinct electron transfer regimes: $-\epsilon > \lambda$, or the *normal regime*, $-\epsilon < \lambda$, or the *inverted regime*, and $-\epsilon = \lambda$, where the activation energy disappears and electron transfer

is fastest. Traditional intuition based on linear free-energy relationships [52] suggests that as the energetic bias between two states increases, the rate should also increase; while this is true in the normal regime, the opposite is true in the inverted regime. Nevertheless, the existence of the inverted regime—where increasing the bias between the states *decreases* the electron transfer rate—as first predicted by Marcus has been verified experimentally innumerable times [53, 54, 55, 56, 57, 58, 59, 60, 61].

As the Marcus rate is a Fermi Golden Rule rate, it is only valid when second-order perturbation theory in V is valid: when the electronic coupling is small. Additionally, the Marcus rate makes several assumptions about the solvent: (1) that electron transfer is instantaneously fast compared to the timescale of solvent reorganization (i.e., solvent reorganization is slow); (2) that electron transfer is a rate process (i.e. there are no long-lived quantum coherences between the electronic states); and (3) that both diabats interact with the same set of solvent modes. We will explore how we can generalize the first two of these three approximations in the following section.

1.1.3 System-Bath Models

Marcus's key insight was that solvent plays the central role in condensed-phase electron transfer. Unfortunately, an exact dynamical description of this process from first principles is difficult if not impossible due to the multitude of degrees of freedom involved in solvent reorganization, which are necessary to describe electron transfer dynamics and kinetics. Because exact quantum methods cannot describe systems with thousands of degrees of freedom without running into exponential scaling, approximate models are often invoked to describe electron transfer dynamics.

System-bath models are one class of these approximate models which are particularly well-suited to studying electron transfer. In a system-bath model, the chemistry being studied is partitioned into a "system"—the interesting part—and a "bath"—a part that is uninteresting on its own, but paramount for describing the system accurately. System-bath models are useful for studying short-term chemical dynamics due to their inherent simplicity; in this thesis, we will use system-bath models extensively to relax two of the assumptions that Marcus theory makes about solvent relaxation (as discussed in Section 1.1.2).

One important system-bath model for describing chemical dynamics is the spin-boson model, a system-bath model that describes a two-level system coupled linearly to a large number of harmonic bath modes [62] (Figure 1-3). The spin-boson Hamiltonian (also known as the Caldeira-Leggett model) [62] can be written as

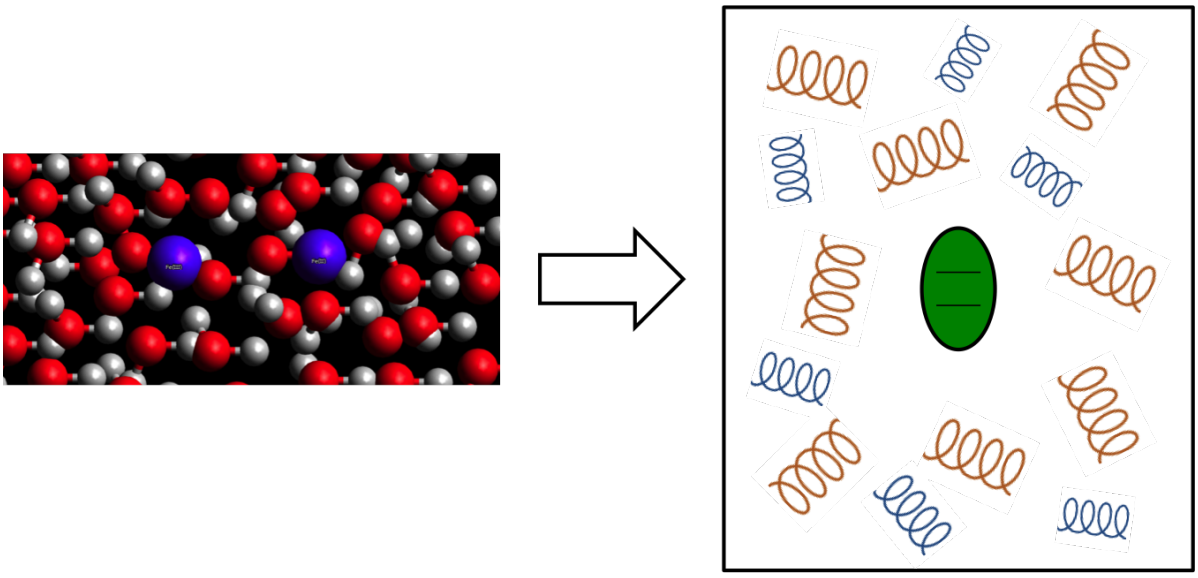

Figure 1-3: Schematic representation of a system-bath model. A chemical system can be mapped on to something much simpler; in the case pictured, it is mapped on to the spin-boson model, a two-level system interacting linearly with only harmonic bath modes. Such systems can be a useful way to describe electron transfer in solvent without explicitly considering tens of thousands of degrees of freedom.

$$\begin{aligned}\hat{H} &= \hat{H}_S + \hat{H}_B + \hat{H}_{SB} \\ &= \begin{pmatrix} \frac{\epsilon}{2} & \hat{V} \\ \hat{V} & -\frac{\epsilon}{2} \end{pmatrix} + \sum_j \begin{pmatrix} \frac{p_j^2}{2m_j} + \frac{1}{2}m_j\omega_j^2 x_j^2 & 0 \\ 0 & \frac{p_j^2}{2m_j} + \frac{1}{2}m_j\omega_j^2 x_j^2 \end{pmatrix} + \sum_j \begin{pmatrix} c_j x_j & 0 \\ 0 & -c_j x_j \end{pmatrix} \end{aligned} \quad (1.2)$$

where the p_j and x_j describe normal mode harmonic bath coordinates and momenta described by mass m_j and frequency ω_j, and the c_j are coefficients determining the strength that each harmonic bath mode couples to the system.

In practice, knowing the minute details of the bath modes is irrelevant: by invoking system-bath models, we are implicitly only interested in the detailed dynamics of the system, so we only need to know about the bath insomuch as it affects system dynamics. For a harmonic bath, population dynamics are completely characterized by the bath *spectral density*, [63, 64, 51]

$$J(\omega) = \frac{\pi}{2}\sum_j \frac{c_j^2}{m_j\omega_j}\delta\left(\omega - \omega_j\right) \quad (1.3)$$

In principle, a particular spectral density can generally be obtained by Fourier transforming a corresponding bath time correlation function [51]; these time correlation functions can, in turn, be obtained from experiment or from molecular dynamics simulations. Many times, an analytical form is usually assumed for the spectral density.

The spin-boson Hamiltonian is used widely in elementary studies of chemical dynamics because of its moderate assumptions and overall simplicity. While simpler than an atomistic model, the spin-boson model still cannot be solved exactly: the exact density matrix and the propagator must each be expanded in the basis of a many-dimensional collection of harmonic oscillators, again leading to exponential scaling. Nevertheless, many approximate methods [63, 65, 66, 67, 68, 69, 70] (and exact methods for certain assumptions about the bath [71, 72]) for solving the Schrödinger equation for this Hamiltonian exist.

The spin-boson model is particularly well-suited to studying the condensed phase electron transfer problem: Its harmonic approximation implied parabolic potential energy surfaces in appropriate limits, like those used in Marcus theory. It can be shown analytically that the dynamics generated by the spin-boson Hamiltonian reduce to Marcus kinetics in the long-time, slow-bath, diabatic limit—exactly the limit that the Marcus rate is valid. The spin-boson model can be thought of as a many-dimensional extension of Marcus theory that can be used beyond some of the limits where Marcus theory breaks down. We will thus be using this model as a starting point for nonadiabatic electron transfer dynamics studies.

1.1.4 Conical Intersections

Photochemically-excited molecules can relax back to the ground state either through radiative processes or nonradiative processes. When relaxation is fast, it is thought that molecules relax from excited state to ground state through *conical intersections*—points where the excited state adiabatic potential energy surface cross the ground state adiabatic potential energy surface [73]. Conical intersections have been studied extensively in the gas phase both theoretically [74, 75, 76, 77, 78, 17] and experimentally [79, 80, 81]. Condensed-phase photochemistry is often much more complicated, as a continuum of bath modes now must be considered (especially at low frequencies, accounting for very slow solvent motion). Condensed-phase conical intersections are much less-studied [82, 83, 84, 85]. Nevertheless, conical intersections in condensed phases are thought to be important for such processes as internal conversion and intersystem crossing [86], the understanding of which is essential for the prediction of quantum yields in devices such as photovoltaics and light-emitting diodes [14] and the understanding of DNA/RNA isomerization [79, 87]. A condensed-phase model capable of describing conical intersections is thus of great scientific importance.

Unfortunately, many existing condensed-phase models predict the nonexistence of conical intersections. In order for a conical intersection to exist, two conditions must be upheld: (1) the excited state and ground state have the same energy; and (2) the electronic coupling between the two states must be zero [73]. Under the Condon approximation, the electronic coupling is not a function of the nuclear coordinates and can never be zero; thus, any model utilizing the Condon approximation, including the canonical spin-boson Hamiltonian, cannot describe conical intersections—phenomena which are paramount to the accurate description of photochemical processes. The qualitative difference between the adiabatic sur-

(a) (b)

Figure 1-4: Conical intersections in N dimensions manifest themselves as surfaces intersecting along N-2 dimensions; thus, the smallest dimension along which two adiabats can intersect is two, and in 2D that intersection is a point. (a) Under the Condon approximation, the coupling can *never* be zero for any value of the two nuclear coordinates, and the two adiabats will *never* intersect; the closest they get to each other is an avoided crossing, with magnitude $2V$. (b) If the coupling is allowed a linear dependence on each coordinate, the adiabats can intersect at a single point—a conical intersection.

faces predicted by two-dimensional two-state Hamiltonians (a) under the Condon approximation, and (b) beyond the Condon approximation is shown in Figure 1-4.

Because the spin-boson model does not predict the existence of conical intersections, we must use a slightly different model when we wish to accurately study photochemical dynamics. We use a generalization of the spin-boson Hamiltonian known in the literature as the linear vibronic coupling (LVC) model:

$$\hat{H}_{LVC} = \hat{H}_{SBM} + \sum_j \begin{pmatrix} 0 & V_j \hat{x}_j \\ V_j \hat{x}_j & 0 \end{pmatrix} \tag{1.4}$$

We choose this model because all of the tools we can use to study the spin-boson model can also be used to study the LVC model. We make use of this model in Chapter 4 in particular, where we develop and study the theoretical framework which can be used to computationally model conical intersection dynamics.

1.2 Computational models for electron transfer in solution

Regardless whether we are studying electron transfer thermodynamics, kinetics, or dynamics, we need to compute (1) the thermodynamic stabilities the chemical moities involved with electron, and (2) the interaction of the electron transfer system with solvent. When we are looking at catalyst intermediate stability for catalytic screens, the thermodynamic stability of the solvated intermediates is of the utmost important [88, 34]; for kinetics, we need not only the thermodynamic driving force of electron transfer ϵ but also an accurate description of the reorganization energy λ [58]. To describe electron transfer *dynamics*, an even more detailed description of the solvent is required: We must compute spectral densities from sampled bath correlation functions. Additionally, through all of this, we wish to use the diabatic picture

to describe electron transfer as it is a natural basis for the description of this phenomenon; because of this choice, we must additionally compute or model the diabatic coupling V. Things are especially complicated for the modeling of conical intersections, as we need time correlation functions of V.

In this section, we describe the computational approaches used to describe electron transfer in solvent. We treat all nuclei electrons quantum-mechanically and all nuclei classically. We first discuss density functional theory, which we use for all thermodynamic quantities associated with the "system" piece of a system-bath model Hamiltonian as described in Section 1.1.3; the formalism of density functional theory is reviewed in Section 1.2.1. Of particular note is a DFT-based method to compute diabatic states and diabatic coupled: constrained density functional theory with configuration interaction.

We then move our discussion to approximate computational descriptions of the bath—solvent. We review implicit solvent models, which can often be useful for computing thermodynamic quantities such as redox potentials but lack the detail necessary to compute more complicated bath phenomina such as reorganization energies or spectral densities. For these, we must use explicit solvent sampled with molecular dynamics. Implicit and explicit solvent are discussed and compared in Section 1.2.2.

1.2.1 Density Functional Theory

Kohn-Sham Density Function Theory

Within the Born-Oppenheimer approximation, a molecule is a collection of N electrons interacting with a classical external potential generated by the masses and charges of fixed nuclei. Quantum-mechanically, molecules are described by a many body wavefunction $\psi(\mathbf{r}_1, ..., \mathbf{r}_N)$ obtained by solving the Schrödinger equation for the molecular Hamiltonian—the Hamiltonian describing the kinetic energy of a molecule's electrons, their interactions with each other, and their interactions with a particular configuration of nuclei that keep them bound. Approximate methods to obtain $\psi(\mathbf{r}_1, ..., \mathbf{r}_N)$ have been around since near the dawn of quantum mechanics in the form of Hartree-Fock theory [89], but the energies associated with these Hartree-Fock wavefunctions are often not acceptably accurate for chemical problems. Hartree-Fock theory is also difficult improve upon due to the theoretical complexity of working with a function of 3N coordinates.

Density functional theory (DFT) is an attempt to compute quantities associated with the quantum-mechanical many-body wavefunction $\psi(\mathbf{r}_1, ..., \mathbf{r}_N)$ without referencing the many-body nature of the wavefunction at all. Instead, DFT posits that a classical quantity, the electron density—a function of 3 variables, not 3N—contains all of the information needed to describe the chemistry of a molecule. In terms of the wavefunction, the density $\rho(\mathbf{r})$ can be represented as

$$\rho(\mathbf{r}) = \int \psi^*(\mathbf{r}, \mathbf{r}_2, ..., \mathbf{r}_N)\psi(\mathbf{r}, \mathbf{r}_2, ..., \mathbf{r}_N)d\mathbf{r}_2...d\mathbf{r}_N \tag{1.5}$$

The advent of modern DFT occurred when Hohenberg and Kohn proved their eponymous theorem [90]: There exists a universal functional of the electron density, $F[\rho(\mathbf{r})]$, that determines the energy of that density interacting with an external potential v_{ext},

$$E[\rho(\mathbf{r})] = \int v_{ext}(\mathbf{r})\rho(\mathbf{r})d\mathbf{r} + F[\rho(\mathbf{r})] \tag{1.6}$$

Additionally, the Hohenberg-Kohn theorem states that the energy functional in Equation 1.6 is minimized for the density associated with the ground state wavefunction of the system. While the Hohenberg-Kohn theorem was a theoretical landmark in the field of electronic structure, practically, it has little use: The universal functional of the density $F[\rho(\mathbf{r})]$ is unknown, and in practice must be approximated.

Most practical implementations of DFT calculations today use the Kohn-Sham formalism [91]. In Kohn-Sham DFT the electron density is expanded in a basis of fictional, one-electron, non-interacting orbitals ($\phi_i^{KS}(\mathbf{r})$, the Kohn-Sham orbitals), such that

$$\rho(\mathbf{r}) = \sum_i |\phi_i^{KS}(\mathbf{r})|^2$$

The energy functional in the Kohn-Sham formalism becomes

$$E[\rho(\mathbf{r})] = T_s[\rho(\mathbf{r})] + \int v_{ext}(\mathbf{r})\rho(\mathbf{r})d\mathbf{r} + E_H[\rho(\mathbf{r})] + E_{xc}[\rho(\mathbf{r})] \tag{1.7}$$

where T_s is a functional which determines the *non-interacting* kinetic energy (since the Kohn-Sham orbitals do not interact with one another), E_H is the Coulomb energy (determined from the density via classical electrostatics [92]), and E_{xc} is the *exchange-correlation functional*—an energy functional that contains everything else that contributes to the energy of a molecular system. Effects included in the exchange-correlation functional include the interacting piece of the kinetics energy, electron exchange, and electron correlation.

The advantage of the Kohn-Sham picture over an orbital-free picture is that because the density can be partitioned into many non-interacting one-electron orbitals, certain components of the exact functional can be computed exactly. Perhaps most importantly, it circumvents the problem of defining a kinetic energy functional $T[\rho(\mathbf{r})]$ by introducing a non-interacting kinetic-energy functional $T_s[\rho(\mathbf{r})]$, which contains the major component of the kinetic energy. All non-well-defined electron-electron interactions are wrapped up in the exchange-correlation functional. The disadvantage of the Kohn-Sham picture is that the exchange-correlation functional, while it has certain properties it must obey, is not known and must be approximated. Further, each approximation is uncontrolled, meaning the accuracy of Kohn-Sham DFT calculations is not systematically improvable.

Nevertheless, certain classes of exchange-correlation functionals which share properties have developed, and a hierarchy known as Jacob's Ladder exists among these classes of functionals [93]. Classes

higher up on the hierarchy are demonstrably better than classes lower on the hierarchy. The lowest rung of the ladder includes local density approximation (LDA) functionals [94, 95], where E_{xc} is a functional only of the electron density. Higher are generalized gradient approximation (GGA) functionals such as PBE [96], in which E_{xc} depends on both the density and its gradient at every point—allowing for description of regions of non-uniform densities in molecules. Hybrid functionals like B3LYP [97] and PBE0 [98] take GGA functionals and add in exact exchange from Hartree-Fock theory, improving energies further. Finally, nonlocal van der Waals functionals such as VV10 [99] are functionals that connect the density at a point **r** to another point **r'**. In this thesis, we primarily use hybrid functionals, as the tradeoff between accuracy and speed is the greatest for the classes of problems considered.

Constrained Density Functional Theory

Density functional theory exceeds at approximating the energy of molecular adiabats; electron transfer theories, however, require knowing the approximate energies of diabats, and their couplings. It is rigorously impossible to create strict diabatic states from a given set of adiabats [47, 100, 101]; however, these diabats can be approximately constructed using a DFT-based tool known as constrained density functional theory (CDFT).

In a CDFT calculation, one can compute the lowest energy electronic state of a molecule subject to a set of constraints on the electron density. In general, the constraint can be written as

$$\int w_C(\mathbf{r})\rho(\mathbf{r})d\mathbf{r} - N_C = 0 \tag{1.8}$$

where ρ is the electron density, N_C is the value of the constraint, and w_C is a weighting function which allows different spatial regions of the density to have different values of the constraint. Imposing the constraint in equation 1.8 is equivalent to solving a Kohn-Sham equation with an effective Kohn-Sham potential

$$V_{KS}^{eff} = V_{KS} + V_C w_C(\mathbf{r}) \tag{1.9}$$

where V_C is a Lagrange multiplier imposing the constraint w_C. We have developed a method to solve the Kohn-Sham equations using the potential in equation 1.9 efficiently [102]. Appropriate choice of the constraint functions w_C can result in the formation of approximate diabats, as well as charge transfer excited states; CDFT can thus be used as a tool to extract diabat energies and charge-transfer excitation energies to sufficient accuracy [103, 104, 105].

One is often interested not only in the electronic structure of a diabat but also its interaction with other states. Such electronic couplings are important for hopping probabilities between states and thus rates. By using a few constrained states of interest in order to form a configuration-interaction basis, we have shown [106, 107] that one can estimate the coupling with CDFT-CI using matrix elements of the

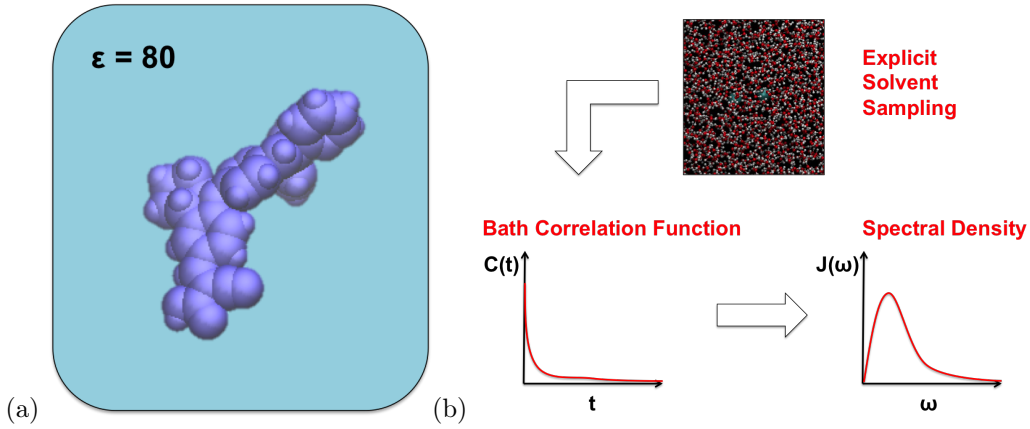

Figure 1-5: (a) In an implicit solvent model, a cavity is carved out of space based on the van der Waals radii of all of the atoms in the solute. The remainder of space is then filled with a polarizable material of a given dielectric, which is allowed to self-consistently polarize to account for the electronic structure of the solute. The dielectric continuum, in turn, polarizes the solute's electrons. Implicit solvents are useful for quick, accurate calculations of solvation thermodynamics. (b) In an explicit solvent model, each solvent molecule is explicitly represented in the simulation. From the motions of the solvent, bath correlation functions can be extracted, which can then be Fourier transformed into spectral densities—the central quantity needed to compute the dynamics of system-bath model Hamiltonians.

CDFT constraint operators. For two CDFT states $|D\rangle$ and $|A\rangle$ with energies E_D and E_A (respectively), the coupling V can be estimated as

$$\begin{aligned} V &= \left[\frac{E_D + E_A}{2} + \frac{V_{CD}w_{CD} + V_{CA}w_{CA}}{2}\right]\langle D|A\rangle \\ &\quad -V_{CD}\langle D|w_{CD}|A\rangle - V_{CA}\langle D|w_{CA}|A\rangle \end{aligned} \tag{1.10}$$

These couplings can then be used directly in a Marcusian rate expression like Equation 1.1, or to parameterize a system-bath Hamiltonian like the spin-boson model (Equation 1.2). There are limitations to the accuracy of CDFT-CI couplings which will be addressed in Chapter 5; despite these limitations, CDFT-CI couplings are often good approximations for diabatic couplings [105, 106, 47].

1.2.2 Solvent models

We now turn our attention to computational descriptions of solvent. We discuss two approaches to modeling solvent: implicit approaches, which are computationally cheap and often accurate for thermodynamics applications; and explicit approaches, which are computationally costly but necessary for very accurate descriptions of the solvent needed in dynamics applications. These two different approaches to solvation are summarized in Figure 1-5.

Implicit solvation

In implicit solvation, the solute density responds self-consistently to a surrounding dielectric continuum parameterized according to the identity of the solvent [108]. This is a mean-field treatment of solvation in which solute flexibility can be described in principle through conformational sampling, but is often only accounted for within the harmonic approximation. A very popular class of implicit solvent models are the polarizable continuum models (PCMs), including conductor-like screening models like COSMO [109] and CPCM [110].

The underlying approximation of these methods is that the solvent can be easily described by a single dielectric constant ϵ describing the low-frequency polarization of the solvent. Implicit solvent models thus work very well for neutral species near equilibrium [111], as here only infinitely slow motions of the solvent contribute to the solvation energy. Because implicit models are fast, they are often the method of choice for computing accurate solvation free energies [112, 113]. Far from equilibrium, however, a simple dielectric response picture cannot hope to capture detailed solvent dynamics. Instantaneous electron polarization, high-frequency solvent reorganization, and hydrogen bonding—all important features of dipolar solvents, and essential to capture the properties of water—are not modeled in dielectric continuum models. For properties requiring a description of these, such as reorganization energies and bath correlation functions, explicit solvent models are required.

Explicit solvation

In an explicit solvent model, each molecule of solvent is represented explicitly in the simulation. Atomistic treatment of the solvent removes most of the approximations associated with the use of implicit solvent, allowing us to capture effects such as hydrogen bonding and heterogeneities in solvent polarization. Unfortunately, modeling explicit solvent also requires extensive configurational sampling to incorporate all solute and solvent degrees of freedom.

As a consequence, modeling with explicit solvent is much more computationally demanding, and one must often tolerate a limited sampling of solvent configurations or a more approximate description of the solvent electronic structure. The most approximate way to describe the electronic structure of the solvent is also the way to allow for extensive configurational sampling: describing the solvent with a molecular mechanics (MM) force field. In MM, each solvent molecule is described by its own internal bond energy, Coulomb interactions among its atoms and the rest of the atomics in the simulation, and a van der Waals radius interacting with the rest of the simulation via a Lennard-Jones interaction. Altogether, these interactions are defined by a set of parameters called a 'force field.' MM force fields parameters are chosen to replicate collections of experimental observables and/or *ab initio* data [114, 115].

A more accurate description of a single individual configuration (at the cost of being able to sample fewer total configurations) can be obtained by adding electron polarization to an MM force field. The

most common way to add polarization is by using Drude particles—fictional charges tethered to a site on each solvent molecule by a harmonic restoring force [116]. Polarizable MM is able to capture both timescales associated with solvent reorganization upon electron transfer: fast electron polarization, and slow nuclear polarization; polarizable MM is essential for accurately computing reorganization energies [117, 118].

Even more accurate still is to allow the electronic structure of the solute—the electron transfer system described by the system Hamiltonian in a system-bath model—to relax self-consistently with each sampled solvent configuration. Such quantum mechanics - molecular mechanics (QMMM) simulations [119] allow for extremely accurate descriptions of solvent, allowing for quantitative prediction of thermodynamic redox potentials [118] and thus Marcus kinetics; however, they come at an additional cost, as every sampled configuration requires an electronic structure calculation.

In order to study electron-transfer dynamics using system-bath models, configurational sampling of the solvent is of paramount importance. As discussed in Section 1.1.3, so long as the harmonic bath approximation holds, all effects of solvent on an electron transfer system can be distilled into a single function of the frequency of bath modes: the spectral density. As depicted in Figure 1-2, solvent fluctuations cause fluctuations in the energy gap between diabatic states, and these fluctuations in the energy gap drive electron transfer. It should thus come as no surprise that the spectral density is intimately related to energy gap fluctuations; for the spin-boson model, this relationship can be expressed mathematically as

$$J(\omega) = \frac{\beta\hbar\omega}{4}\int_0^\infty \langle \delta\Delta E(t)\delta\Delta E(0)\rangle \cos(\omega t)\, dt \tag{1.11}$$

where $\beta = 1/k_B T$ is the inverse temperature, $\Delta E(t) = E_{|2\rangle} - E_{|1\rangle}$ is the energy gap between states $|2\rangle$ and $|1\rangle$ at time t, and $\delta\Delta E(t) = \Delta E(t) - \langle \Delta E\rangle$ describes the fluctuations of the energy gap away from its average value. We see, then, that the spectral density is related to the Fourier transform of the *time correlation function* of the energy gap, which can be sampled from molecular dynamics [51, 120].

Other methods

We mention in passing other solvent methods, though they will not be used in this thesis. It is possible to combine the strengths of both methods through three-layer models such as a quantum mechanics / molecular mechanics / polarizable continuum model (QM/MM/PCM) strategy.[121] Semi-empirical and polarizable molecular mechanics (MMpol) models, which lie between the quantum and classical approaches in complexity, offer additional flexibility in constructing multi-level strategies.[122, 116] There are also approaches which do not easily fit into the implicit versus explicit solvation paradigm, such as the RISM approach.[123, 124]

1.3 Structure of this thesis

This thesis comprises two major topics: the prediction of redox potentials to guide the design of artificial redox catalysts, and the development of computational methodologies to study the short-time dynamics of photochemical redox processes. We discuss the first of these topics in Chapter 2; the second is discussed in great detail in Chapters 3, 4, and 5.

In Chapter 2, we examine the essential role of theoretical calculations in understanding the water splitting reaction on heterogeneous catalysts. First, we present an overview of DFT thermochemical calculations on water splitting catalysts, addressing how these calculations are adapted to condensed phases and room temperature. We show how DFT-derived chemical descriptors of reactivity can be surprisingly good estimators for reactive trends in water splitting catalysts. Using this concept, we recover trends for bulk catalysts using simple model complexes for at least the first-row transition metal oxides. We also look at mixtures of these first-row metal oxides, developing design principles based on examining how different combinations of metals affect the redox potentials of key mechanistic steps along with changing the rate-determining step of the overall reaction. We conclude by looking at the kinetics of redox on these catalysts using CoPi as a test case, with particular focus on solvation. Our discussion is intended to provide an overview of the current strengths and weaknesses of the state-of-the-art DFT methodologies for condensed phase molecular simulation involving transition metals and also to guide future experiments and computations toward the understanding and development of novel water splitting catalysts.

Chapter 3 changes focus from the thermodynamics of electron transfer in solvent to the short-time dynamics. We examine the dynamics of spin-boson models to fourth-order in time-dependent perturbation theory in the diabatic coupling. In order to prevent divergences, perturbation expansions must be resummed. Here we present a comparison of different resummation techniques for the memory kernels of generalized master equations up to fourth order. For a variety of different spin-boson parameter regimes, we find that resumming the kernels through fourth order using a Padé approximant results in divergent populations in the strong electronic coupling regime due to a singularity introduced by the nature of the resummation, and thus recommend a non-divergent exponential resummation (the "Landau-Zener resummation" of previous work). The inclusion of fourth-order effects in a Landau-Zener-resummed kernel is shown to improve both the dephasing rate and the obedience of detailed balance over simpler prescriptions like the non-interacting blip approximation (NIBA), showing a relatively quick convergence on the exact answer. The results suggest that including higher-order contributions to the memory kernel of a generalized master equation and performing an appropriate resummation can provide a numerically-exact solution to system-bath dynamics for a general spectral density, opening the way to a new class of methods for treating system-bath dynamics.

In Chapter 4, we extend our analysis from Chapter 3 to develop a formalism to treat condensed-

phase dynamics beyond the Condon approximation. We show that even for an extremely simple test system, hexaaquairon(II) / hexaquairon(III) self-exchange in water, the electronic coupling is expected to fluctuate rapidly and non-Condon effects must be considered to obtain quantitatively accurate short-time photochemical dynamics. As diabatic couplings are expected to fluctuate substantially in many condensed-phase electron transfer systems, we assert that non-Condon effects are essential to quantitatively capture accurate short-time dynamics.

The study in Chapter 4 prompted an investigation into the reliability of CDFT-CI couplings, which we present in Chapter 5. Unfortunately, CDFT-CI occasionally fails significantly, predicting couplings that do not decay exponentially with distance and/or overestimating the expected coupling by an order of magnitude or more. In this chapter, we show that the eigenvalues of the difference density matrix between the two constrained states can be used as an *a priori* metric to determine when CDFT-CI are likely to be reliable: when the eigenvalues are near 0 or ± 1, transfer of a whole electron is occurring, and CDFT-CI can be trusted. We demonstrate the utility of this metric with several illustrative examples.

Finally, we conclude by summarizing key findings in Chapter 6 and presenting them in the broader context of solar energy transfer and energy storage. Future avenues of research in the field are also discussed.

Chapter 2

Exploring Catalytic Design of Metal-Oxide Oxygen Evolution Catalysts with Density Functional Theory

2.1 Introduction

The oxygen evolution reaction (OER) is a popular proposal to store energy from sources such as the sun in chemical bonds, using the energy to split water and produce hydrogen gas as a fuel,

$$\mathrm{H_2O_{(\ell)}} \rightarrow \mathrm{H_{2\,(g)}} + \frac{1}{2}\mathrm{O_{2\,(g)}} \qquad\qquad E^\circ = 1.23\,\mathrm{V}$$

where E° is reported with respect to the standard hydrogen electrode (SHE). This reaction can then be reversed, oxidizing hydrogen gas in a fuel cell to produce water and releasing the energy in the process. The oxygen evolution half-reaction occurs efficiently in nature with low activation barriers [21, 22, 23]; promoting efficient oxygen evolution artificially is a much larger challenge, due to an ill-understood mechanism and resulting high catalytic overpotentials [5, 6]. Catalytic design varies wildly, from small molecule transition metal complexes [7, 8] to amorphous cobalt oxides [9] and perovskite materials [10, 11, 12]; unfortunately, underlying design principles of these materials are often poorly understood.

At first glance, the thermodynamics of the water splitting reaction seem quite simple. In one half-reaction, two molecules of water are split into four protons and a molecule of O_2, releasing four electrons

at a potential of 1.23 V per electron with reference to the standard hydrogen electrode (SHE). In the other half-reaction, which occurs at the SHE, two protons and two electrons combine to form one molecule of H_2. Nevertheless, the full catalytic cycle, illustrated schematically in Figure 2-1, involves several intermediates whose thermodynamic stabilities and interconversion kinetics dictate the overall catalytic activity. Furthermore, the stability of certain intermediates necessitates voltages larger than 1.23 V (overpotential) when running the water splitting reaction on a catalytic surface. Ultimately, the catalyst's molecular structure and the experimental conditions determine the observed efficiency through four interrelated factors:

- Thermodynamics of stable intermediates
- Solvent effects
- Kinetics of chemical and electrochemical steps
- Mechanisms of O-O bond formation and O_2 release

The catalytic cycle proceeds through a series of stable intermediates leading up to the central event of water splitting: formation of the oxygen-oxygen bond. Two qualitatively different mechanisms, dubbed the "acid-base" mechanism (also known as the "nucleophilic water attack" mechanism) and the "direct coupling" mechanism (or "radical coupling" mechanism), are shown in Figure 2-1. The acid-base mechanism proposes that the O-O bond is formed via a nucleophilic attack on an electrophilic metal-oxo species; it is suspected to be the mechanism at play for oxygen evolution in a wealth of synthetic systems [8, 127, 128]. By contrast, the direct-coupling mechanism proposes that two high-valent metal-oxo species on the catalytic surface come together to form O_2; recent computational [129] and experimental [130, 131] evidence suggest this mechanism may be at play for certain metal oxide catalysts.

The acting mechanism for O-O bond formation depends on the participating transition metal center(s) [132] and the pH [133], among other factors. Further complicating matters, the relationship between OER thermodynamics and kinetics is not always clear. Many of the reactive steps shown in Figure 2-1 are proton-coupled electron transfer (PCET) events whose nature (concerted vs. sequential) depends on the transition metal system [21, 22, 7, 130, 129, 127, 131]. Additionally, the critical oxygen-oxygen bond formation step is, invariably, a chemical step – one that depends little on the governing electrical potential and highly on small fluctuations of the local environment. The aqueous environment plays a critical role here, both in providing the proper electrostatic environment around the metal oxo species to facilitate the reaction, and also as a reactant itself: water ultimately is responsible for the displacement of O_2 from the catalyst.

The role of computation in understanding heterogeneous catalysis cannot be overstated. With appropriate care and for systems of moderate size (up to hundreds of atoms), density functional theory (DFT)

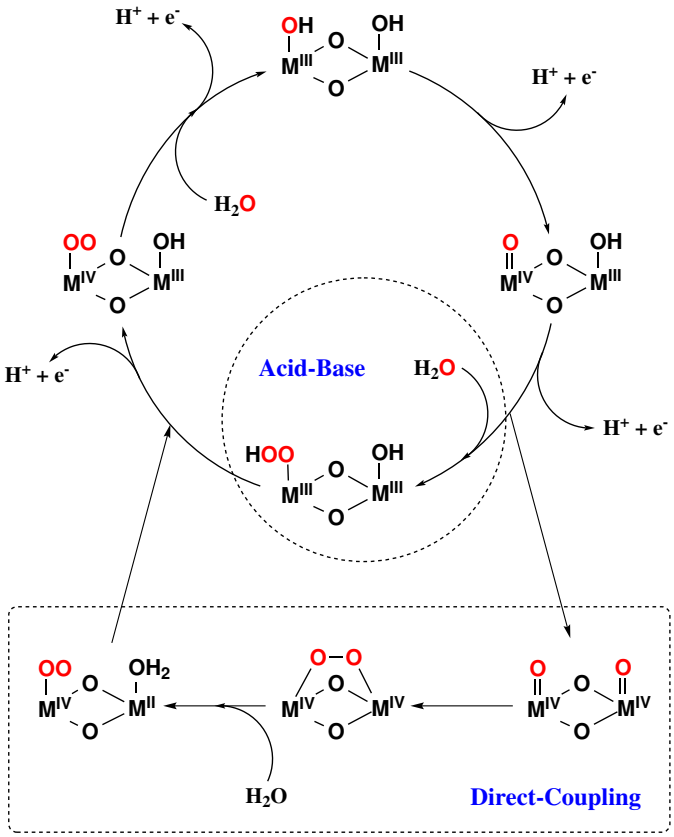

Figure 2-1: Oxygen evolution can proceed via a variety of mechanisms. In this chapter, we will focus on the acid-base (also known as water nucleophillic attack) mechanism, where the O-O bond is formed by a nucleophillic attack by water on an oxidized catalyst; and the direct-coupling (or radical coupling) mechanism, where oxygens a doubly-oxidized catalyst snap together to form the O-O bond. For the direct-coupling mechanism, we refer to the steps in order from the top by the following names: (1) Metal(III) first oxidation, (2) Metal(III) second oxidation, (3) O-O bond formation, (4) Water attachment; (5) Metal(II) oxidation, and (6) Oxygen displacement. In accordance with the observations of many in the literature [125, 126], we focus only on mechanisms involving a Lewis acid, which is thought to be essential for oxygen evolution to occur.

calculations in particular can be used to make useful predictions about the thermodynamics, kinetics, and mechanism of the water splitting reaction on a wide variety of materials, saving time and money in the laboratory by suggesting experiments that should be performed. In particular, DFT can in principle be used both to screen large numbers of catalytic materials [36] and to provide a detailed understanding of the catalytic process on a particular material [129]–both of which can be utilized to guide experimentation. While computation is poised to provide important insights, black-box application of DFT to the problem could easily lead to false conclusions. Proper care must be taken in order to extract accurate thermodynamic data and meaningful trends from electronic structure calculations.

2.1.1 Catalytic screens

Computational high throughput screening for materials design is increasingly a reality, since computing power and memory have increased to the point where materials can be treated with sufficient accuracy in reasonable amounts of time. The ultimate goal of a computational screen is to judge the efficacy of a catalyst without knowing the detailed mechanistic workings of a catalytic cycle; after all, for a novel catalyst, these workings are at best unknown, and at worst unknowable. Sabatier analysis originated in the 1910s [134] and was reintroduced recently by Norskov and others [88, 36, 135] as a tool to screen materials without *a priori* knowledge of mechanism. The Sabatier principle states that an ideal catalyst falls in a Goldilocks region of substrate binding: not too weak, or the substrate cannot adsorb to the catalyst; and not too strong, or the final product cannot desorb. A Sabatier analysis correlates catalytic activity with catalyst-substrate bond energies—quantities which are *thermodynamic* in nature, eliminating the need to study kinetics and thus mechanism. Sabatier analysis has been used with great success in electrochemical catalysis over the past decade [136, 137, 138, 139, 34, 140], in particular guiding the design of certain efficient perovskite catalysts before their experimental realization [141, 10, 142]. It unfortunately requires a 'chemical descriptor' of activity, which certainly will not be universal and may not exist at all for entire classes of catalytic materials.

The challenge for the computational screening of materials is typically cast in terms of finding an appropriate descriptor for the activity, a quantity that can be conveniently calculated for modest cost. Due to the importance of OER, a sizeable quantity of literature is devoted to the exploration of the mechanism of OER and the discovery of such descriptors. Since the basis for the OER mechanism involves oxygen bond breaking, water (or OH) binding, and metal center oxidation, it should be no surprise that these quantities form the basis for descriptors.

Three groups of interrelated descriptors are prevalent in the design of OER. In the first, an orbital/energy level framework, good catalysts are found to have particular 3d states, a good d-band energy match with O_2 energy levels, or particular e_g orbital occupations [143, 10]. These descriptors were used to recently find a barium-strontium-cobalt-iron metal oxide with an order of magnitude higher

activity than iridium oxides.

A prominent group of authors assert that a universal framework for design can be achieved by considering a second descriptor: surface binding of oxygen, hydroxide, or other intermediates [34]. Experimental attempts to use this descriptor to design new catalysts date back to 1955 [144]; recently, Noskov and coworkers have pioneered their use in computational catalytic design through their work on rutiles [145, 146] and metals [135]. It should come as no surprise that the metal-oxygen bond strength descriptor and the orbital framework descriptor are related, as observed by Vojvodic and Norskov [141].

The final descriptor considers the oxidation of the metal. A 1980 paper by Trasatti suggested metal oxidation would supersede the strength of surface adatom binding as the optimal descriptor [147]. Since descriptors always have linear relationships with the overpotential, it is natural to consider whether the overpotential of alloys can be estimated from a linear combination of their constituents. This approach would prevent the increase of computational complexity when ternary complexes are considered, and has recently found success in the case of the design of a Fe-Co-W alloy for OER [148].

Common to all approaches is the formation of a *volcano plot* with respect to the descriptor. In each case, there is a linear relationship with positive slope on one side of an optimal value of the descriptor, and a linear relationship with negative slope on the other side of this optimal value. Both higher and lower values than this optimal value will result in a greater overpotential and thus catalytic inefficiency. While a useful construct, there often exists significant deviation away from the lines defining a volcano plot (see, e.g., [149]). An open question remains as to the utility of using high-accuracy density functional theory (DFT) calculations to explore the design space away from the volcano—does such a space exist, and is its exploration useful in guiding catalytic design?

The concept of a computational screen hinges on systematically understanding what thermodynamic and kinetic factors affect the stability and formation of key intermediates in the catalytic cycle under study. Developing high-throughput screens is thus intricately intertwined with understanding reaction mechanism. Mechanisms determine catalytic intermediates, which determine which physical and chemical properties can be used for screening; screens, in turn, eliminate unfeasible mechanisms.

2.1.2 This chapter

In this chapter, we review the role of computation in understanding water splitting by artificial transition metal catalysts. We first review what DFT is particularly good at: thermochemistry. We compute the overpotentials associated with different mechanisms on the same catalysts, hypothesizing that if the true rate-determining step (RDS) of a catalyst is chemically similar to the RDS of an incorrect mechanism, the overpotentials predicted from the incorrect mechanism may still be quantiatively accurate. We next aim to develop a catalytic screen for mixed alloys of transition metals by studying in detail the properties of mixed metal-oxide dimers, or 'heterobimetallics.' Through the development of this screen, we necessarily

must critically examine the utility of the widely-used Sabatier analysis to study the properties of alloys, as its utility in such complex chemical systems is unclear. By studying how the two metals in a dimer interact and whether or not these interactions raise or lower overpotentials, we aim to answer the question: Can the properties of heterobimetallic OER catalysts be predicted soley from the properties of the homobimetallics, or are the electronic interactions between metals of different chemical character too complex to make such predictions?

We then examine high-fidelity simulations of catalytic water-splitting, in which the treatment of solvation and the selection of model catalysts are key factors. We focus on OER on Nocera's CoPi catalyst [9, 150, 130, 151] to discuss these issues. Additionally, we pay particularly close attention to the kinetics of PCET events so ubiquitous in this reaction. Our hope is that we may provide a concise summary of the state-of-the-art methods and best practices for applying DFT to study catalysis in order to guide future work.

2.2 Computational Thermodynamics of Water Splitting

Water splitting catalysis is not a concerted process, but proceeds through stable intermediates. To know the intermediates in the water splitting cycle, we must first propose a mechanism. Once we propose a mechanism and enumerate the intermediates, we can calculate the thermodynamic stability of the different intermediates, and determine how stable they are in relation to one another. Though the *overall* reaction may have a potential of 1.23 V per electron transfered, *individual reaction steps* may have potentials thermodynamically uphill by a value much greater than 1.23 V (or even downhill!). The thermodynamic stability of different intermediates in the catalytic cycle depends heavily on both the nature of the catalytic surface (both the type of transition metal and uniformity) and the catalytic mechanism.

There are also reaction barriers between these steps, which determine the kinetics of electron transfer. The overpotential of the overall reaction depends on the magnitude of the largest barrier in the entire cycle. If we ignore activation energy (and thus reaction kinetics) by assuming it is small, then the overpotential of a given mechanism is determined entirely by thermodynamics. This overpotential will be an underestimate of the true overpotential, but can be a quite useful estimate, and is attainable without studying reaction kinetics in detail. In certain cases, ignoring barrier heights is justifiable: for example, PCET events, ubiquitous in water splitting, usually have small barriers and PCET rate constants often contain large quantum-mechanical tunneling prefactors [152, 153]. In other cases—cases which we will examine in detail later—it is not as justifiable, and a careful treatment of the reaction barriers is necessary.

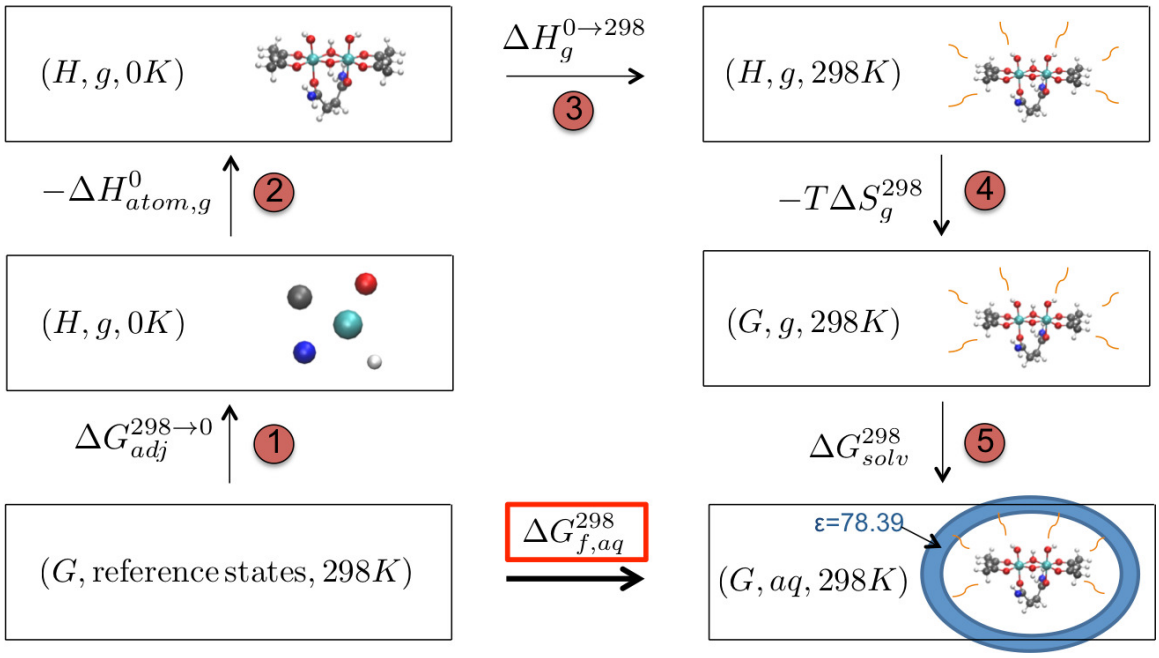

Figure 2-2: Thermodynamic cycle which can be used for the computation of $\Delta G_{f,aq}^{298}$, the aqueous free energy of formation of a molecule. The numbered steps correspond to the numbered steps in the main text. Once one references the absolute energy of a molecule to a suitable standard state (steps 1 and 2 in the cycle), one can then apply a series of corrections to the DFT-calculated internal energy to adjust the temperature from 0 K to an arbitrary temperature (step 3; here, room temperature, or 298 K); include entropic effects due to molecular vibrations (step 4); and include the effects of solvent electrostatics (including those on entropy) through a continuum dielectric model (step 5).

2.2.1 Thermodynamics Overview

Density functional theory is quite well-suited to computing relative thermodynamic stabilities among a series of compounds. Using reasonably-sized basis sets and hybrid functionals, one can get very close to "chemically accurate" heats of atomization (and, with suitable use of experimental tables, heats of formation) for compounds in the gas phase at 0 K [154, 155]. The challenges of density functional thermochemistry come with predicting free energies of formation in solution at finite temperature. For ease of notation, we shall illustrate how to compute free energies of formation at 298 K, but in practice this protocol can be applied for any temperature. Fortunately, there has been much development on this topic in recent years [156, 157, 111, 112, 118]; we shall summarize some of the main finding here.

Many authors have made use of thermodynamic cycles in order to study the thermodynamics of water splitting. Yang and Baik have developed computational methods for studying the thermodynamics of water splitting from a molecular perspective [158, 159, 160]; likewise, Norskov et al. pioneered similar methods for plane-wave computations on simulated surfaces [145, 88]. In this chapter, we shall focus in particular on one example of a protocol, shown in Figure 2-2. This particular protocol is not original or unique, but is chosen in order to clearly illustrate themes in water splitting thermodynamics which are

detailed below.

The cycle in Figure 2-2 can be used to calculate $\Delta G^{298}_{f,aq}$, from which reaction free energies–and thus redox potentials–can be computed. Many ideas in this cycle are well-established for wavefunction-based methods [154, 161, 155], and have more recently been extended to DFT methods [162]. The main idea can be summarized as follows:

1. Computation of atomization energies from DFT is straightforward, but computation of formation energies is not. We must thus first adjust the "reference" from elements in their standard state at 298 K to atoms at 0 K using empirical data from standard thermodynamic tables [163] by applying an adjustment $\Delta G^{0\to 298}_{\text{adj}}$. This will eventually allow for the calculation of free energies of formation.

2. Compute $\Delta H^{0}_{\text{atom},g}$, the gas-phase atomization energy at 0 K, from the DFT energies of the compound of interest and its constituent atoms.

3. Compute the vibrational frequencies of the molecule using a harmonic frequency analysis; from this, extract:

   (a) $\Delta\Delta H^{0\to 298}_{f,g} = \Delta\Delta H_{\text{vib}} + \Delta\Delta H_{\text{rot}} + \Delta\Delta H_{\text{trans}} + PV = \frac{1}{2}\sum_i \hbar\omega_i \coth\left[\frac{\hbar\omega_i}{2RT}\right] + \frac{3}{2}RT + \frac{3}{2}RT + RT$. Note that this includes the zero-point vibrational energy, as well as thermal contributions from higher vibrational states within the harmonic approximation. The translational and rotational contributions to the enthalpy are treated classically.

   (b) $T\Delta S^{298}_{g} = \sum_i \frac{\hbar\omega_i \coth\left[\frac{\hbar\omega_i}{2RT}\right]}{2} + RT\ln\left[\frac{1}{2}\text{csch}\left[\frac{\hbar\omega_i}{2RT}\right]\right]$. This comes from the standard statistical mechanical relationship for vibrational enthalpy.

4. Compute $\Delta G^{298}_{f,g} = \Delta H^{0}_{\text{atom},g} + \Delta G^{0\to 298}_{\text{adj}} + \Delta\Delta H^{0\to 298}_{f,g} - T\Delta S^{298}_{g}$, the gas-phase free energy of formation of the molecule at 298 K.

5. Compute $\Delta G^{298}_{\text{solv}}$; then, $\Delta G^{298}_{f,aq} = \Delta G_{f,g} + \Delta G^{298}_{\text{solv}}$.

In passing, we will note that the computation of $\Delta H^{0}_{\text{atom},g}$ can be non-trivial for transition metals, as the ground-state spin multiplicity is often incorrectly predicted by DFT [164, 165, 140]. Procedures have been tested to get the ordering of spin states correct and minimize the errors in Δ_O, the octahedral crystal field energy spin splitting [166, 167].

Furthermore, computation of $\Delta G^{298}_{\text{solv}}$ is a delicate matter. In a continuum dielectric solvation calculation, the molecule of interest is enclosed in a cavity; then, the rest of space is filled with a dielectric medium. The medium is allowed to polarize the electrons on the molecule (and vice-versa) in a self-consistent fashion, which ultimately influences the total energy of the system. Accurate solvation free energies rely largely on the quality of the cavity used as well as the parameterization of the dielectric response of the polarized continuum. Many models capture these effects with different underlying physics,

each with their own strengths and weaknesses; for a good review on the topic, we direct interested readers to the exchange in References [112] and [113].

From a $\Delta G^{298}_{f,aq}$ we can easily compute a reaction free energy, ΔG^{298}_{r}, from which we can calculate an absolute electrochemical potential,

$$E^{\circ} = -\frac{\Delta G^{298}_{r}}{nF}$$

where n is the number of electrons transferred and F is the Faraday constant. One final step must be completed before a comparison to experiment is possible: adjusting the absolute potential with respect to a reference electrode. Experimentally, redox potentials are measured with respect to a reference electrode or an internal standard reference redox couple whose absolute potential is known. Computationally, redox potentials are often calculated as the difference in (free) energy between a species with an excess electron and that same species without its excess electron. In order to compare theory to experiment, these two methods must be reconciled.

One complication which arises in these calculations is how to treat the solvation of a proton and an electron in order to get accurate free energies. The solvation free energy of both of these particles is beyond the reach of the state-of-the-art in computational chemistry; as such, alternatives must be used. One common approach is to compute an absolute free energy of solvation for each by using an experimental reference value [168, 169, 170].

Another common approach, which we use in our calcuations, is to use a *computational internal standard* (see, e.g., References [145, 171]). As an example, consider the PCET reaction

$$\mathrm{MH}^{2+} \rightarrow \mathrm{M}^{3+} + \mathrm{H}^{+} + e^{-}$$

If we assume the reaction

$$\mathrm{H}^{+} + e^{-} \rightleftarrows \frac{1}{2}\mathrm{H}_2$$

is in equilibrium ($E = 0.00\,\mathrm{V}$), then we can add the two reactions of interest without changing the redox potential of the reaction of interest, and compute the absolute redox potential of

$$\mathrm{MH}^{2+} \rightarrow \mathrm{M}^{3+} + \frac{1}{2}\mathrm{H}_2$$

In doing so, we have used a computational internal standard – namely, we have referenced all of our redox potentials to the redox potential of the atomization of molecular hydrogen. This specific choice of a reference redox couple is given a special name in the experimental literature: the standard hydrogen electrode (SHE). In principle, this referencing technique can be applied to *any* redox couple; besides

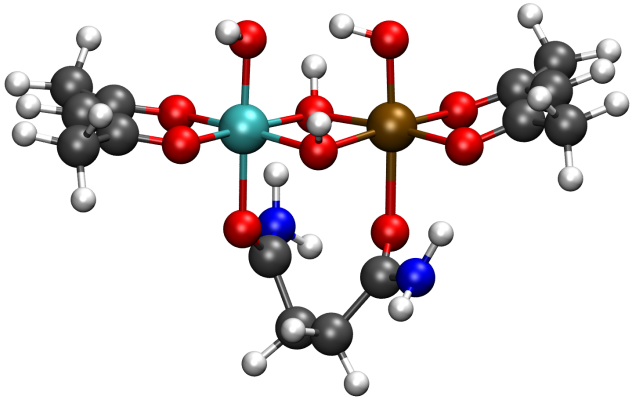

Figure 2-3: All calculations in this section were performed using the above model complex. This complex was chosen so as to (1) replicate the octahedral oxygen coordination sphere found in heterogeneous metal-oxide catalysts, and (2) fix the oxidation states of each metal. The metal oxidation states are controlled by removing a hydrogen atom (proton + electron) from the simulation on the two apical sites. In this catalytic intermediate, each metal has an -OH at its active site, meaning each metal is in the +3 oxidation state. Metal atoms are represented in cyan and brown; oxygens in red; nitrogens in blue; carbons in black; and hydrogens in white.

referencing to the SHE, referencing to the ferrocene couple has been quite popular in recent years [171]. In practice, it is most convenient to compute the redox potential of a reaction with respect to a reference that is easily experimentally accessible.

2.2.2 Computational model

In order to screen a large number of metal-oxide alloys, it was necessary for us to reduce a bulk heterogeneous catalyst down to a simpler model system, in order to reduce cost. We chose to reduce a bulk metal-oxide down to a two-metal small-molecule catalyst, as depicted in Figure 2-3. The model was chosen to allow us to examine how two transition metals (like or dislike) interact during the course of the mechanisms in Figure 2-1. The metals have octahedral oxygen coordination sphere (like in most bulk metal oxides), and the ligands were chosen to give the metals the correct oxidation state (M^{III} for both metals in the depicted intermediate). The catalytic intermediate can be changed by permuting the protonation state of the two OH ligands bound to the top of the metals, allowing us to study the entire catalytic cycle. With our model, we make the implicit assumption that only nearest-neighbor effects affect catalytic overpotentials.

We computed redox potentials following the thermodynamic procedure detailed in the previous section. All *ab initio* calculations were performed using PBE0 [98] and the 6-31g* basis set as implemented in the Q-Chem software package [172]. Geometry optimizations were performed for each intermediate in the catalytic cycle. A stability analysis was performed after each optimization to ensure the structure was at a minimum; imaginary frequencies smaller than 100 cm^{-1} were ignored. The energy at each minimum was

corrected using (1) finite temperature enthalpy corrections, and (2) vibrational entropy corrections, using a combination of the real vibrational frequencies of the intermediate (scaled appropriately for PBE0/6-31g* [162]) and the equipartition theorem. A solvation correction was also added to the energy, using the polarizable continuum model (PCM) [110, 108] with a dielectric of 78.39 (that of water at 298 K). Van der Waals radii for all elements were taken from standard tables [173] and scaled by 1.2 (1.1 for H), following established precedent [174, 175, 111, 112]. An integration grid of 74 radial points and 302 angular points were used for all SCF computations.

In order to simplify our analysis, we assumed that the resting state of the catalyst was always M-OH, and the metal in the catalytic resting state had an oxidation state consistent with the metal's most-prevalent oxidation states (III for most metals, IV for V and Cr). As the catalyst progressed through the catalytic cycle, we adjusted the oxidation accordingly—from III for M-OH and M-OOH, to IV for M-O and M-OO, to II for M-OH_2. We additionally made the simplifying assumption that each metal had a spin state consistent with a low-spin octahedral crystal field picture, and that the spins of the two metals in the dimer were ferromagnetically coupled.

We explicitly computed the redox potentials versus the standard hydrogen electrode (SHE) (and, in cases of chemical steps where there was no electron transfer, the ΔG°_{rxn}) for each step in the mechanisms shown in Figure 2-1. To be consistent with analyses done by other authors [88], we combined chemical steps (i.e., ones with no explicit electron transfer) with electrochemical steps (i.e., ones with explicit electron transfer) to reduce each mechanism down to four electrochemical steps. We performed the grouping according to the following heuristic:

- If a chemical step is downhill, assume the previous step is pre-equilibrium; group the chemical step with the previous step
- If a chemical step is uphill, it is rate-determining for the chemical transformation; group it and all other following chemical steps with the next electrochemical step.

With four electrochemical redox potentials present for each mechanism, we computed the overpotential η by taking the largest of these four potentials and subtracting from it the thermodynamic potential for water splitting against the SHE, 1.23 V:

$$\eta = E^{\circ}_{max} - 1.23\,V$$

where E°_{max} is the potential of the largest uphill step in the considered mechanisms.

2.2.3 Application to the first-row transition metal series

In order to illustrate the utility of the procedure described in the previous section, we applied the thermodynamics protocol outlined above to compute the overpotential for water splitting on a family of model

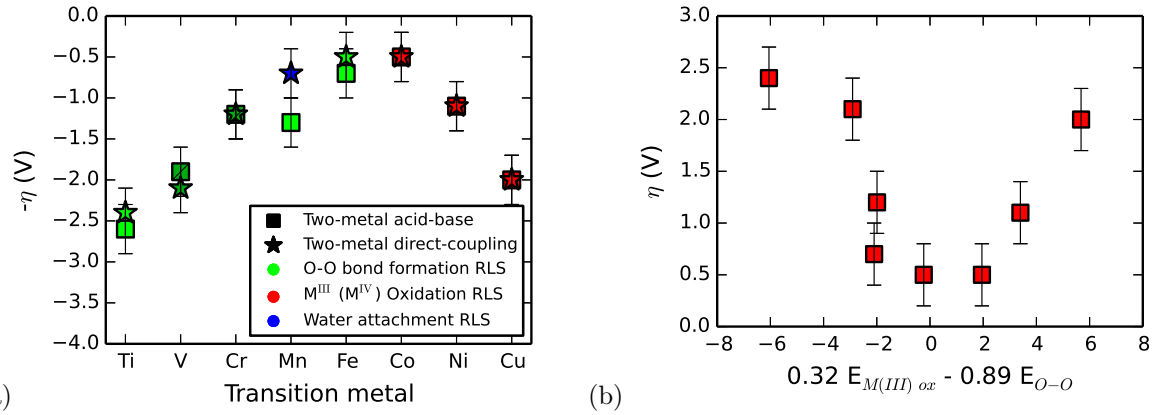

Figure 2-4: (a) Overpotentials of metal-oxide model clusters follow the expected periodic trend: as the d-orbitals fill up and the number of unpaired e_g electrons is maximized, the overpotential decreases. This is associated with a change in the mechanistic rate-determining step from O-O bond formation to metal oxidation. Somewhat surprisingly, mechanisms with chemically-similar rate-determining steps have computationally indistinguishable overpotentials, suggesting that DFT can predict overpotentials even if the assumed mechanism is incorrect (but chemically similar to the true mechanism). (b) A principle component analysis of the data used to generate (a) reveals that the coordinate along which the catalytic activity is maximized is a linear combination of the energy of M^{III} (M^{IV}) oxidation and oxygen-oxygen bond formation. Error bars represent the intrinsic error of DFT calculations on these sorts of systems, estimated generously as $\pm 0.3\,V$ [165].

molecular catalysts shown in Figure 2-3 spanning the first row of the transition metal series. The selection and design of the model catalysts are discussed in Section 2.2.2. Figure 2-4 shows our results, where we plot activity versus our descriptor, atomic number of the transition metal center. Both the acid-base mechanism and direct-coupling mechanism are considered.

As Figure 2-4 shows, the lower bound on overpotentials which we calculate using our model system has two linear regions, which intersect at a peak of activity. This trend has been observed generally for many molecular scaffolds, as explained in more detail below. Our data also serves as a scan across the first period of the periodic table for catalytic activity and its relation to mechanism. There are two interesting points to note:

- The rate-limiting step of OER shifts from oxygen-oxygen bond formation to formation of M^{IV} from M^{III} going left to right across the period
- The observed activity does not depend on mechanism to within the error of our calculations

As we go from left to right across the period, the overpotential required to evolve oxygen from a metal-oxide catalyst first decreases, and then increases again—forming a peak in activity consistent with previous experimental and theoretical results [135, 10, 142, 34]. The rate-determining step changes from O-O bond formation on the left side of the period, to M^{III} oxidation on the right side of the period; this observation is consistent with arguments regarding the origin of this periodic trend based on metal-oxygen

bond strength and d-band filling as outlined in detail in Section 2.1.

The second point raises a bit of a conundrum, as the rate of oxygen evolution *should* depend on mechanism, provided the rate-limiting step is O-O bond formation. This dependence is not observed. Regardless, the fact that the overpotentials don't vary with mechanism can be classified as a strength of this type of thermodynamic analysis, as one can predict overpotentials without worrying about getting precisely the correct mechanism. As a caveat, the converse is not true: just because the overpotential agrees with an experimentally observed value does not mean that the mechanism that is used to predict the overpotential is correct. Thermodynamic analysis is incredibly useful as a fast, computationally cheap screen of a large number of potential catalysts, but conclusions about mechanism or the chemical nature of oxygen evolution cannot and should not be drawn from such an analysis. For the remainder of this chapter, we will thus focus only on direct-coupling overpotentials for simplicity.

2.2.4 Chemical Descriptors of Reactivity

In the previous two sections, we have described the computation of the thermodynamics of the water-splitting reaction on a heterogeneous catalyst and demonstrated how thermodynamics can be used as a predictor of catalytic activity; we will now review the theoretical work that went into pioneering this approach, and the experimental work that has grown from it. Much of the initial work in this area came out of the group of Jens Norskov [88, 145, 135, 141, 34], but other theoretical groups [139, 176] and some experimental groups [10, 142] have extended the principles and used them to explain experimental observations. We do not plan on engaging in a comprehensive review of transition-metal water oxidation catalysis here; for such a review, the interested reader is directed to Reference [177].

The use of thermodynamics to describe catalysis is not a new concept: Paul Sabatier introduced his eponymous principle in 1911 [134]. The Sabatier Principle states that the optimal catalyst for a particular substrate will not bind the substrate too weakly (because if it did, the substrate would not bind to the catalyst) or the product too strongly (because if it did, the product would never be released from the catalytic surface, and the catalyst would be "poisoned"). As a special case of the discussion in the previous section, Sabatier analysis suggests that it should be possible to use thermodynamics alone to predict catalytic activity.

Norskov extended this analysis to the 21st century by proposing that one could computationally screen a large number of catalysts using DFT by focusing on the metal-oxygen bond strength. By the Sabatier principle, the perfect catalyst for water splitting should bind water "strongly" and oxygen "not too strongly"; since both bind through a metal-oxygen bond, a plot of catalytic activity as a function of metal-oxygen bond strength should have a maximum at the "optimal" metal-oxygen bond strength. In practice, one forms two calibration curves (one with a positive slope, and one with a negative slope) by calculating the metal-oxygen bond strength of a large number of species and correlating these with experimentally-

measured activities; these two calibration curves form a "volcano" of activity, with their intersection lying at the peak of the volcano. Then, one can screen large numbers of compounds computationally, and those compounds with metal-oxygen bond strengths near the peak of the volcano are predicted to have high catalytic activity.

Metal-oxygen bond strength is not the only useful chemical descriptor for Sabatier analysis. Other descriptors exist as well, including the filling of transition metal e_g orbitals—the orbitals most implicated in surface metal-oxygen bonds. Ultimately, these all boil down to the same sort of Sabatier principle: if it's easy for the substrate to form a chemical bond to the catalyst, and easy for the product to break a chemical bond with the catalyst, the catalyst will work well. Remarkably, these volcano plots work extremely well at predicting activity as a function of a simple chemical descriptor.

We performed a principle component analysis on the six free energy changes associated with the direct coupling mechanism across the metal series in order to better understand the origin of the periodic trend; the result of this analysis is shown in Figure 2-4(b). Unsurprisingly, the two potentials that best characterize the data are the potential for M^{III} oxidation (or M^{IV} oxidation in the case of V/Cr) and the energy for oxygen-oxygen bond formation. For at least the homobimetallic case, where the catalyst is comprised of only a single type of metal, a linear combination of these two energies can serve as an adequate descriptor of catalytic activity.

One major criticism of this Sabatier-type analysis is that it assumes the rate-limiting step of catalytic water splitting is either the association of the substrate with the catalyst or the dissociation of the product from the catalyst. In many cases, this is simply not true: redox steps and oxygen-oxygen bond formation have been found to be rate-limiting in certain systems [131, 136, 143, 178, 130, 8, 129, 179, 12]. Sabatier analysis is thus successful when the rate-limiting step of the catalytic cycle is a redox step, but its scope is limited to such systems; as such, the use of Sabatier analysis is often precluded by not knowing the rate-limiting step of a catalytic cycle ahead of time. Nevertheless, the technique is powerful, in that it uses *thermodynamic* information (along with an assumption about the rate-limiting step of the cycle) in order to predict *kinetics*.

2.2.5 Extracting catalytic design principles from metal alloy overpotentials

Building off of the observed trends for homobimetallic complexes, we extended our investigation to heterobimetallic complex—catalysts where two different metals can interact, altering the stability of mechanistic intermediates. To extract general catalytic design principles, we must ask: How does doping a metal-oxide with a different type of metal affect the energetics of catalysts? And how much of the properties of the heterobimetallic species can be predicted *a priori* from the homobimetallic data?

To answer these questions, we first extended the analysis presented in Figure 2-4 to metal dimers composed of all possible combinations of metals in the first period of the transition metal series; the

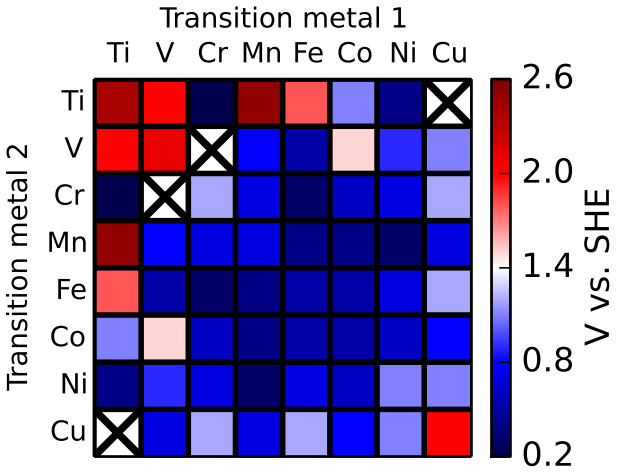

Figure 2-5: Absolute overpotentials of all heterobimetallic complexes studied, in volts with respect to the standard hydrogen electrode. No data is reported for two complexes, Ti-Cu and V-Cr, as certain catalytic intermediates in each case fell apart upon geometry optimization. Additionally, Cr-Mn through Cr-Ni complexes did not remain octahedral during O-O bond formation, and Mn-Cu was found to have a different resting state (Mn-O Cu-OH_2) than the other complexes studied. While certain points appear questionable (especially Ti-Ci), we observe reasonably low overpotentials near the center of the matrix, begging the question: is there a chemical descriptor that we can use to predict alloy overpotentials *a priori*?

overpotentials associated with these dimers are presented in Figure 2-5. We limit the scope of our discussion for the heterobimetallics to the direct coupling mechanism. The diagonal elements of the pictured overpotential matrix are the direct coupling overpotentials depicted in Figure 2-4.

Of greater interest are the off-diagonal elements, which represent heterodimer overpotentials. Some of these have lower overpotentials than the homobimetallic materials, suggesting higher catalytic turnover. Of the screened materials with small overpotentials, we suspect that Ti-Cr and Ti-Ni may be questionable, as titatium(III) oxide catalysts are known to be inefficient due to their large band gaps [180]. Additionally, many of the chromium dimers required a significant distortion of the ligand field in order to accomodate O-O bond formation. These materials aside, none of the rest of the materials screened showed any large issues, so we expect the overpotentials of materials containing Mn-, Fe-, Co- and Ni- to be chemically relevant—to within the accuracy of our DFT calculations. We are unable to, e.g., order the overpotentials of Ni-Fe, Ni-Co, and Co-Fe with respect to one another, because they are all the same to within the error of our calculations; the ordering presented here may thus be inconsistent with experimental observations [181].

To understand the origins of the overpotentials presented in Figure 2-5, we examine qualitatively which step in the water splitting cycle is the rate-determining step. The results are presented in Figure 2-6. While the mechanism of homobimetallic complexes (see Figure 2-4) shows a clear trend—shifting from an O-O bond formation RDS to a metal oxidation RDS across the period—the corresponding analysis of

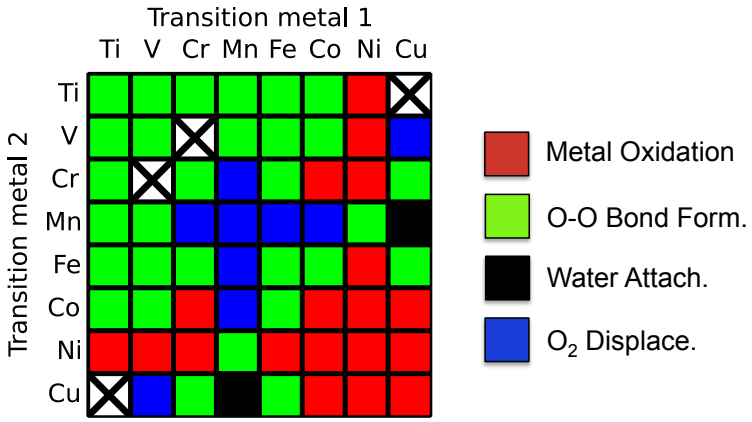

Figure 2-6: Rate-determining steps of the oxygen evolution reaction on transition metal-oxide dimers. While the homobimetallics showed a clear trend, the RDS of heterobimetallic species is much more varied. A Sabatier analysis thus cannot be applied in a straightforward manner to the heterobimetallics.

the RDS of heterobimetallic complex does no such thing. O-O bond formation is the predominent RDS: it accounts for the bottleneck step in over half of the complexes studied. In spite of this observation, nickle-containing complexes have a tendences to have metal oxidation as the RDS, and manganese-containing complexes water attachment. Because of these frequent blips, a Sabatier analysis is not straightforward; we will thus focus our discussion on trying to understand the origin of these trends and searching for a descriptor that can be used to inform catalytic design.

2.2.5.1 Metal Cooperativity

We recapitulate that our desire in this chapter is to understand how much of the properties of the heterobimetallics can be predicted solely from the properties of the homobimetallics, and how a mapping of one on to the other can inform rational design. We begin our analysis by quantifying how much two unlike metals cooperate with one another to lower overpotentials. With the exception of O-O bond formation, each step in the direct-coupling mechanism is local: it occurs on only one of the two metals in the complex. As a measure of cooperativity, then, we ask: for a RDS occuring primarily on metal A in the transition metal dimer A-B, what is the difference between the A-B overpotential and the A-A overpotential? Or, in the case where the RDS is O-O bond formation, what is the difference between the A-B overpotential with the average of the A-A and B-B overpotentials?

Figure 2-7 shows the results of this analysis. We observe, generally, that in the lower-right corner of the table—where metal(III) oxidation is the RDS—metal dimers tend to behave weakly anticooperatively or independently. In the region near Mn-Mn—where water attachment is the RDS—metal dimers tend to behave weakly cooperatively or independently. By contrast, in the rest of the table—where O-O bond formation is the RDS—metal dimers tend to cooperate strongly.

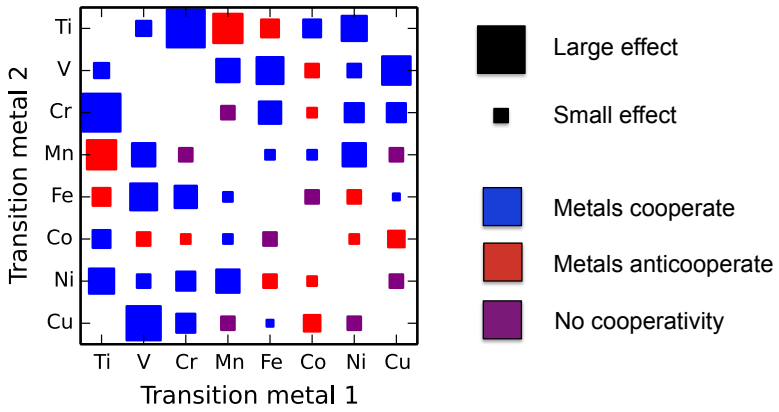

Figure 2-7: For each metal pair, we compute a naive estimation of the overpotential by taking either (1) the homobimetallic overpotential of the site associated with the chemistry of the RDS, or (2) the average of the two homobimetallic overpotentials for the alloy in question if the RDS is O-O bond formation. By plotting the difference between the heterobimetallic overpotential and our naive estimate, we extract a measure of how cooperative the metals are in the heterodimers. Blue squares represent a positive effect (i.e. the metals work together to lower overpotentials) and red squares represent a negative effect. The size of the square corresponds to the magnitude of the effect.

These observations are consistent with our chemical intuition that when chemistry is local (i.e. the RDS only involves one metal site directly), the other metal center tends to act as a spectator, only weakly influencing the RDS. We point out an exception to this rule in the case of Ni doping (where the RDS is predominantly metal(III) / metal(IV) oxidation but we observe strong cooperativity). This exception can be understood by examining the individual redox potentials for Ni oxidation versus M oxidation for each other metal in the series, as plotted in Figure 2-8. The RDS in this series does actually change from Ni oxidation to M oxidation across the period. This change in RDS inflates our cooperativity metric towards the left half of this series, as overpotentials are being drastically lowered by changing the RDS from O-O bond formation to Ni oxidation.

O-O bond formation, on the other hand, is inherently nonlocal, and thus requires more than sum of parts. Interestingly, in this case, we observe that overpotentials on heterodimers which arise due to large barriers for O-O bond formation are reduced significantly compared to the average of the homodimer overpotentials, indicating nonequal contributions from the two metals in the radical coupling step. Overall, the results in Figure 2-7 tell us how many of the overpotentials presented in Figure 2-5 could have been guessed looking only at the overpotentials in Figure 2-4. In cases where cooperativity is small, homobimetal overpotentials are a good predictor of alloy overpotentials; in cases where cooperativity is large, they are not a good predictor. Thus, we must continue our search for a good universal predictor of alloy catalytic activity.

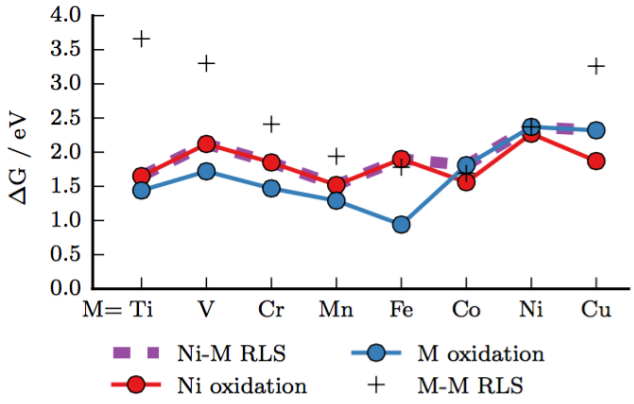

Figure 2-8: Examining Ni-M dimers across the series of metals reveals an interesting trend: overpotentials of Ni-M species are generally lowered with respect to M-M species because the O-O bond formation energy is substantially lowered, making a metal oxidation event the rate-determining step. For the first half of the series, Ni oxidation is higher in energy than M oxidation, making it the RDS; later, this flips, and M oxidation becomes the RDS.

2.2.5.2 Metal Communication

We next ask the question: Is an *a priori* universal predictor of heterobimetallic activity even possible, or do the metals interact to such a significant effect that finding such a descriptor is hopeless? We purport to answer this question by measuring *communication* between the metals. As a metric for communication, we must look not only at how much the redox potential of the RDS changes going from a homobimetal-based description of redox potentials to a heterobimetal-based description, but also at how much *every* redox potential changes.

For this analysis, we use all six free energy changes occuring in the direct coupling cycle presented in Figure 2-1, as combining chemical and electrochemical steps obfuscates metal communication. For each metal pair, we look at the two sets of homobimetal redox potentials (and free energy changes) for the two metals in the heterodimer. We compute six naive overpotentials for the heterodimer using the following procedure:

1. First metal oxidation is the lower of the two homodimer metal oxidation potentials
2. If the first oxidation occurred on the left metal, take the second metal oxidation potential from the right metal, or vice-versa
3. Average the two homodimer O-O bond formation free energies
4. Take the lower of the two homodimer free energies for water attachment
5. If water attachment occurred on the left metal, take the third redox potential from the left metal, or vice-versa

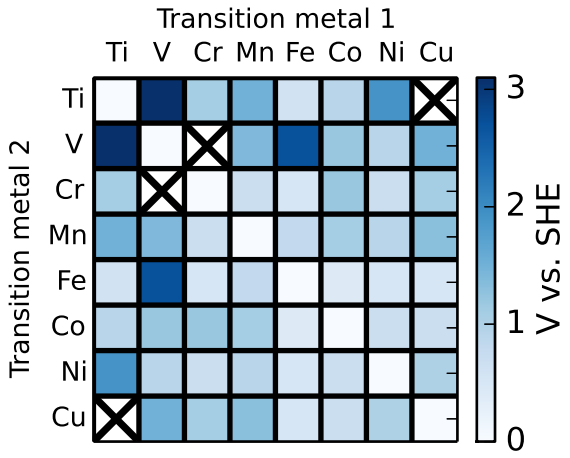

Figure 2-9: We wish to determine whether or not any information about heterodimer overpotentials can be surmised by looking at only the homodimer data. For each heterodimer, we constructed a series of 6 chemical and electrochemical energies / redox potentials assuming the metals do not interact (except for O-O bond formation, where they interact in a mean-field sense). Concretely, we took the lower of the two homodimer energies for the two steps where there is a choice to be made (the initial metal oxidation, and the site of water attachment), and followed the chemistry of the mechanism through for the rest of the energies. The RMSD of these six energies from the heterodimer energies is shown, where the homodimers by definition have an RMSD of 0 V.

6. If water attachment occurred on the left metal, take the final redox potential from the right metal, or vice-versa.

These six redox potentials (and free energies) form a naive picture of the thermodynamics of catalysis on a heterodimer: If the metals do not communicate much or at all, we would expect the true heterodimer potentials / energies to be very close to these naive potentials / energies; if the metals communicate a lot, we would expect the true heterodimer energies to deviate substantially from the naive energies.

We measure the root-mean-square deviation (RMSD) of the true redox potentials from the naive redox potentials of all six steps for each metal dimer; the results are plotted in Figure 2-9. We wish to make two observations about the data. First, overall, most of the metals in the heterodimers communicate fairly substantially; in all of our data, the smallest RMSD is 0.4 V (for Co-Fe) and the largest is 3.1 V (for Ti-V), and the mean RMSD is 0.9 V with a standard deviation of 0.7 V. Second, the communication data show only a weak correlation with the cooperativity data in Figure 2-7. We observe that when the RDS is metal oxidation or water attachment, the metals on average communicate less than when the RDS is O-O bond formation (again, confluent with our chemical intuition); any deeper insights are difficult to perceive.

From these observations, we conclude that even if metals communicate, it isn't necessarily in a way that affects cooperativity—sometimes, communication just affects redox potentials that aren't the RDS. While this indirectly affects overpotentials (as raising the potential of one step necessarily lowers the

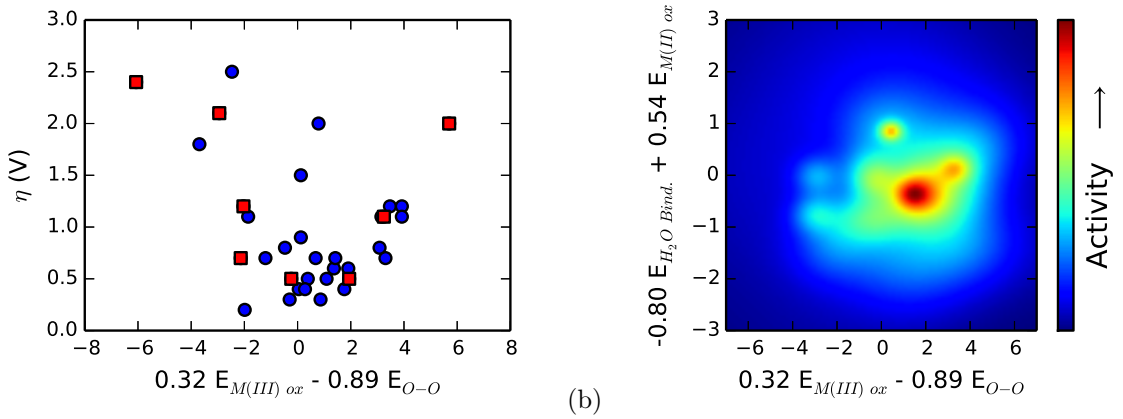

Figure 2-10: A principle component analysis of the six free energy differences computed for all compounds studied reveals two key coordinates which can be used as descriptors of catalytic activity. (a) Examining only the first of these two coordinates does not show a peak in activity, only a downward trend (especially once the homobimetallic points, pictured as red squares, are excised from the data). (b) Looking at both coordinates reveals a clear volcanic island of activity. We thus observe that in general, four energies are needed to characterize the activity of a catalyst: the ionization potentials of metal(II) and metal(III); the metal - water bond dissociation energy; and the O-O bond formation energy.

energy of at least one other), it does not necessitate the lowering of overpotentials. We can additionally conclude that while there is overall a lot of metal-metal communication, since it does not necessarily affect the RDS, it should (in principle) be possible to extract descriptors of catalytic activity from the data.

2.2.5.3 Sabatier Analysis

Given the complexity of all that we've discussed so far, we return to our original question: Does anything we know about homobimetals help predict heterobimetal behavior, or does the Sabatier analysis break down due to the large amounts of communication and cooperativity in certain metal pairs? We perform a principle component analysis on the data [182]—again using all six free energy changes implicated in the direct coupling catalytic cycle instead of folding chemical steps into electrochemical steps as discussed previously. The results are shown in Figure 2-10. The principle eigenvector of the covariance matrix of redox potentials (averaged over the ensemble of all metal pairs) is, in full,

$$e_1 = 0.32E_{M(III)\,ox1} + 0.20E_{M(III)\,ox2} - 0.89E_{O-O} + 0.20E_{H_2O\,add} + 0.18E_{M(II)\,ox}$$

with eigenvalue 6.13. This coordinate can be approximated by its two largest values,

$$e_1 \approx 0.32E_{M(III)\,ox1} - 0.89E_{O-O}$$

Plotted versus this linear combination of potentials, the traditional Sabatier analysis breaks down

(Figure 2-10(a)): the overpotentials decrease along this coordinate, but do not appear to increase again after a minimum is reached (especially if the homobimetallic data are excised).

We do, however, recover Sabatier-like behavior if the second eigenvector (eigenvalue 1.20) is included; in full, this eigenvector is

$$e_1 = 0.25E_{M(III)\,ox2} - 0.80E_{H_2O\,add} + 0.54E_{M(II)\,ox}$$

which can again be approximated by its two largest components,

$$e_2 \approx -0.80E_{H_2O\,add} + 0.54E_{M(II)\,ox}$$

The correlation of overpotential with these two coordinates is shown in Figure 2-10(b). A volcano of activity emerges along these two coordinates where none existed along only the first. Additionally, all other eigenvalues of the covarience matrix are smaller than 1, suggesting that only the two coordinates presented are chemically relevant for exploring design space.

2.3 Modeling water splitting kinetics

DFT thermochemistry can often reproduce trends in catalytic activity, as illustrated by the analysis in the previous section. This level of modeling can provide actionable insight without a detailed understanding of the mechanism of catalytic activity. However, to determine plausible reaction pathways or to predict the activity of novel catalyst designs, a mechanistic understanding of the catalytic cycle is indispensable. Strictly thermochemical approaches neglect the role of kinetics, which must be incorporated into the simulation strategy for mechanistic studies. In this section, using recent computational studies of Nocera's CoPi cobalt oxide catalyst [9, 150, 130, 151] as a basis for discussion, we discuss the computation of redox potentials in solution and the insight it can provide into kinetics of catalytic water splitting.

2.3.1 Catalyst model selection

The active form of the aqueous CoPi catalyst is a cobalt oxide cluster possessing pendant water and hydroxo ligands. The catalytic cycle of CoPi is comprised of a series of four oxidations of the CoPi-water complex coupled to the formation of an O-O bond, release of O_2 from the catalytic surface, and regeneration of the catalyst resting state by water addition [129]. Identification of the rate-determining step (RDS) of the CoPi catalytic cycle is a central goal of computational studies. The RDS controls the turnover rate, and its identification helps narrow the range of plausible mechanisms. For chemical (bond-breaking and forming) steps in the cycle, the activation free energy $\Delta G^{\ddagger}$ is the key quantity to be determined, while for redox events, the ET kinetics are governed predominantly by the redox potentials

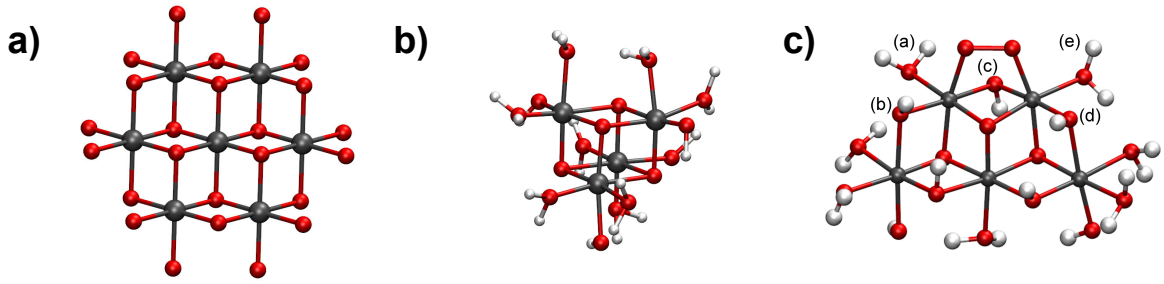

Figure 2-11: (a) 7-center model of the CoPi surface (protons omitted), consisting of edge-sharing CoO_6 octahedra and supported by EXAFS studies. (b) Cubane Co_4O_4model of the CoPi catalyst, used in Reference [129]. (c) O-O bonding in the 5-center CoPi model, which was used for the additional calculations described in this chapter. Letters identify terminal oxo (a,e) and bridging μ-oxo (b,c,d) protons available for abstraction in the third and fourth PCET events.

of the catalyst.

Given the extensive network of single-step chemical reactions that can take place in, on, and around the CoPi catalyst, an exhaustive exploration of all possible water oxidation pathways is possible only for model systems of modest size. EXAFS studies support structures as small as the 7-center cobaltate model [183] shown in Figure 2-11(a), but initial mechanistic studies of the CoPi catalyst focused on a minimal 4-center cubane model, Figure 2-11(b). This model permits the quantification of both acid-base and direct coupling mechanisms while satisfying Occam's razor by limiting the investigation to the simplest mechanism capable of explaining experimentally observed features.

To consider additional PCET pathways not testable with the cubane model, we introduced a 5-center model, Figure 2-11(b), shown here in the state immediately following two PCET events and O-O bond formation. Here, terminal oxo (labels a, e) and μ-oxo protons (labels b, c, d) are both available for abstraction by PCET. The 5-center model is thus capable of distinguishing among a larger variety of PCET pathways.

A related study of water splitting on CoPi [184] raised the important issue of identifying the lowest energy protonation state of the model complex. Using a different computational model from the one used in Reference [129], Li et al. found a lower-energy protonation state for the 4-center catalyst, containing protonated μ-oxo bridges. DFT MD simulations of representative Co_6O_{23}, Co_7O_{24}, and Co_7O_{26} clusters by Mattioli et al. also suggested a role for protonated μ-O atoms in the resting state [185]. Their model structures were derived from the known crystal structure of $LiCoO_2$ and included a linked pair of perfect Co_4O_4 cubanes; a pair of defective cubanes (identical to the 7-center model discussed above); and a mixed case. The structural differences in these studies lead to differing conclusions about the O-O bonding mechanism in CoPi, as discussed below.

2.3.2 Treatment of solvent

In practice, DFT-derived reduction potentials can depend strongly on the level of theory at which the solvent is treated, especially for protic solvents like water. This dependence has been investigated extensively [112, 186, 187, 118], supporting an informed decision about how to model the aqueous environment of the CoPi catalyst. The CoPi water oxidation studies of Li et al [184]. employed a Poisson-Boltzmann implicit solvent model [188], based on the success of this approach for modeling biological water oxidation [125]. However, in the case of water oxidation by the CoPi catalyst, the potentially important role of hydrogen-bonding at the surface of the catalyst is a strong argument against the use of implicit solvation models which do not account for hydrogen bonding across the artificial solute-solvent interface.

In a benchmark study of reduction potentials of aqueous transition metal clusters, we showed that DFT (using the B3LYP functional) [97] with the conductor-like screening model (COSMO) [109] successfully predicts experimental reduction potentials for organic molecules, metallocene complexes, and transition-metal complexes in various solvents, with the key exception of octahedrally coordinated aqueous transition-metal complexes [118]. The calculated reduction potentials of aqueous transition-metal complexes, shown in blue, are nearly all overestimated by more than 1 V, in contrast to root mean square deviations (RMSD) of 0.2-0.4 V between calculated and experimental reduction potentials for all other classes of complexes. While such errors were acceptable when extracting qualitative trends and design principles, they are less desirable when we wish to pin down kinetic barriers quantitatively.

A polarizable QM/MM (QM/MMpol) treatment showed significant improvement, achieving a similar RMSD to the other systems in implicit solvent. In the QM/MMpol model, electronic polarization of the solvent due to redox events was accounted for explicitly [116]; its inclusion proved to be essential for reproducing the experimental reduction potentials. The QM/MMpol approach overcomes the failures of implicit solvation for aqueous transition metal complexes, but at significant computational cost. By isolating the effects of solute flexibility and of temporal solute-solvent correlation on the solvation energy, we showed that hydrogen-bonding effects are the primary feature absent from the implicit solvation models which account for most of the error in the calculated reduction potentials.

The CoPi studies of Mattioli et al. also rely on an explicit representation of the solvent, treating the surrounding water at the same DFT level of theory as the catalyst itself [185, 189]. This even-handed approach accounts for hydrogen-bonding effects—to the extent that the underlying functional successfully describes noncovalent interactions—while naturally including both electronic and orientational polarization of the solvent after a redox event. The only clear disadvantage of such an approach is computational cost. In the next section, we will explore how the model selection and solvent considerations above influence the calculation of redox potentials and reaction profiles for water oxidation in CoPi.

2.3.3 Computational methodology

To calculate redox potentials in the QM/MM approach, we ran equilibrium MD trajectories of the solvated catalyst both before and after the PCET event. The change in free energy was computed by sampling configurations from both the oxidized and reduced ensembles; calculating the ensemble-averaged energy gaps between oxidized and reduced states, E_{ox} - E_{red}; and finally taking the mean of these two energy gaps:

$$\Delta G = \frac{1}{2} \left(\langle E_{ox} - E_{red} \rangle_{ox} + \langle E_{ox} - E_{red} \rangle_{red} \right) \tag{2.1}$$

This working equation stems from the technique of thermodynamic integration and assumes that free energy changes are linear in the thermodynamic integration parameter, which can be thought of as a reaction coordinate for PCET [118].

To calculate redox potentials for the third and fourth PCET events in CoPi, we employed the QM/MM approach described in the Supporting Information of Reference [129] with some minor modifications.

For QM/MM simulations, the CoPi catalyst and all pendant ligands, including water, are treated quantum mechanically with DFT (PBE0 functional) and the TZVP basis set [190]. The catalyst was surrounded by 216 SPC/E water molecules [191] in a periodic box (length 37.2 Å). The QM/MM interaction potential is derived from the usual electronic embedding scheme [192]; for van der Waals interactions, hydrogen and oxygen parameters are taken from the SPC/E model while cobalt parameters are taken from UFF [193]. All QM/MM MD simulations were performed through the CHARMM/Q-Chem interface [194].

Initial configurations for QM/MM MD simulations of the 3rd and 4th PCET events were sampled from NVT-equilibrated configurations of the previous (O-O bonding) step in the catalytic cycle. For each protonation state (as described in Figure 2-12), between 2 and 6 independent QM/MM MD simulations were performed with a velocity Verlet integrator, a timestep of 1 fs, and a Nosé-Hoover thermostat to maintain a simulation temperature of 298 K. The SHAKE algorithm [195] was used to constrain highfrequency vibrations in SPC/E water during the dynamics. After collecting at least 2.5 ps of dynamics from each trajectory, the first 0.5 ps were discarded and snapshots were sampled at regular intervals of 20 fs for the calculation of energy gaps.

Vertical energy gaps between neutral and ionized species were computed using a polarizable QM/MM model. Electronic polarization of the solvent was described through a modified SPC/E water model described in previous work [129], which employs a Drude particle on oxygen whose polarizability parameter is taken from the SWM4-DP water model [116]. Vertical energy gaps are adjusted for referencing with respect to the standard hydrogen electrode (4.43 V, pH 0) by subtracting 4.43 V and 59 mV for each pH unit.

2.3.4 Redox potentials for the CoPi catalyst

In previous work, we showed a direct coupling pathway for O_2 bond formation on the 4-center CoPi model of Figure 2-11(b), where an O-O bond formed spontaneously between a pair of terminal oxo ligands after two PCET events [129]. The redox potentials for these two PCETs, computed using the QM/MMpol approach described in the previous section, are 0.8 V and 1.4 V, respectively. Here we report redox potentials for the third and fourth PCET events, assuming that both take place before water addition and O_2 displacement. The same QM/MMpol strategy used for the first two PCET events is employed here: the QM region consists of the CoPi model complex including all hydroxyl and water ligands, surrounded by water treated through the MMpol model. Redox potentials were obtained through conformational sampling of the ionization potential and electron affinity of the catalyst in different oxidation states, as described in the Section 2.3.3. All possible pairs of deprotonation sites, indicated in Figure 2-11(c), were considered.

The pathway with lowest determined overpotential consisted of deprotonation of a water ligand (a) at 0.2 V, followed by deprotonation at a μ-oxo site (b) at 1.2 V; the complete series of redox events is summarized in Figure 2-12. For the fourth PCET, deprotonation of a second water (e) was calculated to require an additional potential of 0.4 V above the (a,b) pathway. Interligand proton transfer on CoPi is also relatively facile in the simulations, evidenced for example by proton transfer from water to a hydroxyo ligand preceding the fourth PCET in Figure 2-12. The simulations show a lower redox potential for the fourth PCET than for the second PCET preceding O-O bond formation. Therefore it is feasible for all four PCET steps to precede water addition, making O_2 release a plausible rate-limiting step. This finding helps rationalize the Sabatier-type analysis discussed previously by supporting its underlying assumption that the rate-limiting step is a catalyst-reactant association or dissociation process.

The prediction of water splitting kinetics in catalysts like CoPi ultimately hinges on three capabilities: simulating solvent dynamics, accurately computing redox potentials, and estimating reaction free energy barriers. The computational investigations presented here each addressed these requirements in slightly different ways, but they collectively point to several points of consensus about CoPi. Mattioli et al. carried out direct Car-Parrinello MD simulations of a solvated CoPi complex including full DFT treatment of water. Redox processes were simulated by removing electrons at fixed time intervals of 1 ps [189]. The timescale is incompatible with the relaxation time of water [196]. but allowed for real-time simulation of the full sequence of redox events within DFT. The simulations did not show spontaneous formation of terminal Co(O) groups until all four electrons were removed, requiring an overpotential of 1.87 V for a Co_6O_{23} model catalyst. Li et al. considered redox events on the cubane Co_4O_4 model using implicit solvent and found a slightly lower barrier for water attack than for direct coupling after the first two oxidations [184].

All of the studies agree that the 4-center model for CoPi cannot fully account for all experimental

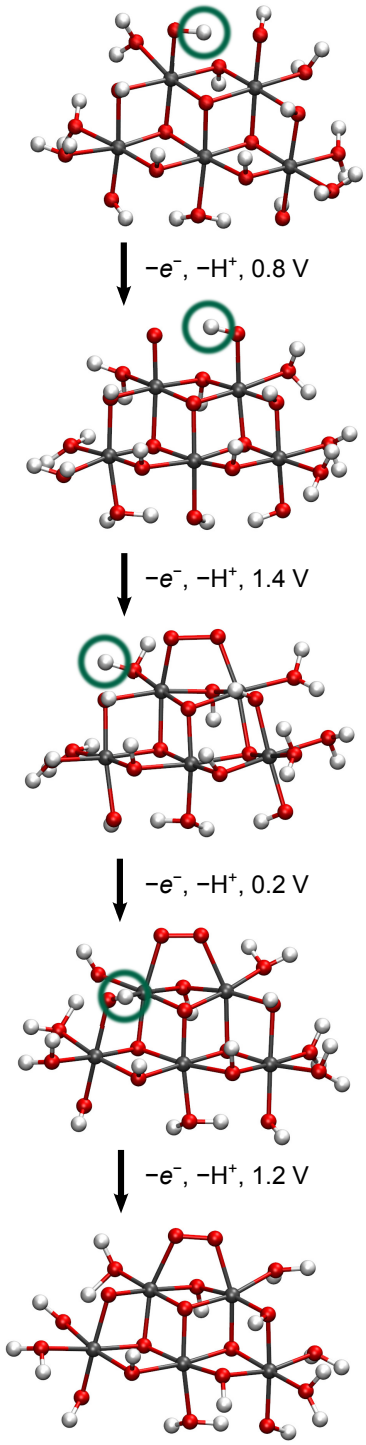

Figure 2-12: Oxidations and bond rearrangements on CoPi leading up to water addition and O_2 release, assuming a direct coupling mechanism across neighboring terminal oxos. The lowest redox potential identified for each step is shown with the corresponding deprotonation site.

observations, especially the distribution of bond lengths determined by X-ray absorption spectroscopy. Regarding the sequence of redox processes, the QM/MM and CPMD studies agree on several points: (1) O-O bonding can proceed after loss of as few as two electrons, though losing additional electrons helps; (2) pre-equilibrium steps involving proton transfer are likely, as intramolecular proton transfer is facile on the surface of CoPi; and (3) direct coupling, not an acid-base mechanism, is responsible for O-O bonding in the Co_4O_4 model cluster. It is of course possible that multiple mechanisms contribute to the overall performance of a heterogeneous, self-assembled catalyst such as CoPi.

The direct coupling mechanism supported by the QM/MM and CPMD studies is at odds with the implicit solvation study of Li et al., where O-O bonding occurred between an oxo group and an attacking water molecule. This difference underscores the importance of treating catalyst-solvent interactions explicitly in order to accurately model catalytic water oxidation. For this reason, progress in theoretical modeling of water oxidation is closely linked to the broader challenge of developing high-quality theoretical models for water and its interactions with solutes.

2.4 Conclusions

Artificial water oxidation catalysis is poised to become a commercially significant technology in the near future. A detailed understanding of the structure and reactivity of candidate catalysts will play an essential role in further catalyst design and optimization. In this chapter we have discussed the current state of the art in electronic structure calculations of artificial water oxidation catalysts, with an emphasis on how DFT is used to explore reactivity trends and underlying mechanisms. DFT thermochemistry can be employed to quantify chemical descriptors of reactivity, and these descriptors reproduce experimentally observed "volcano plots" describing the dependence of catalytic activity on the constituent transition metal. The proper incorporation of solvent effects remains a challenge, but polarizable QM/MM and full QM/MM models of the surrounding water provided insight into the sequence of PCET events in the catalytic cycle of the CoPi water oxidation catalyst.

We conclude by returning to the central question of this chapter: Can we predict the overpotentials of metal oxide alloys by only looking at properties of individual metal oxides? We answer the question with a qualified "yes." As we pointed out in Sections 2.2.5.1 and 2.2.5.2, the metals tend to communicate and cooperate when the RDS is O-O bond formation, but they do not tend to be as communicative when the RDS is something else. Additionally, in Section 2.2.5.3, we present two generalized coordinates that are both blind to which step is the RDS and predictive of catalytic activity.

Based on these two central results, we propose that a descriptor of catalytic activity can be attained by using the generalized coordinates in Section 2.2.5.3 *and relevant homogenous metal-oxide energies.* Computation of the M(II) and M(III) ionization potentials and M-OH_2 bond enthalpies for two indepen-

dent metal-oxide catalysts should be able to provide a reasonable stand-in for the same energies in an alloy, as each corresponds to an event that occurs relatively locally on a single metal.

Unfortunately, the fourth and most significant energy involves—that of O-O bond formation—is required to attain an accurate descriptor of activity and cannot be readily extracted from only the pure metal data. Nevertheless, we believe that through the work presented in this chapter, we have reduced the cost for a computational screen of heterometallic oxides. Previously, the ground-state energies of 9 OER intermediates on a heterometallic catalyst were required to construct a complete energy landscape for the catalytic cycle in order to extract an overpotential. Now, based on the analysis provided, only 2 intermediates are required to compute the energy of O-O bond formation on the heterometal catalyst. This energy, along with a handful of energies readily computed from monometal-oxide catalysts, can be used along with the coordinates described in Section 2.2.5.3 to screen potential bimetal-oxide catalysts for OER activity.

The ability of theory and computation to address the mechanism of water oxidation catalysis is largely tied to developments in DFT and other electronic structure theories. Current shortcomings relevant to the artificial water oxidation problem include the treatment of dispersion effects, reaction barrier heights, and the underlying issue of self-interaction error. All of these areas are very active topics of research, and there is good reason to expect steady improvement in the accuracy of DFT models for water oxidation catalysts in the coming years.

2.5 Acknowledgement

The work described in this chapter was carried out with Takashi Tsuchimochi, Lexie McIsaac, Tim Kowalczyk, and Lee-Ping Wang, who are co-authors of Ref. [19].

Chapter 3

Resummed Memory Kernels in Generalized System-Bath Master Equations

3.1 Introduction

Generalized master equations are useful constructs in chemical physics for solving problems that involve a few "system" degrees of freedom interacting with a large number of "bath" degrees of freedom, like when considering electron transfer in solution. When used to monitor time evolution of system populations, these equations generally have the form

$$\dot{\mathbf{P}}(t)=\int_0^t \mathbf{K}(t-s)\mathbf{P}(s)ds \tag{3.1}$$

where $\mathbf{P}$ is a vector containing the populations of the various system states and $\mathbf{K}$ is a matrix controlling the (non-Markovian) flow of populations among states *without explicitly referencing the bath degrees of freedom*; this time-nonlocal matrix $\mathbf{K}$ is often referred to as the *memory kernel*. Such equations allow us to solve explicitly for system observables while only taking into account aspects of the bath that directly influence the system. Formally equivalent to generalized Langevin equations and path integral methods, generalized master equations allow for a somewhat phenomenological description of the bath and are thus useful when detailed statistical information about the bath is not known *a priori*.

Many different methods have been proposed that solve the system-bath dynamics problem to varying extents; unfortunately, none are both robust and general. Due to the existence of the influence functional for harmonic baths [197], path-integral-based numerical methods have been quite successful for this

problem [66, 67]. Additionally, there are also formulations of this problem that are not fully quantum-mechanical. The simplest formulation is a mixed quantum-classical set-up where the system (and perhaps a few important bath degrees of freedom) are treated quantum-mechanically and (the rest of) the bath is treated classically. There are several detailed reviews of these methods including their successes and shortcomings in the literature [198, 199, 200].

In recent years, several alternative methods not based on generalized master equations have been proposed that successfully solve the quantum dynamics problem for certain classes of system-bath Hamiltonians. One method of particular merit is the multi-configuration time-dependent Hartree approach [201, 202, 203], which in and of itself is limited to treating only a few degrees of freedom exactly but can be quite powerful when coupled with other degrees of freedom semiclassically [69, 68]. Even more recently, hierarchical equation of motion (HEOM) approachs to this problem have been proposed which in principle give numerically exact results [71, 72]. Unfortunately, these state-of-the-art numerical methods are not general in that they require very specific assumptions about the nature of the bath. They can also often be extremely slow to converge, especially at low temperatures [204].

In the general case of a generalized master equation of the form of equation 3.1, $\mathbf{K}(t)$ cannot be obtained; often, we must resort to using perturbation theory to gain information about $\mathbf{K}(t)$. In cases when the system-bath coupling is weak, one can expand the Hamiltonian perturbatively in the system-bath coupling and utilize the tools of Redfield theory to obtain a solution [205, 206]. In the opposite regime, when the strength of the system-bath coupling is much stronger than the strength of the intrasystem electronic couplings, one can first apply a *polaron transform* and then expand the kernels perturbatively in the system-bath coupling. The original polaron transform was proposed for application in solid state physics [207], but can be particularly effective for system-bath dynamics problems in the special case of a harmonic bath [208, 209, 210, 211, 212]. Recently, for particular classes of harmonic bath models, polaron transformations have been used effectively to solve the quantum dynamics problem in an effectively nonperturbative fashion [213, 214].

In other treatments, the memory kernel is expanded in a power series in the electronic coupling V. A truncation of this series at second order results in the famous non-interacting blip approximation (NIBA) [62, 64, 208], which gives a second-order approximation of the dynamics and Fermi's Golden Rule rate constants.

Additionally, many groups have worked with this expansion out to fourth order in certain limits. The Cao group has worked extensively with fourth order rate constants (given by $\mathbf{k} = \mathbf{K}(\omega = 0)$)[215, 216, 217], inspired by the analytical work of Mukamel [218] and Silbey [219]. Reichman, working with Silbey and Neu, derived analytical results for dynamics in the low-temperature limit for certain classes of baths [220, 221, 65]. Finally, a fourth-order correction to Redfield theory that is guaranteed to obey detailed balance has been derived [222]; however, it requires making additional assumptions about the system-bath

coupling. Despite this work, no one has studied detailed short-time two-state *dynamics* for a system-bath Hamiltonian governed by a generalized master equation.

In this chapter, we examine for the first time the dynamics generated by a resummed memory kernel correct to fourth-order. We consider in detail the spin-boson Hamiltonian [62], for which it is possible to derive analytical expressions for $K^{(2)}$, $K^{(4)}$, and (in principle) all higher-order coefficients. We present what we believe to be a novel derivation of $K^{(4)}$ for this problem that can be easily generalized to derive both higher-order terms and non-Condon versions of $K^{(2)}$, $K^{(4)}$, etc. with electronic coupling linear in the bath coordinate. We then present numerical results where we evaluate our analytical memory kernels using a model spectral density. In our numerical results, we compare several methods to resum $K^{(2)}$ and $K^{(4)}$ into a kernel K containing **all** orders of the electronic coupling—a necessary procedure to prevent long-time divergence of the populations. Finally, we show how we can almost trivially force our resummed kernels to obey detailed balance, giving the correct infinite-time equilibrium populations. Our aim is to build towards a general, robust, systematically-improvable system-bath approximation for molecular systems in condensed phases.

3.2 Theory

3.2.1 Generalized Master Equation Formalism

Despite its simplicity, the brute-force numerical propagation of a density matrix under the influence of a system-bath Hamiltonian is not possible, as the computational cost of such a propagation scales exponentially with the number of bath modes represented; hence, generalized master equation approaches become useful. Unfortunately, the memory kernels of equation 3.1 are as computationally intractable as the propagator.

To approach this problem, we can use time-dependent perturbation theory. For simplicity, we shall restrict our discussion to the special case where our system contains only two (diabatically-coupled) states; however, all of the results in this section can be generalized to the general problem of many interacting system states. For any two-level system, we can suggestively write the Hamiltonian as

$$\hat{H} = \begin{pmatrix} \hat{h}_1 & 0 \\ 0 & \hat{h}_2 \end{pmatrix} + \lambda \begin{pmatrix} 0 & \hat{V} \\ \hat{V} & 0 \end{pmatrix} \equiv \hat{H}_0 + \hat{H}_1 \tag{3.2}$$

where $\hat{h}_1$ and $\hat{h}_2$ represent all diagonal elements of the Hamiltonian related to both system and bath, $\hat{V}$ represents all off-diagonal elements of the Hamiltonian related to both system and bath, and we have introduced an ordering parameter λ. The physical Hamiltonian is recovered for $\lambda = 1$.

To study the quantum dynamics generated by memory kernel resummations, we adopt the generalized master equation for the populations of a two-level system interacting with a general bath first derived by

Sparpaglione and Mukamel [218] using projection operator methods [223, 224, 225]

$$\begin{aligned} \dot{p}_1(t) &= -\int_0^t K_{11}(t-s)p_1(s)ds + \int_0^t K_{22}(t-s)p_2(s)ds \\ \dot{p}_2(t) &= \int_0^t K_{11}(t-s)p_1(s)ds - \int_0^t K_{22}(t-s)p_2(s)ds \end{aligned} \tag{3.3}$$

where $p_1(t)$ and $p_2(t)$ are the populations of the two states as functions of time, and K_{11} and K_{22} are the time-dependent memory kernels for the forward ($1 \to 2$) and backward ($2 \to 1$) transitions. We use this formalism primarily because it can be trivially generalized to include many states.

We will work explicitly with populations *differences*. It can be shown using the normalization condition $p_1(t) + p_2(t) = 1$ that equation 3.3 can be rewritten in terms of $P(t) \equiv p_1(t) - p_2(t)$ as

$$\dot{P}(t) = -\int_0^t K_+(t-s)P(s)ds - \int_0^t K_-(s)ds \tag{3.4}$$

where $K_\pm(t) \equiv K_{11}(t) \pm K_{22}(t)$. Note that equation 3.4 has the form of a generalized Langevin equation, with K_+ acting as a friction kernel and the integral of K_- acting as a random noise term.

Using this formalism allows us to expand the memory kernels perturbatively, using λ to collect terms of similar order:

$$K_{11/22}(t) = \lambda^2 K^{(2)}_{11/22}(t) + \lambda^4 K^{(4)}_{11/22}(t) + \cdots \tag{3.5}$$

where $K^{(2n)}_{11/22}(t)$ is the $2n$th-order contribution to the memory kernel. Note that in the special case where $\hat{V}$ is a constant, V, this is equivalent to expanding the memory kernels in a power series in V. For the remainder of this chapter and in order to simplify our discussion, we shall assume that $\hat{V}$ is a constant.

3.2.2 Derivation of $K^{(4)}$ for the Spin-Boson Model

In order to examine the dynamics generated by these memory kernels in detail, we restrict ourselves to specifically to the spin-boson Hamiltonian (see Section 1.1.3 for details). Because the spin-boson Hamiltonian comprises a two-level system linearly coupled to a bath of harmonic oscillators, it should come as no surprise that analytical expressions can be derived for $K^{(2)}(t)$, $K^{(4)}(t)$, and all $K^{(2n)}(t)$. We present here the main analytical result of this chapter: a novel, generalizable derivation of $K^{(4)}(t)$ that does not invoke Liouville space. For the spin-boson problem, the memory kernels can be written as

$$K^{(2)}_{11/22}(t) = 2\mathrm{Re}\left[f_2^{\pm}(t)\right] \tag{3.6}$$

$$
\begin{aligned}
K^{(4)}_{11/22}(t) &= \int_0^t ds_1 \int_0^{s_1} ds_2 K^{(2)}_{+}(t-s_1)K^{(2)}_{11/22}(s_2) - 2\int_0^t ds_1 \int_0^{t-s_1} ds_2 \mathrm{Re}\left[f_4^{\pm}(t-s_1-s_2,s_1,s_2)\right] \\
&\quad +2\int_0^t ds_1 \int_0^{-t} ds_2 \mathrm{Re}\left[f_4^{\pm}(-t-s_2,t-s_1,s_1)\right] \\
&\quad -2\int_0^t ds_1 \int_0^{t-s_1} ds_2 \mathrm{Re}\left[f_4^{\pm}(-t,t-s_1-s_2,s_1)\right] \qquad (3.7)
\end{aligned}
$$

where $K^{(2)}_{+}(t) = K^{(2)}_{11}(t) + K^{(2)}_{22}(t)$ and the top sign is for K_{11} / the bottom sign is for K_{22}. The ubiquitous functions $f_2^{\pm}$ and $f_4^{\pm}$ can be represented analytically as

$$
f_2^{\pm}(t) = V^2 \exp\left[-i\epsilon t - (Q'(t) \pm iQ''(t))\right] \qquad (3.8)
$$

$$
f_4^{\pm}(s_1,s_2,s_3) = \frac{f_2^{\pm}(s_1)f_2^{\pm}(s_2)f_2^{\pm}(s_3)f_2^{\pm}(s_1+s_2+s_3)}{f_2^{\pm}(s_1+s_2)f_2^{\pm}(s_2+s_3)} \qquad (3.9)
$$

where

$$
\begin{aligned}
Q'(t) &= \frac{4}{\pi}\int_0^{\infty} \frac{J(\omega)}{\omega^2}\left(1-\cos(\omega t)\right)\coth\left(\frac{\beta\omega}{2}\right) \qquad (3.10) \\
Q''(t) &= \frac{4}{\pi}\int_0^{\infty} \frac{J(\omega)}{\omega^2}\sin(\omega t) \qquad (3.11)
\end{aligned}
$$

A detailed derivation of equations 3.6 through 3.10 can be found in Appendices A.1 and A.2.

3.2.3 Resummation Schemes

It is well-known that series generated from perturbation theory are not always convergent, especially when truncated [226]. Resummation techniques are ubiquitous in many areas of physics, including quantum electrodynamics [227, 228], renormalization group theory [229, 230], and quantum chemistry [231]. Resummations have also been used in the context of system-bath models to compute rate constants [218, 219, 217], but to our knowledge have never been applied to time-dependent rate kernels in order to study dynamics.

We will focus our attention in particular to resummations of memory kernels for generalized master equations. Resumming at the level of the memory kernels is preferable to resumming at the level of the populations for many reasons, summarized concisely in References [232] and [233]. These resummations are historically performed in the frequency domain, defined through the Fourier transform

$$
K(\omega) = \int_{-\infty}^{\infty} e^{i\omega t} K(t) dt
$$

As such, we will be focusing in particular on ways to resum $K^{(2)}(\omega)$ and $K^{(4)}(\omega)$ into a $K(\omega)$ containing

all orders of the electronic coupling V.

For the particular problem at hand, two resummation schemes have been proposed [218], dubbed the "Padé resummation" and the "Landau-Zener resummation." The Padé resummation is a rational resummation based off of Padé approximants [234], which have been very successful in several areas of physics related to the present problem. Particularly relevant is the result of Cho and Silbey, who showed [219] that the in the subspace comprised of N perturbatively-expanded states, the Fourier transform of the memory kernel $K(\omega)$ can best be represented by an $[N/N-1]$-Padé approximant. The authors proved that this particular resummation choice obeys Schwinger's stationary variational principle for scattering processes [235]. The consequence of this result is that rates obtained from these memory kernels will obey detailed balance as best as possible, a desirable feature that suggests that Padé resummation is the optimal resummation choice for this problem.

For the case $N = 1$ (our present scenario), the Padé approximant, to fourth order, is

$$K_{Padé}(\omega) = \frac{V^2 \left[K^{(2)}(\omega)\right]^2}{K^{(2)}(\omega) - V^2 K^{(4)}(\omega)} \tag{3.12}$$

This form of resummation has been recently employed by Wu and Cao [217] to study kinetics (the $t \to \infty$ limit of equation 3.1). Using the $\omega \to 0$ limit of equation 3.12, the authors showed that the Padé resummation gives very good agreement with numerically-exact results for a model problem. The authors also pointed out that part of this agreement can be attributed to the fact that the Padé resummation recovers the Zusman result [236] in the limit of weak system-bath and weak electronic coupling.

The Padé resummation scheme has been previously investigated in the context of certain classes generalized master equations [237, 238], with the conclusion that a Padé-resummed memory kernel leads to dynamics that converge for all times. Later work by Shi *et al* [232] pointed out that the quality of the dynamics generated by a Padé-resummed memory kernel for arbitrary regimes of Hamiltonian parameter space is still unknown. The general applicability of the Padé resummation for dynamics is one of the central questions this work sets out to answer.

An alternative resummation scheme proposed [239] has been dubbed the Landau-Zener resummation due to its similarity in form to the famous Landau-Zener equation. To fourth order, the Landau-Zener resummation is given by

$$K_{LZ}(\omega) = -\frac{\left[K^{(2)}(\omega)\right]^2}{2K^{(4)}(\omega)} \left[1 - \exp\left(\frac{2V^2 K^{(4)}(\omega)}{K^{(2)}(\omega)}\right)\right] \tag{3.13}$$

It has been shown [218] that this resummation scheme agrees with the Padé scheme in the nonadiabatic limit, but differs from the Padé scheme by a factor of 2 in the adiabatic limit. This flaw prevents the Landau-Zener scheme from being applicable to study dynamics in the adiabatic regime. Fortunately, mixed quantum-classical and semiclassical schemes have great success when the dynamics evolve strictly

on one adiabat, so we shall focus our attention on the nonadiabatic regime.

3.2.3.1 Time-domain Padé Resummation

A very recent detailed analysis of Padé resummations for this problem [240] has made explicit certain conditions on the second-order and fourth-order kernels that predict whether or not Padé resummation will blow up or not; using these conditions, Reichman et al have shown that Padé resummation is expected to behave poorly at low temperatures and high system-bath coupling.

Based on this discussion, we observe that it is possible for the Padé resummation to fail because the Padé resummation is a rational resummation, and certain sets of bath parameters can cause singularities in the resummed kernel in Fourier (or Laplace) space, leading to long-time divergences. A Padé resummed kernel can be written in Laplace space as

$$K_{Padé}(s) = \frac{\left[K^{(2)}(s)\right]^2}{K^{(2)}(s) - K^{(4)}(s)} \tag{3.14}$$

Besides the methods that have been investigated previously, there is one additional method that can be used to potentially smooth the divergences inherent to a rational approximation: Get rid of the denominator. We do so by first rearranging equation 3.14:

$$K_{Padé}(s) = K^{(2)}(s) + \phi(s)K_{Padé}(s) \tag{3.15}$$

where we have defined

$$\phi(s) \equiv \frac{K^{(4)}(s)}{K^{(2)}(s)} \tag{3.16}$$

We then analytically inverse Laplace transform equations 3.15 and 3.16, recognizing that a multiplication in the Laplace domain is a convolution in the time domain:

$$K^{(4)}(t) = \int_0^t dt^{'} \phi(t - t^{'}) K^{(2)}(t^{'}) \tag{3.17}$$

$$K_{Padé}(t) = K^{(2)}(t) + \int_0^t dt^{'} \phi(t - t^{'}) K_{Padé}(t^{'}) \tag{3.18}$$

We can thus carry out Padé resummation in the time domain by solving equation 3.17 numerically for $\phi(t)$, and then using that solution to solve equation 3.18 numerically for $K_{Padé}(t)$. Throughout this chapter, we will refer to the kernel obtained via Equation 3.18 as the time-domain Padé or TDP kernel.

3.2.4 Populations at Equilibrium

For the case of a system with electronic bias, resummation is rather arbitrary: Do we resum the forward rate kernel K_{11} and the backward rate kernel K_{22} and then add and subtract them to form $K_{\pm}$? Or do we resum $K_{\pm}$ directly? Stating this another way, we can define a resummation function that takes a second-order kernel and a fourth-order kernel and returns a resummed kernel (through, for instance, a Padé resummation):

$$K = R\left[K^{(2)}, K^{(4)}\right] \tag{3.19}$$

we can then imagine that we can form $K_{\pm}$through a number of different schemes; for instance,

$$K_{\pm} = R\left[K_{11}^{(2)}, K_{11}^{(4)}\right] \pm R\left[K_{22}^{(2)}, K_{22}^{(4)}\right] \tag{3.20}$$

or

$$K_{\pm} = R\left[K_{11}^{(2)} \pm K_{22}^{(2)}, K_{11}^{(4)} \pm K_{11}^{(4)}\right] \tag{3.21}$$

Both of these schemes give the exact perturbation series to fourth order, but differ at higher orders. Selecting one over the other is an arbitrary choice.

We can reduce this arbitrariness by introducing a parameter α that interpolates smoothly between these two limits:

$$\begin{aligned} K_{\pm} &= R\left[(1-\alpha)K_{11}^{(2)} \pm \alpha K_{22}^{(2)}, (1-\alpha)K_{11}^{(4)} \pm \alpha K_{22}^{(4)}\right] \\ &\quad + R\left[\alpha K_{11}^{(2)} \pm (1-\alpha)K_{22}^{(2)}, \alpha K_{11}^{(4)} \pm (1-\alpha)K_{22}^{(4)}\right] \end{aligned} \tag{3.22}$$

As long as the resummation is first-order homogeneous (as is the case for both the Padé scheme and the Landau-Zener scheme), we can recover equation 3.20 if $\alpha = 0$ and equation 3.21 if $\alpha = \frac{1}{2}$.

Adding in this additional degree of freedom allows us to ensure that the dynamics created by the resummed memory kernel will obey detailed balance. It is well-known that using master equations with second-order kernels does not guarantee that the dynamics settle on the correct equilibrium populations in the case of a system with electronic bias [68, 70]. Introducing α allows us to choose from an infinitely large number of arbitrary choices the optimal manner of resummation that gets equilibrium populations correct. Namely, if the equilibrium populations are known (e.g., from a path integral Monte Carlo

simulation [241, 242]), we can tune α by enforcing the detailed balance condition

$$\frac{k_{11}(\alpha)}{k_{22}(\alpha)} = \frac{p_2^{eq}}{p_1^{eq}} \tag{3.23}$$

by tuning α over the interval $\left[0, \frac{1}{2}\right]$, where $k_{11} \equiv K_{11}(\omega = 0)$ and $k_{22} \equiv K_{22}(\omega = 0)$ are the forward and backward rate constants, and p_1^{eq} and p_2^{eq} are the equilibrium populations.

We note in passing, though importantly, that we cannot use Equation 3.22 for the case of time-domain Padé resummation. The TDP resummation scheme (Equations 3.17 and 3.18) rely on solving an auxilliary Volterra Equation of the First Kind for $\phi(t)$, and then using this function to solving a Volterra Equation of the Second Kind for $K(t)$. Unfortunately, Volterra Equations of the First Kind do not have unique solutions when the Volterra kernel (in the case of Equation 3.17, $K^{(2)}(t)$) is 0 at $t = 0$. This is not a problem normally; however, $K_-^{(2)}(0) = 0$ rigorously, meaning using time-domain Padé resummation cannot be done to form a resummed $K_-(t)$ and thus optimizing the kernel for equilibrium populations cannot be done in general. The end result is that often, time-domain Padé is not the preferred resummation of choice in cases with bias.

3.3 Results and Discussion

3.3.1 Implementation Details

For each set of spin-boson parameters studied, $K_{11}^{(2)}$ and $K_{11}^{(4)}$ (and, in cases where an electronic bias is present, $K_{22}^{(2)}$ and $K_{22}^{(4)}$) were calculated using a FORTRAN95 implementation of equations 3.6 and 3.7. All integrals were computed using an adaptive Gauss-Legendre quadrature until an integral tolerance of 10^{-6} was reached. The frequency integrals over the spectral density were computed with a hard upper frequency cutoff of $\omega = 30$, which was found to be enough to give stable and convergent results for the short propagation time ranges studied.

Once the kernels were computed, they were resummed according to equation 3.12 (Padé resummation) and equation 3.13 (Landau-Zener resummation). Then, a standard algorithm for solving Volterra integrodifferential equations of the second kind [243] was used to solve equation 3.4 for $P(t) \equiv p_1(t) - p_2(t)$, the difference in population between states 1 and 2 as a function of time. Propagating population dynamics using only $K_{11}^{(2)}$ and $K_{22}^{(2)}$, i.e. applying the non-interacting blip approximation or NIBA, is also considered for comparison.

In order to benchmark our fourth-order resummations, we use an Ohmic spectral density with a Drude-Lorentz cutoff, often referred to as a Debye spectral density

$$J(\omega) = \frac{\eta\omega\omega_c}{\omega_c^2 + \omega^2} \tag{3.24}$$

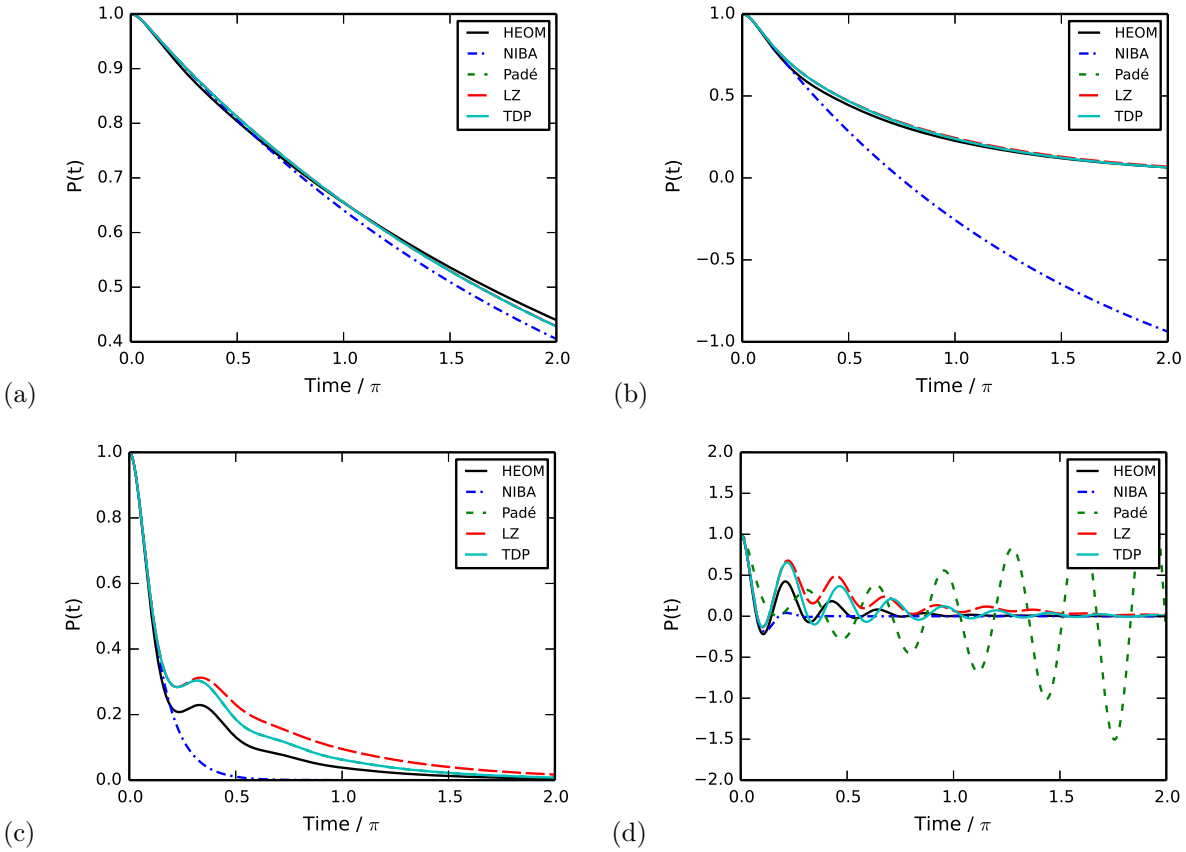

Figure 3-1: Population dynamics of the spin-boson Hamiltonian for various strengths of the electronic coupling. The HEOM (exact) result and the NIBA result are plotted to compare with the two different fourth-order resummations presented in this work: the Padé resummation (equation 3.12) and the Landau-Zener resummation (equation 3.13). Values of the Hamiltonian parameters are $\omega_c = 1.0$, $\eta = 2.0$, $\beta = 0.125$, and (a) $V = 0.5$, (b) $V = 1.0$, (c) $V = 2.0$, and (d) $V = 4.0$. Where no green curve for Padé resummation is shown, it is superimposed on top of the teal TDP curve.

where η and ω_c are parameters that control the strength of the system-bath coupling the the upper cutoff frequency of the bath, respectively. A benefit of using this spectral density is that numerical results for this problem have been presented in the past [68, 70] using various approximate methods.

Additionally, a hierarchical equation of motion (HEOM) technique has recently been presented [71, 72] that obtains (in principle) numerically-exact results for the spin-boson problem. The HEOM technique is a path-integral-based technique which replaces the Vernon-Feynman influence functional with a set of time-nonlocal auxilliary density matrices which account for non-Markovian system-bath coherences. These density matrices are related to one another via hierarchical equations; truncating this hierarchy at order M is equivalent to order $2M$ in perturbation theory in the system-bath coupling [244]. As such, the hierarchy is often very quickly convergent, provided the system-bath coupling is not strong. If changing the depth of the hierarchy does not change the resulting population dynamics, the approximation is

equivalent to infinite-order perturbation theory and is thus exact.

While the HEOM has the potential to give numerically-exact results, it has some shortcomings. The most glaring is that it can only be used for spectral densities of the form given in equation 3.24. Additionally, the HEOM requires evaluation of many depths of a hierarchy of increasing computational complexity; a deeper hierarchy is needed for strong system-bath coupling or low temperature. However, despite the breakdown of the standard HEOM technique in the strong system-bath coupling regime and the low-temperature regime (the latter problem which can been solved using a stochastic HEOM [204]), for many parameter regimes of the Debye spectral density, the HEOM gives extremely accurate results. In this chapter, we consider results from a sufficiently deep HEOM truncation (a hierarchy depth of 11 with a maximum Matsubara frequency of 6) to be numerically exact for this problem. For all calculations, the cutoff frequency ω_c was normalized to 1, and other parameters adjusted with relation to ω_c.

3.3.2 Stability with Increasing Electronic Coupling

As noted previously, NIBA fails with increasing electronic coupling. The reason is quite obvious: we are doing a perturbative expansion in the electronic coupling, so a second-order truncation won't capture any quantum events that involve more than two hops between energy surfaces [70]. Figure 3-1 shows clearly that this is indeed the case. For the case of small electronic coupling (panel (a)), NIBA is good enough to reproduce the HEOM result, and, as higher-order terms in the perturbation series are small, any fourth-order resummation does not significantly change this result.

Going to higher and higher values of the electronic coupling (panels (b) through (d)), NIBA breaks down: two-hop events are no longer sufficient to accurately describe the short-time quantum dynamics of the spin-boson model. Specifically, oscillations in population die out much too fast. Comparing the two fourth-order resummation schemes presented in this chapter with the HEOM result, however, shows that there is hope: higher-order terms recover these oscillations with nearly the correct frequency and a relatively correct damping rate.

In the case of very strong electronic coupling, it is interesting to note that recovering qualitatively correct dynamics depends on the nature of the fourth-order resummation. In particular, using a Padé approximant to resum the second- and fourth-order memory kernels gives a memory kernel which leads to populations that oscillate wildly in time and at the incorrect frequency; by contrast, the Landau-Zener-resummed kernel produces populations which are well-behaved for all times. The time-domain Padé resummed kernel also gives populations which are well-behaved for all times, and are quantitatively different from the Landau-Zener populations.

This is a notable result, as the Padé approximant is the resummation method of choice for rate constants, the zero-frequency limit of the frequency-dependent memory kernel [219, 217]. It can easily be shown that in the small electronic, slow bath limit, the Padé-resummed rate is exactly the rate derived

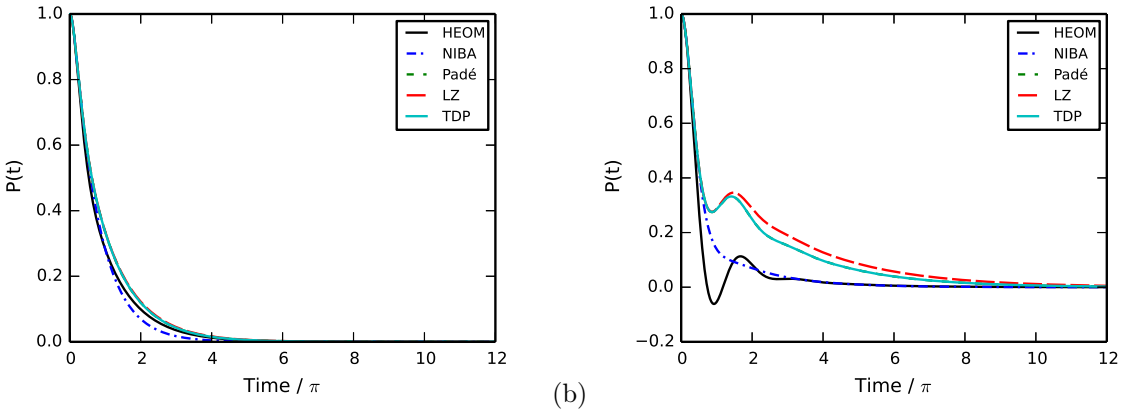

Figure 3-2: Population dynamics of the spin-boson Hamiltonian for various temperatures at moderate electronic coupling. Values of the Hamiltonian parameters are $\omega_c = 1.0$, $\eta = 1.0$, $V = 0.5$ and (a) $\beta = 0.5$ (high temperature); or (b) $\beta = 10.0$ (low temperature). Where no green curve for Padé resummation is shown, it is superimposed on top of the teal TDP curve.

by Zusman connecting the nonadiabatic regime to the adiabatic regime [236, 219].

For short-time dynamics in the large electronic coupling limit, however, the dynamics generated by a Padé resummation are qualitatively incorrect. The reason why this approximate resummation is good for rate constants but bad for dynamics can be seen by examining equation 3.12: When $K^{(2)}(\omega) \approx V^2 K^{(4)}(\omega)$, the Padé-resummed kernel diverges. It is very unlikely that this equality will occur at $\omega = 0$; however, as V grows, the chance that this divergence will occur for some larger value of ω also grows. This introduces a spurious high-frequency component to the memory kernel in the time domain, which translates into populations that oscillate indefinitely, rather than settling down to equilibrium at the desired rate. These divergences are smoothed over by instead performing the resummation in Laplace space, or, since the inverse Laplace transform is not numerically well-conditioned, in the time domain.

3.3.3 Temperature Dependence

The low-temperature regime has often proved problematic for quantum dynamics studies, as many systems are "very quantum" at extremely low temperatures. This problem was studied (and to some extent solved for Ohmic baths) in detail by Reichman [221], but the general case remains an open problem in quantum dynamics. Even the HEOM approach to solving the spin-boson problem breaks down as the temperature approaches 0: while still in principle exact, computation of the exact answer requires inclusion of many Matsubara frequencies and a very deep hierarchy, which very quickly becomes computationally intractable. Other formulations of the HEOM have been designed to fix this problem [204], but a solution still does not exist for general spectral densities.

While our approach is robust in the strong electronic coupling regime, the same cannot be said for the low-temperature regime. Short-time dynamics of the spin-boson Hamiltonian to fourth order in V are

shown in figure 3-2 for moderate values of the system-bath coupling and the electronic coupling. As can be seen in the figure, for high temperature (small values of $\beta \equiv 1/k_B T$), even NIBA gets qualitatively correct dynamics. This makes sense, as the Marcus rate for electron transfer can be formulated as the high-temperature, slow-bath, long-time limit of NIBA [51, 218], and the Marcus rate is a quite good description of the kinetics of many experimental systems [245]. A Padé-based resummation is required to recover correct *quantitative* dynamics in this regime, as only Padé resummations are known to recover the Zusman limit.

At low temperatures, both NIBA and any fourth-order resummations give qualitatively incorrect description of the dynamics: NIBA dephases too quickly, and the fourth-order resummations do not decay to equilibrium quickly enough. Both the lack of low-frequency oscillations and the incorrect zero-frequency component of the population dynamics can be traced to the presence of a large number of low-frequency bath modes at low temperatures, which have a large contribution to the memory kernels. The fourth-order resummations studied in this thesis assume a "small" $V^4 K^{(4)}$, which may not necessarily be the case at low temperatures; this observation may lend to the development of alternative resummation schemes for fourth-order perturbation series and beyond.

We note in passing that for regimes where NIBA does not give good dynamics, adding in fourth-order effects tends to *overcorrect.* This result has been observed for rates [217], and is seen very clearly in figure 3-2 to also be the case for dynamics.

3.3.4 Systems with Electronic Bias

A systematic problem with NIBA arises in systems with an electronic bias: NIBA memory kernels generate population dynamics that do not decay to the correct equilibrium, meaning these memory kernels disobey detailed balance. Disobedience of detailed balance implies a fictitious breaking of time-reversal symmetry, which may cause systemic problems with short-time dynamics. This issue should be addressed, at least to some extent, by including higher-order contributions to the memory kernel; indeed, it has previously been shown that fourth-order corrections to Redfield theory obey detailed balance exactly [222]. We now turn our attention to the dynamics of a system with an electronic bias, particularly to the question of how including fourth-order effects in the memory kernels affects the obedience of detailed balance.

Figure 3-3 shows our main result for the biased case: going to fourth order helps, but does not guarantee, the satisfaction of the detailed balance condition (and, in some cases, conservation of probability!). As expected, for small values of the electronic coupling (when effects fourth-order in the coupling are small), the equilibrium populations are more-or-less exactly correct; for larger values, the equilibrium populations deviate more from their correct values. For reasons discussed in cases without bias, using a Padé resummation can exacerbate this problem; additionally, time-domain Padé is not as easy fixed as $K_-(t = 0) = 0$, making Equation 3.17 numerically ill-conditioned. Nevertheless, a combination of

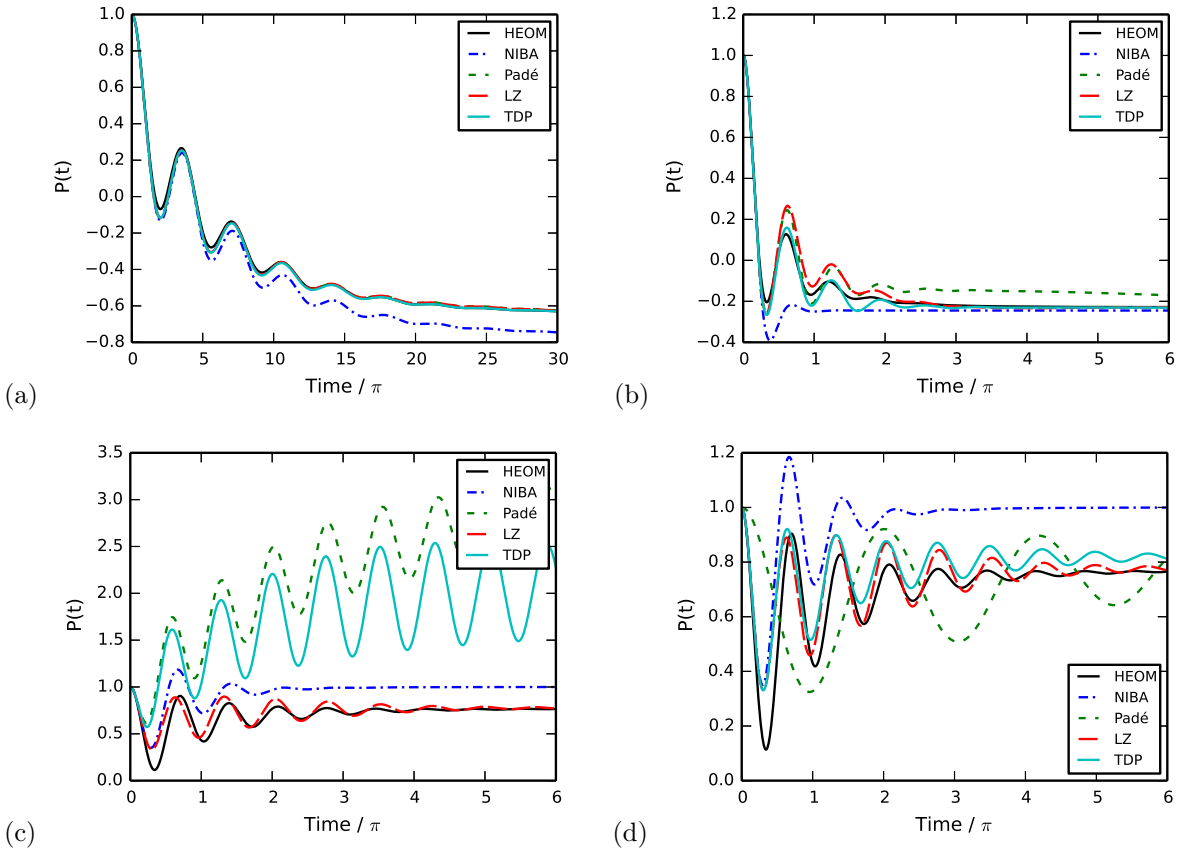

Figure 3-3: Population dynamics of the spin-boson Hamiltonian for various strengths of the electronic bias. All resummations were conducted using equation 3.22 for the reasons discussed in section 3.2.4; where possible, the value of the parameter α was fixed by enforcing detailed balance, equation 3.23. The "time-domain Padé resummation" plots were generated using the TDP resummation for K_{11}, K_{22}, and K_+, but the frequency-domain Padé resummation for K_- to avoid the ill-conditioning problem (Equation 3.17 has no unique solution for $K_-(t)$). Values of the Hamiltonian parameters are (a) $\omega_c = 1.0$, $\eta = 0.1$, $\beta = 5.0$, $V = 0.2$, and $\epsilon = 0.4$ ($\alpha = 0.19$ for Padé and Landau-Zener resummations; note the different scale on the time axis); (b) $\omega_c = 1.0$, $\eta = 0.665$, $\beta = 0.376$, $V = 1.33$, and $\epsilon = 1.33$ ($\alpha = 0.37$ for Padé and Landau-Zener resummations); and (c) $\omega_c = 1.0$, $\eta = 0.5$, $\beta = 5.0$, $V = 1.0$, and $\epsilon = -2.0$ ($\alpha = 0.16$ for Padé, $\alpha = 0.5$ for Landau-Zener). Panel (d) uses the same parameters as Panel (c) but sets $\alpha = 0.5$ for all resummations.

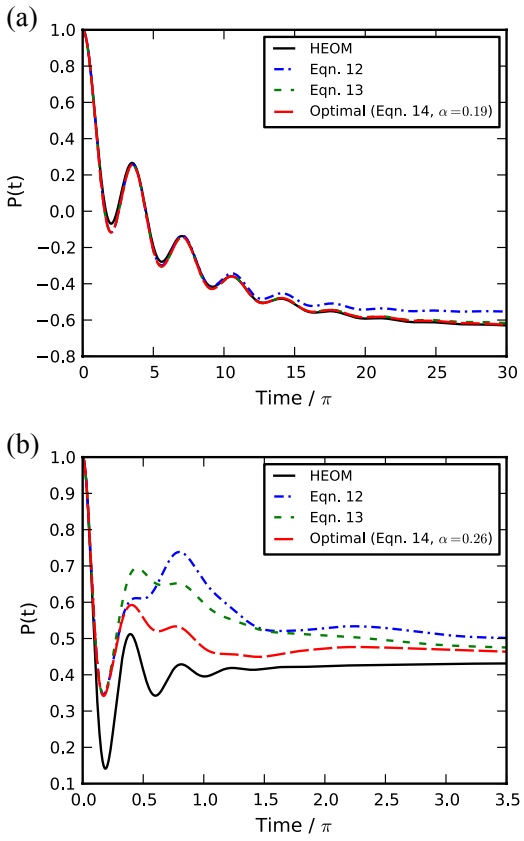

Figure 3-4: As stated in the text, there is an arbitrary choice of which memory kernels to resum: the forward and backwards rate kernels K_{11} and K_{22}, or some linear combination of these kernels. Plotted here are three specific choices of which memory kernels to resum in a Landau-Zener fashion (i.e. according to equation 3.13): resummation according to equation 3.20, equation 3.21, and equation 3.22. (a) For most choices of Hamiltonian parameters, it is possible to satisfy the detailed balance condition exactly using an intermediate value of α. For the set of Hamiltonian parameters in figure 3-3(a) ($\omega_c = 1.0$, $\eta = 0.1$, $\beta = 5.0$, $V = 0.2$, and $\epsilon = 0.4$), using $\alpha = 0.19$ causes detailed balance to be satisfied. (b) For other sets of Hamiltonian parameters, it is only possible to satisfy detailed balance in a least-squares sense. For example, with $\omega_c = 1.0$, $\eta = 1.0$, $\beta = 0.25$, $V = 2.0$, and $\epsilon = -4.0$, using $\alpha = 0.26$ will give dynamics with the "best" long-time asymptotics allowed. Note that the time axes on the two panels have different ranges.

frequency-domain and time-domain Padé resummations for the four different kernels involved (K_{11}, K_{22}, K_+ and K_-) will often produce the best possible dynamics of any resummation scheme studied.

We note that the divergence seen in Figure 3-3(c) is decidedly *not* due to the divergence of the Padé denominator, but another effect entirely. We suspect that it may be due to poor numerical convergence of the underlying kernels ($K_{11}^{(2)}$, $K_{22}^{(2)}$, $K_{11}^{(4)}$, and $K_{22}^{(4)}$) at intermediate times, giving unphysical resummed kernels. We note that if we set $\alpha = 0.5$ for the two Padé resummations, the dynamics improve considerably, as shown in Figure 3-3(d); however, our algorithm for optimizing α based on the detailed-balance condition does not currently pick out this solution, suggesting that it is not the optimal algorithm for choosing the best resummed kernel.

Including memory effects up to infinite order in V is one way to guarantee the obedience of detailed balance. Since this is not computationally feasible, we present an alternative approach that guarantees that any kernel resummed to fourth order (or higher) will generate dynamics that decay to the correct equilibrium populations.

Following the discussion in section 3.2.4, we have tried resummations of the form of equation 3.22, enforcing the detailed balance relation in equation 3.23 to optimize a parameter α. This scheme exploits a choice we have when deciding how to perform a resummation in order to guarantee the correct equilibrium. We will note that in general, it is also possible to know *a priori* the correct equilibrium populations, either by knowing the long-time limit of a numerically exact solution (as is the case in this present work), or, more generally, by doing path integral Monte Carlo or molecular dynamics simulations in order to explore the energy landscape of the two states as they interact with a bath [241, 242].

Figure 3-4 shows the dynamics generated by a Hamiltonian in the moderate electronic coupling, moderate system-bath coupling, moderate temperature regime with strong electronic bias. In each panel, four dynamics runs are plotted: the HEOM run, and runs generated by resumming the memory kernels in a Landau-Zener fashion according to equations 3.20, 3.21, and 3.22. For most sets of Hamiltonian parameters, like those in figure 3-4(a), the detailed balance condition can be met exactly with some $0 \leq \alpha \leq \frac{1}{2}$. For some sets of Hamiltonian parameters, like those in figure 3-4(b), the detailed balance condition can only be satisfied in a least-squares sense.

As can be seen in the figure, the different choices for how to resum the forward and backward memory kernels can give very different trajectories. The different trajectories are entirely artifactual: were we to know all of the $K^{(2n)}$ out to infinite order, we wouldn't need to perform an approximate resummation and the discrepancy in how we choose to resum kernels disappears. Nevertheless, if we wish to compute memory kernels to finite order, we must make an arbitrary choice. Figure 3-4 shows that the best value for this choice is the particular interpolation between equations 3.20 and 3.21 that satisfies equation 3.23 (either exactly or in a least-square manner)—i.e., the particular resummation where the long-time limit of the resummed kernels best obeys detailed balance.

It is worth noting that for some parameter regimes, one of the two resummations in equations 3.20 and 3.21 diverges. A set of parameters where this occurs is the set of parameters used in figure 3-3(c): the kernel resummed according to equation 3.20 diverges but the kernel resummed according to equation 3.21 does not. Using equation 3.22 to resum and optimizing α gives a value $\alpha = 0.5$. For this value of α, equation 3.22 reduces exactly to equation 3.21. Thus, using equation 3.22 and optimizing α to enforce detailed balance not only gives qualitatively better dynamics for some parameter regimes, but prevents divergences in other parameter regimes. Doing the resummation in this manner is not just a bonus; it is imperative.

3.4 Conclusions

In this chapter, we have shown for the first time numerical results for a generalized system-bath master equation that uses rate kernels resummed from a fourth-order perturbation series in the electronic coupling. We have shown that for the case of a two-level system interacting with a harmonic bath that a Fourier-resummed Padé resummation diverges for even moderate values of the electronic coupling; however, most of these divergences are smoothed over when carrying out this resummation in the time domain. The Landau-Zener resummation scheme never diverges; however, it has the incorrect asymptotics. Therefore, Padé resummation is recommended for regions of parameter space where the resulting dynamical kernel does not diverge (as discussed in great detail in Reference [240]).

The current resummation techniques robustly describe the dynamics for a wide range of Hamiltonian parameters, including cases with an electronic bias—cases which have historically troubled system-bath methods. The low-temperature regime, a regime which has plagued system-bath models for decades, remains problematic. We have lastly shown that by using a fourth-order resummation, one can always guarantee that the dynamics reach the correct equilibrium by exploiting a freedom inherent in the structure of the problem.

One of our goals when beginning this work was to develop a general, systematically improvable scheme to study system-bath dynamics. We have noted that the scheme that we have presented gets close to the exact answer for a model spectral density in most parameter regimes, but does not recover the exact result for regimes of very strong electronic coupling or low temperature.

To address the former issue, we need to include higher orders in the perturbation series. The simplest approach is to generalize our derivation in section 3.2.2 to arrive at an expression for $K^{(6)}$; unfortunately, the computational scaling becomes limiting when going out to such high orders of perturbation theory. Perhaps a more promising approach is to enforce both good short-time behavior *and* good strong-coupling behavior. The Landau-Zener resummation scheme succeeds at the former, but disagrees with the adiabatic ($V \to \infty$) limit by a factor of two [218]. Correct behavior in the adiabatic limit can be built into a more

sophisticated resummation scheme. To improve even more on behavior in the strong-coupling (but not adiabatic) regime, we can derive expressions for the lowest-order non-adiabatic correction to adiabatic behavior and incorporate it into our resummed memory kernels.

To address the latter issue, new resummation schemes are required that correctly capture the low-temperature limit. Other resummation schemes, such as a generalized high-order resummation [218], the noncrossing cumulant scheme [65], and convolution resummation with auxillary kernels [232, 246] have the potential to capture this limit. Exploration into the numerical results of kernels generated by these resummation schemes to fourth order is ongoing.

Finally, and perhaps most excitingly, we have limited the discussion in this chapter to one particular form of the spectral density $J(\omega)$—namely, the Debye spectral density. Our method makes no assumptions as to the form of the spectral density; as such, we should be able to investigate system-bath dynamics using arbitrary spectral densities. Many procedures have been suggested in the literature for sampling numerical spectral densities from classical molecular dynamics trajectories and applying a post-hoc quantum-mechanical correction to the classical trajectories to extract a semiclassical spectral density [245, 66, 247, 248, 249]. In the next chapter, we investigate the dynamics for the case of a general spectral density, with the hope that approximate dynamics for a large number of chemically-relevant problems may become accessible in the near future.

Chapter 4

Condensed Phase Electron Transfer Beyond the Condon Approximation

4.1 Introduction

Electron transfer is a fundamental process in chemistry and biology. An exact dynamical description of this process from first principles is difficult if not impossible due to the multitude of degrees of freedom involved in solvent reorganization. These solvent degrees of freedom are critical for properly describing electron transfer rates and dynamics, as observed originally by Marcus [48, 49, 50] and subsequently reinforced by many others [53, 54, 55, 56, 57, 58, 59, 60, 61]. Because exact quantum methods cannot describe systems with thousands of degrees of freedom without running into exponential scaling, approximate models are often invoked to describe electron transfer dynamics.

As described in Section 1.1.3, one important model for describing condensed-phase electron transfer is the spin-boson model, a system-bath model that describes a two-level system coupled linearly to a large number of harmonic bath modes [62]. While simpler than an atomistic model, the spin-boson model still cannot be solved exactly: the exact density matrix and the propagator must each be expanded in the basis of a many-dimensional collection of harmonic oscillators, again leading to exponential scaling. Nevertheless, many approximate methods [63, 65, 66, 67, 68, 69, 70] (and exact methods for certain assumptions about the bath [71, 72]) for solving the Schrödinger equation for this Hamiltonian exist. We have outlined and explored some of these methods in the previous chapter.

The spin-boson model is useful; however, it is not without its limitations. One limitation is that the spin-boson model makes the Condon approximation—which states that electronic transitions occur instantaneously on the timescale of nuclear motion, or alternatively that the electronic coupling operator $\hat{V}$ is a constant that does not depend on nuclear coordinates [51]. This approximation is often successful,

but in certain cases—specifically, photochemistry—it is demonstrably bad.

In this chapter, we examine approximate solutions to the linear vibronic coupling Hamiltonian, which is an extension of the spin-boson Hamiltonian that includes these non-Condon effects. Using a generalized master equation formalism [218], we derive memory kernels for the linear vibronic coupling Hamiltonian to fourth order in perturbation theory in the electronic coupling, amounting to augmenting the well-studied second- and fourth-order kernels [68, 70, 250] with several extra non-Condon terms. In order to demonstrate the impact of these non-Condon terms, we examine the dynamics of the electron transfer self-exchange reaction Fe(II) + Fe(III)→Fe(III) + Fe(II) in water. We choose these system because (1) the partitioning between system and bath is straightforward; (2) the system is very well-studied [251, 252, 253, 245, 254, 255, 256, 257, 258, 259], and (3) there is no intrinsic bias driving the reaction one way or the other, meaning we are not in a regime where second-order methods are known to give qualitatively incorrect answers [68, 70].

4.2 Theory

4.2.1 Spin-Boson Hamiltonian

A detailed description of the spin-boson model can be found in Section 1.1.3; here, we briefly recap what was said there. Mathematically, the spin-boson model can be described with the Hamiltonian

$$\begin{aligned}
\hat{H}_{SBM} &= \hat{H}_s + \hat{H}_b + \hat{H}_{s-b} \\
&= \begin{pmatrix} -\frac{\epsilon}{2} & V_0 \\ V_0 & \frac{\epsilon}{2} \end{pmatrix} + \sum_j \begin{pmatrix} \frac{\hat{p}_j^2}{2} + \frac{1}{2}\omega_j^2 \hat{x}_j^2 & 0 \\ 0 & \frac{\hat{p}_j^2}{2} + \frac{1}{2}\omega_j^2 \hat{x}_j^2 \end{pmatrix} \\
&\quad + \sum_j \begin{pmatrix} c_j \hat{x}_j & 0 \\ 0 & -c_j \hat{x}_j \end{pmatrix}
\end{aligned} \tag{4.1}$$

where $\hat{H}_s$ is the Hamiltonian describing the two-level system, $\hat{H}_b$ the harmonic bath, and $\hat{H}_{s-b}$ the system-bath coupling. The two system states intrinsically differ in energy by a bias of ϵ and are coupled with a constant coupling V_0. The bath is comprised of a collection of harmonic oscillators with frequency ω_j that couple to the system with coupling c_j. The mass-scaled normal mode coordinates and momenta of the bath are represented by $\hat{x}_j$ and $\hat{p}_j$, respectively.

4.2.2 Linear Vibronic Coupling Hamiltonian

The most straightforward way to generalize the spin-boson Hamiltonian to include non-Condon effects is to add to the Hamiltonian an off-diagonal coupling to the bath. This new Hamiltonian is known as the

linear vibronic coupling Hamiltonian, and has been studied in some detail [260, 261, 262, 263, 17, 264]. We described this model previously in Section 1.1.4; to recap, we can write the linear vibronic coupling Hamiltonian as

$$\hat{H}_{LVC} = \hat{H}_{SBM} + \sum_j \begin{pmatrix} 0 & V_j \hat{x}_j \\ V_j \hat{x}_j & 0 \end{pmatrix} \tag{4.2}$$

where $\hat{H}_{SBM}$ is the Hamiltonian defined in equation 4.1. This Hamiltonian has the advantage over $\hat{H}_{SBM}$ in that for some set of bath coordinates$\{\hat{x}_j\}$, it is possible for $\hat{H}_{LVC}$ to become proportional to the identity, allowing for the existence of conical intersections.

The linear vibronic coupling model can be understood by considering a two-level system interaction with a collection of harmonic oscillators. The two states have an energy difference, ϵ, and a coupling, V—each which fluctuate in time. The fluctuations in ϵ and V are driven by the action of the harmonic bath: some bath modes couple to the energy gap $\epsilon(t)$, driving its fluctuations; other bath modes couple to the coupling, $V(t)$, driving its fluctuations. In general, some bath modes could drive fluctuations in both ϵ and V, introducing cross-terms into the dynamics correlating the energy gap and coupling trajectories; as discussed in more detail in the next section, we will be neglecting cross-correlations.

4.2.3 Mode Continuua in Condensed Phases

In the gas phase, the number of bath modes defining $\hat{H}_{SBM}$ or $\hat{H}_{LVC}$ is numerable: a nonlinear molecule with N atoms has $3N-6$ vibrational models. In the condensed phase, where thousands of atoms must often be considered to get even a rudimentary desciption of charge-transfer dynamics, the number of bath modes quickly becomes innumerable. This quickly facilitates the introduction of the *spectral density*, which coarse-grains an uncountably large number of bath modes in the condensed phase into a continuous function describing how strongly the bath couples to the diagonal elements of the system Hamiltonian at various frequencies ω[51]

$$J_{EG}(\omega) \equiv \frac{\pi}{2} \sum_j \frac{c_j^2}{\omega_j} \delta(\omega - \omega_j) \tag{4.3}$$

In the case of the linear vibronic coupling model, the bath also couples to the off-diagonal elements of the system Hamiltonian. We thus must introduce two more spectral densities: one describing the explicit coupling of the bath to off-diagonal elements of the Hamiltonian,

$$J_V(\omega) \equiv \frac{\pi}{2} \sum_j \frac{V_j^2}{\omega_j} \delta(\omega - \omega_j) \tag{4.4}$$

and one describing the cross-correlation between time-domain energy gap fluctuations and coupling fluctuations,

$$J_{cross}(\omega) \equiv \frac{\pi}{2}\sum_j \frac{c_j V_j}{\omega_j}\delta(\omega-\omega_j) \tag{4.5}$$

where ω_j, c_j, and V_j are Hamiltonian parameters introduced in equations 4.1 and 4.2. The details of how these spectral densities may be obtained from molecular simulation will be discussed in the following section.

For the bulk of the discussion below, we make the approximation

$$J_{cross}(\omega) \approx 0$$

i.e., there is no coupling between bath modes which drive fluctuations in the energy gap and those which drive fluctuations in the coupling. While such a cross-coupling may exist in principle, in the vast majority of physical situations, very different bath motions are required to drive charge transfer in molecular systems like transition metal complexes and organic semiconductors. Thus, we shall neglect cross-coupling to distill the discussion down to the core bath effects responsible for driving charge transfer.

4.2.4 Generalized Master Equations and Memory Kernels

In order to study the dynamics generated by the linear vibronic coupling Hamiltonian, we have adopted a generalized master equation formalism [223, 224, 225], following the approach of Sparpaglione and Mukamel[218]. Generalized master equations are convenient ways of expressing the population dynamics of a system coupled to a bath when one is not interested in the detailed dynamics of the bath. We now assume a set of generalized master equations of the form

$$\begin{aligned}
\dot{p}_1 &= -\int_0^t K_1(t,t_1)p_1(t_1)dt_1 + \int_0^t K_2(t,t_1)p_2(t_1)dt_1 \\
\dot{p}_2 &= \int_0^t K_{11}(t,t_1)p_1(t_1)dt_1 - \int_0^t K_2(t,t_1)p_2(t_1)dt_1
\end{aligned} \tag{4.6}$$

which are identical to the equations in the Sparpaglione-Mukamel formalism [218], except that the kernels are no longer time-translationally invariant due to the use of the photochemical initial condition. Here, $p_1(t)$ and $p_2(t)$ are the populations of state 1 and state 2 respectively, and $K_1(t)$ and $K_2(t)$ are memory kernels describing the $1 \rightarrow 2$ and $2 \rightarrow 1$ population transfer process, respectively. Populations of a two-state system can be determined by solving these master equations for a given set of memory kernels.

While determining $K(t)$ is tantamount to solving the time-dependent Schrödinger equation and is

thus exponentially hard, one can expand $K(t)$ in a formal power series in the electronic coupling operator $\hat{V}$,

$$K(t) = \hat{V}^2 K^{(2)}(t) + \hat{V}^4 K^{(4)}(t) + ... \tag{4.7}$$

and use time-dependent perturbation theory in order to derive analytic expressions for $K^{(2)}$, $K^{(4)}$, and in principle all higher order terms. The exact kernel can then be reconstructed via a resummation technique, e.g. a Padé resummation [219, 250, 265, 240]. Note that truncating this perturbation series to second order for the spin-boson model results in the famous non-interacting blip approximation (NIBA) [64, 63], which is the Fermi's Golden Rule result for this problem—in many senses, it is a dynamical generalization of Marcus theory.

Using time-dependent perturbation theory and the master equations defined in equation 4.6, we have derived the non-Condon version of the memory kernel $K^{(2)}(t)$—giving us a version of NIBA including linear vibronic coupling and allowing us to compute generalized Marcus rates (and short-time dynamics!) beyond the Condon approximation. As we are interested in describing photochemistry, we have derived these kernels using the photochemical initial condition: $p_1(0) = 1$ but the bath is initially in equilibrium with State 2. A full derivation is presented in the Appendix. In summary, to second order in perturbation theory in $\hat{V}$,

$$K^{(2)}(t) = K_c^{(2)}(t) + K_{nc}^{(2)}(t) \tag{4.8}$$

where $K_c^{(2)}(t)$ is the Condon kernel,

$$K_c^{(2)}(t, t_1) = 2V_0^2 \exp\left[-Q'(t-t_1)\right] \cos\left(\epsilon(t-t_1) \pm \phi(t, t_1)\right) \tag{4.9}$$

where

$$\phi(t, t_1) = Q''(t-t_1) - 2Q''(t) + 2Q''(t_1) \tag{4.10}$$

$$\begin{aligned} Q'(t) &= \frac{4}{\pi} \int_0^\infty \frac{J_{EG}(\omega)}{\omega^2} \left(1 - \cos(\omega t)\right) \coth\left(\frac{\beta\omega}{2}\right) \\ Q''(t) &= \frac{4}{\pi} \int_0^\infty \frac{J_{EG}(\omega)}{\omega^2} \sin(\omega t) \end{aligned} \tag{4.11}$$

and $K_{nc}^{(2)}$ is the non-Condon kernel,

$$
\begin{aligned}
K_{nc}^{(2)}(t,t_1) = 2\exp\left[-Q'(t)\right]\big[&S'(t-t_1)\cos\left(\epsilon(t-t_1)\pm\phi(t,t_1)\right) - S''(t-t_1)\sin\left(\epsilon(t-t_1)\pm\phi(t,t_1)\right) \\
&\left(\left(R'(t-t_1)-2R'(t)\right)\left(R'(t-t_1)-2R'(t_1)\right) - R''(t-t_1)^2\right)\cos\left(\epsilon(t-t_1)\pm\phi(t,t_1)\right) \\
&+\left(2\left(R'(t)+R'(t_1)-R'(t-t_1)\right)R''(t-t_1)\right)\sin\left(\epsilon(t-t_1)\pm\phi(t,t_1)\right) \\
&+2V_0\left(R'(t)+R'(t_1)-R'(t-t_1)\right)\cos\left(\epsilon(t-t_1)\pm\phi(t,t_1)\right) \\
&+2V_0R''(t-t_1)\sin\left(\epsilon(t-t_1)\pm\phi(t,t_1)\right)\big]
\end{aligned}
\tag{4.12}
$$

where

$$
\begin{aligned}
R'(t) &= \frac{2}{\pi}\int_0^\infty d\omega \frac{J_{cross}\left(\omega\right)}{\omega}\cos\left(\omega t\right) \\
R''(t) &= \frac{2}{\pi}\int_0^\infty d\omega \frac{J_{cross}\left(\omega\right)}{\omega}\coth\left(\frac{\beta\omega}{2}\right)\sin\left(\omega t\right)
\end{aligned}
\tag{4.13}
$$

and

$$
\begin{aligned}
S'(t) &= \frac{1}{\pi}\int_0^\infty d\omega J_V\left(\omega\right)\cos\left(\omega t\right)\coth\left(\frac{\beta\omega}{2}\right) \\
S''(t) &= \frac{1}{\pi}\int_0^\infty d\omega J_V\left(\omega\right)\sin\left(\omega t\right)
\end{aligned}
\tag{4.14}
$$

If we approximately neglect cross-correlation, $R'(t) = R''(t) = 0$, and Equation 4.12 simplifies:

$$
\begin{aligned}
K_{nc}^{(2)}(t) \approx\ & 2\exp\left[-Q'(t)\right]\times \\
& \left[S'(t-t_1)\cos\left(\epsilon(t-t_1)\pm\phi(t,t_1)\right)\right. \\
& \left.-S''(t-t_1)\sin\left(\epsilon(t-t_1)\pm\phi(t,t_1)\right)\right]
\end{aligned}
\tag{4.15}
$$

Other authors have arrived at similar expressions [266, 267]. We will assess the validity of this approximation for a relevant chemical problem in this chapter. We would like to note in particular that in this regime and at short times, the non-Condon kernel effectively modulates the electronic coupling. One can rewrite the above equations as

$$
K^{(2)}(t) = \frac{\langle V^2\rangle - \left[\lambda_V(t)\right]^2}{\langle V^2\rangle}K_c^{(2)}(t) \tag{4.16}
$$

where $\lambda_V(t)$ acts as an effective time-dependent reorganization energy along the coupling coordinate; it

is strictly positive. When averaging over the bath in this manner, we observe that non-Condon effects are strictly expected to slow down population transfer from $|1\rangle$ to $|2\rangle$. Other authors [266, 268, 269] have observed that by averaging over the bath in a different manner (which amounts to rewriting Equation 4.16 in terms of $\langle V \rangle^2$) amounts to a strict non-Condon speedup in population transfer. We also note that *diabatic* population transfer is slowed down by non-Condon effects. *Adiabatic* population transfer is thus *sped up*, which makes sense: non-Condon effects facilitate traversal through conical intersections, a fast nonradiative decay pathway.

4.3 Computational Details

4.3.1 Extracting spectral densities from molecular simulation

Following our discussion in Section 4.2.4, it is apparent that in order to map chemical dynamics on to the spin-boson model, we require a way to extract the bath spectral density (or densities) from molecular simulation. Many authors [254, 51, 120] have observed that the energy gap spectral density J_{EG} defined in equation 4.3 is related to the Fourier transform of the energy gap fluctuation autocorrelation function:

$$J_{EG}(\omega) = \frac{\beta\omega}{4} \int_0^\infty \langle \delta\Delta E(t) \delta\Delta E(0) \rangle \cos(\omega t)\, dt \tag{4.17}$$

where β is the inverse temperature, $\delta\Delta E(t) \equiv \Delta E(t) - \langle \Delta E \rangle$, and $\Delta E(t)$ is the energy gap, $\Delta E(t) \equiv E_2(t) - E_1(t)$. We recognize that (up to some factors of 2, which we have wrapped up in our definition of the non-Condon kernel, equation 4.12), the cross- and coupling spectral densities defined in equations 4.5 and 4.4 can be written in terms of the energy gap - coupling cross correlation function and the coupling autocorrelation function, respectively:

$$J_{cross}(\omega) = \frac{\beta\omega}{2} \int_0^\infty \langle \delta\Delta E(t) \delta V(0) \rangle \cos(\omega t)\, dt \tag{4.18}$$

$$J_V(\omega) = \beta\omega \int_0^\infty \langle \delta V(t) \delta V(0) \rangle \cos(\omega t)\, dt \tag{4.19}$$

where $\delta V(t) \equiv V(t) - \langle V \rangle$.

Using these relations, we are able to map time correlation functions—quantities which we can readily extract from molecular simulation—on to the linear vibronic coupling Hamiltonian—a Hamiltonian with an in-principle numerically exact dynamical solution. In the remainder of this section, we discuss in detail how we extract the relevant information from simulation for a simple molecular system. In the following sections, we discuss the short-time and long-time dynamics which result from this mapping.

4.3.2 Simulation details

4.3.2.1 Molecular dynamics simulations

Following our discussion in Section 4.2.4, it is apparent that in order to map chemical dynamics on to the spin-boson model, we require a way to extract the bath spectral density (or densities) from molecular simulation. Many authors [254, 51, 249, 120] have observed that the energy gap spectral density J_{EG} defined in equation 4.3 is related to the Fourier transform of the energy gap fluctuation autocorrelation function:

$$J_{EG}(\omega) = \frac{\beta\omega}{4} \int_0^\infty \langle \delta\Delta E(t) \delta\Delta E(0) \rangle \cos(\omega t)\, dt \tag{4.20}$$

where β is the inverse temperature, $\delta\Delta E(t) \equiv \Delta E(t) - \langle \Delta E \rangle$, and $\Delta E(t)$ is the energy gap, $\Delta E(t) \equiv E_2(t) - E_1(t)$. We recognize that (up to some factors of 2, which we have wrapped up in our definition of the non-Condon kernel, equation 4.12), the cross- and coupling spectral densities defined in equations 4.5 and 4.4 can be written in terms of the energy gap - coupling cross correlation function and the coupling autocorrelation function, respectively:

$$J_{cross}(\omega) = \frac{\beta\omega}{2} \int_0^\infty \langle \delta\Delta E(t) \delta V(0) \rangle \cos(\omega t)\, dt \tag{4.21}$$

$$J_V(\omega) = \beta\omega \int_0^\infty \langle \delta V(t) \delta V(0) \rangle \cos(\omega t)\, dt \tag{4.22}$$

where $\delta V(t) \equiv V(t) - \langle V \rangle$.

Using these relations, we are able to map time correlation functions—quantities which we can readily extract from molecular simulation—on to the linear vibronic coupling Hamiltonian—a Hamiltonian with an in-principle numerically exact dynamical solution. In the remainder of this section, we discuss in detail how we extract the relevant information from simulation for a simple molecular system. In the following sections, we discuss the short-time and long-time dynamics which result from this mapping.

4.3.3 Simulation details

4.3.3.1 Molecular dynamics simulations

In order to examine the non-Condon effects on electron transfer dynamics predicted by equation 4.12, we have examined the aqueous electron transfer self-exchange reaction

$$Fe^{II} + Fe^{III} \rightarrow Fe^{III} + Fe^{II}$$

All molecular dynamics simulations were performed using the GROMACS 4.6.5 software package [270]. Two iron atoms (van der Waals parameters $\sigma_i = 2.2$ Å, $\epsilon_i = 0.0323$ kcal/mol employing combination rule $\sigma_{ij} = \sqrt{\sigma_i \sigma_j}$ for both σ and ϵ [255]) were placed at their touching-sphere distance of 5.5 inside a periodic simulation box of dimensions 4 nm x 4.55 nm x 4.018 nm and then solvated with 2466 molecules of TIP3P water [271]. Iron atoms were allowed to interaction with solvent via nonbonded interactions only. For NVT runs, the simulation box was coupled to a Nose-Hoover thermostat at 300 K with a time constant of 200 fs. Electrostatics were treated with the Particle Mesh Ewald method [272] with a cutoff of 1.5 nm; van der Waals interactions were cut off after 1.4 nm. A harmonic restraining potential ($r_0 = 0.35$ nm, $k = 100.0$ kJ mol^{-1} nm^{-2}) was used in order to keep the two irons in close proximity to each other.

A 1 ns NVT equilibration run was performed followed by a 1 ns NVT production run, each with a timestep of 1 fs. 300 configurations were sampled randomly from the production run at intervals of 100 fs; from each of these starting configurations, a 50 ps NVE run with a timestep of 0.5 fs was performed in order to ensure that correlation functions were sampled in the correct ensemble. For the NVE runs, Coulomb interactions were treated with the Reaction Field Zero method [273] with a cutoff of 1.3 nm, for better energy conservation; van der Waals interactions were treated as before.

For each snapshot in each NVE simulation, the energy was computed twice: once with the original force field, and again with the charges on the two iron atoms swapped. The difference between these two energies is the energy gap, ΔE. The mean energy gap was subtracted from each data point to give fluctuations in the energy gap, $\delta\Delta E$. A 5 ps energy gap - energy gap time correlation function was computed using a shifting average over the data from each NVE run to give $\langle \delta\Delta E(t)\delta\Delta E(0)\rangle_{NVE}$; these correlation functions were then averaged over the 300 different NVE runs to give a the final energy gap - energy gap time correlation function at 300 K, $\langle \delta\Delta E(t)\delta\Delta E(0)\rangle_{NVE}$.

For these same snapshots, we additionally computed the coupling V using the *ansatz* outlined in the subsequent section. The mean coupling $\langle V\rangle$ was subtracted out from each value of $V(t)$ to give fluctuations in the coupling, δV. A 5 ps coupling - coupling time correlation function was computed in the same manner as for the energy gap correlation function (including the same averaging over many NVE trajectories) to give $\langle \delta V(t)\delta V(0)\rangle_{NVE}$. Plots of one NVE trajectory and the resulting correlation functions are shown in Figure 4-1.

4.3.3.2 *Ansatz* for the coupling

From our NVE production runs, we additionally extracted the coordinates of the two iron atoms and those of the twelve waters forming the first solvation shell (six in an octahedral configuration around each iron). In principle, one can compute the coupling using an *ab initio* method such as constrained density functional theory with configuration interaction [103, 105, 106, 47]; in practice, we found these computations to be quite challenging for this system [274] . As such, we treated the coupling semi-

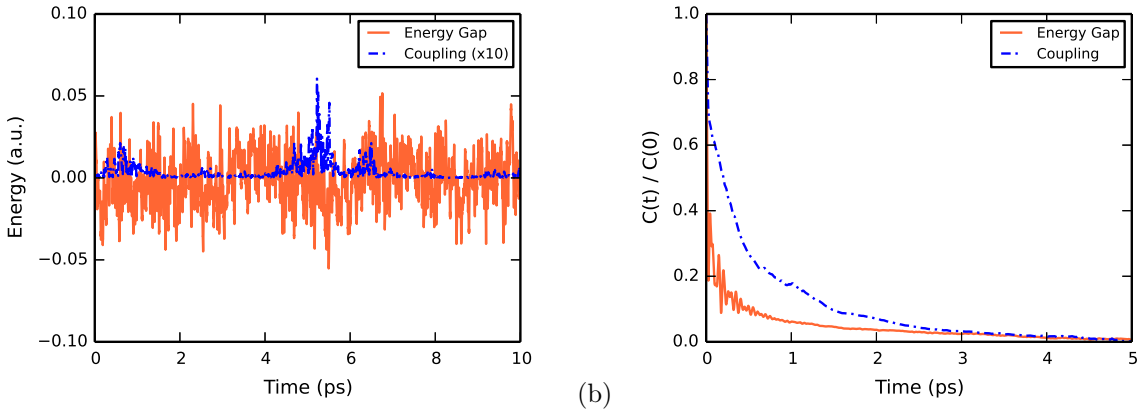

(a) (b)

Figure 4-1: (a) Energy gaps and couplings fluctuate rapidly on short timescales due to bath motions; the trajectory shown here is one of 300 NVE trajectories sampled from an NVT ensemble used to compute time correlation functions. (b) Energy gap - energy gap and coupling - coupling time autocorrelation functions are computed for this system. For illustration only, the correlation functions are normalized by C(0); unnormalized correlation functions were used in all calculations.

empirically.

The coupling should decay exponentially with distance [53, 58, 47], and, in order to allow for the existence of conical intersections, should be zero for some nuclear configuration [73]. One observable with both of these properties is d-orbital overlap. Figure 4-2 shows four snapshots from a single NVE molecular dynamics trajectory described in the previous section. As can be seen, two things occur over the course of the simulation: (1) the crystal field around each iron ion rotates, causing the d-orbitals on the irons to rotate with respect to each other; and (2) degenerate orbitals mix, causing the orbitals to change shape qualitatively. The latter effect occurs because the distorted octahedral environment causes electron transfer to occur from (and to) the lowest energy t_2g-like orbital on each iron atom, and the shape of that orbital fluctuates with the environment. We compute the overlaps, accounting for both factors, as detailed in Appendix 4.6.1.

The overlap of the d-orbitals on the two irons involved in our electron transfer process make an excellent proxy for a coupling. Like couplings, overlaps decay exponentially with distance, and since the orbitals are rotating with respect to one another throughout the course of the simulation, there is some rotation of the two molecules that will make the orbitals on one iron orthogonal to the orbitals on the other iron, giving an overlap of zero. We thus make an *ansatz* that the coupling is directly proportional to the overlap of the two d-orbitals involved in electron transfer, overlap, S:

$$V = \alpha S \tag{4.23}$$

Upon computing orbital overlaps at each step of our simulation, we transform them into couplings in such a way to recover the root-mean-square average of the literature values of $\langle V \rangle_{rms}$ reported for this

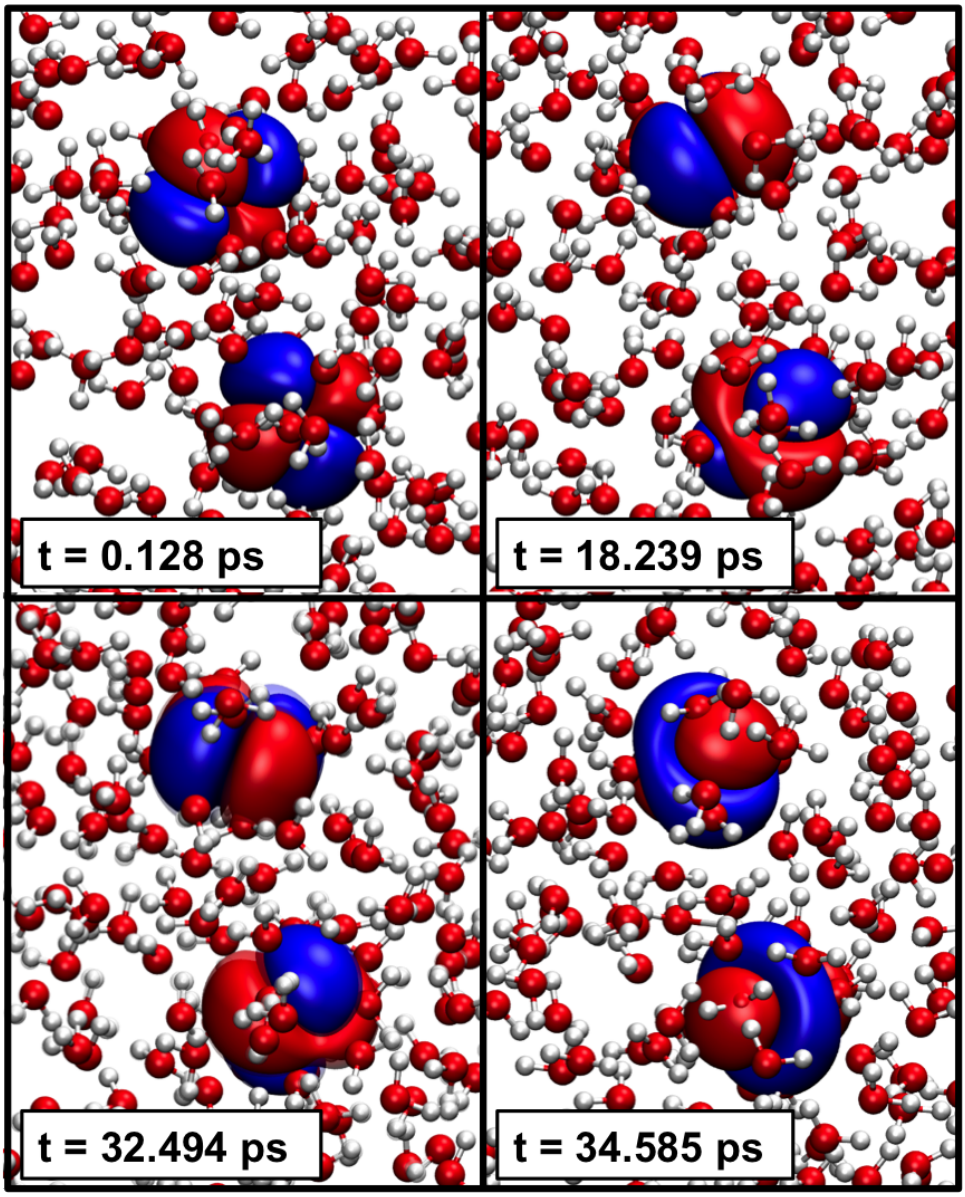

Figure 4-2: Over the course an NVE trajectory, the orbitals of the two irons change significantly. Due to both rotation of the crystal field around each iron and mixing of degenerate t_{2g} orbitals, both the orientation and qualitative character of the orbitals with respect to one another fluctuate. This causes large fluctuations in the overlap, meaning that even for this simple system, we cannot expect the coupling between the two orbital manifolds to remain constant—it, too, must fluctuate.

system [256], 57.3 cm^{-1} . We do this by first fixing the undetermined constant α using the average value of S,

$$\alpha = \frac{\sqrt{\langle V^2 \rangle}}{\langle S \rangle} \tag{4.24}$$

and then applying Equation 4.23 to compute couplings. It stands to reason that the coupling cannot be constant, even in this simple system: the orbital overlap changes rapidly with time, causing large fluctuations in the coupling.

4.3.3.3 Computing memory kernels and populations

In order to compute population dynamics and rates, equations 4.9 and 4.12 were implemented in FORTRAN 95. Since the spectral density $J(\omega)$ is sampled at a finite number of frequencies from molecular dynamics simulations, we chose to linearly interpolate between the sampled frequencies, as the integrals $Q^{''}(t)$, $R^{'}(t)$, and $S^{''}(t)$ are piecewise analytic for a piecewise linear spectral density. The three remaining integrals ($Q^{'}(t)$, $R^{''}(t)$, and $S^{'}(t)$) are not analytic; we computed these numerically using Simpson's Rule for each piecewise-linear segment, recursively subdividing the intervals until an absolute accuracy of 10^{-15} was reached. In order to avoid numerical divergences, we treated frequencies lower than 10^{-4} a.u. by taking the first 20 terms in the Taylor expansion about $\omega = 0$ of each integrand and evaluating the integral analytically.

Once the kernels were computed, the populations were computed using a standard algorithm for solving Volterra integrodifferential equations of the second kind [243] to solve equation 4.6 for $P(t) \equiv p_1(t) - p_2(t)$, the difference in population between states 1 and 2 as a function of time.

4.4 Results and Analysis

The spectral densities computed for iron self-exchange in water are showcased in Figure 4-3. The energy gap spectral density showcases the strength with which certain bath frequencies drive energy gap fluctuations; similarly, the coupling spectral density showcases the strength with which certain bath frequencies drive coupling fluctuations.

The energy gap spectral density has four features of note: a weak, broad, low-frequency band and three strong, sharp, high-frequency bands. These can be interpreted as bath modes driving outer-sphere and inner-sphere electron transfer, respectively. The three high-frequency bands can be assigned to typical vibrational frequencies observed in hexaaquairon complexes [275]. The role of outer-sphere bath modes and inner-sphere bath modes in driving iron self-exchange electron transfer has long been a subject of debate [251, 252, 253, 245, 254, 255, 256, 276, 277, 278], with a consensus that both types of modes can play a role but coupling-driven outer-sphere electron transfer often plays the bigger role. We observe

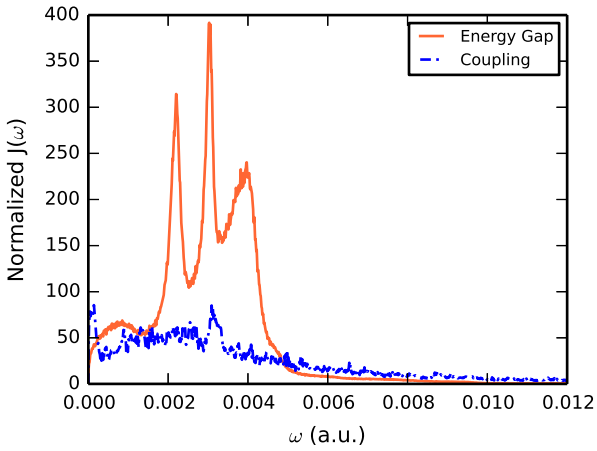

Figure 4-3: Energy-gap and coupling spectral densities are computed from the correlation functions shown in Figure 4-1 via equations 4.20 and 4.22. The energy-gap spectral density has high-frequency structure due to iron-oxygen vibrations—inner-sphere bath modes. While the coupling spectral density shows less structure, there is still substantial off-diagonal system-bath coupling at low and higher frequencies. For illustration purposes, the spectral densities shown are computed from the normalized correlation functions; unnormalized spectral densities were used in dynamics calculations.

here both modes of electron transfer driven by energy gap fluctuations occur: slow bath librations drive outer-sphere electron transfer and fast Fe-O vibrations drive inner-sphere transfer.

Energy gap fluctuations are not the only force driving electron transfer; though smaller in magnitude, coupling fluctuations also drive electron transfer, shown by the substantial magnitude of the coupling spectral density. Bath modes that drive fluctuations in the coupling tend to be lower-frequency in nature; in the present case, coupling fluctuations are coupled to iron-iron separation distance and the relative orientation of the irons' ligands with respect to one another. Both of these fluctuate slowly—very importantly, along independent characteristic physical coordinates. The decorrelation of these motions manifests itself in two distinct features in the spectral density.

Figure 4-4(a) showcases the short-time dynamics generated by the spectral densities in Figure 4-3. Plotted here are photochemical dynamics here computed using the kernels in Appendix A.3, as these dynamics more clearly illustrate the relative importance of non-Condon effects. Non-Condon effects do appreciably change the magnitude of population transfer, but not the overall profile; additionally, non-Condon effects strictly slow down diabatic population transfer (and thus speed up adiabatic population transfer)—in line with the analytic observation made in equation 4.16.

Unfortunately, because outer-sphere electron transfer dominates and $\langle V \rangle_{rms}$ is very small for this system, the magnitude of population transfer over the first hundred femtoseconds is small. Nevertheless, examining this system provides an important benchmark: if $\langle V \rangle_{rms}$ were bigger, non-Condon effects would play a vital role in population transfer. This can be seen by scaling $\langle V \rangle_{rms}$ by a factor of 10 so

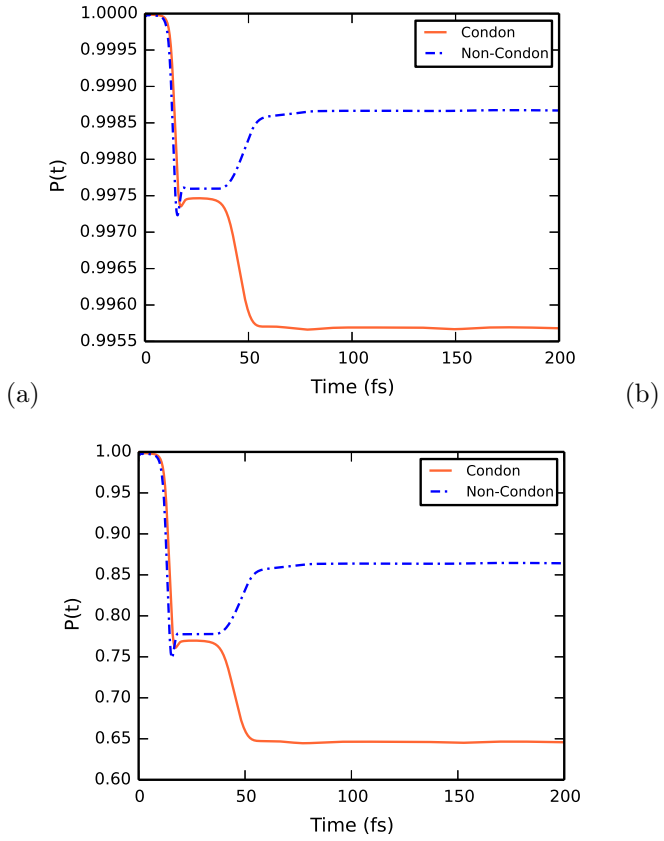

Figure 4-4: (a) Condon and non-Condon dynamics for hexaaquairon(II/III) self-exchange, with $\langle V \rangle_{rms} = 57.3$ cm^{-1}. Non-Condon effects are appreciable, even though charge-transfer is slow due to the small value of $\langle V \rangle_{rms}$ for this system. (b) If the coupling used is instead $\langle V \rangle_{rms} = 573$ cm^{-1}—a reasonable size for many condensed-phase charge-transfer systems—it becomes readily apparent that non-Condon effects cannot be neglected when studying condensed-phase electron transfer, as even for a simple metal self-exchange reaction in water there are substantial fluctuations in the coupling.

that it has a value of approximately 0.1 eV (a reasonable size for a coupling in, say, an organic charge-transfer system), and scaling the fluctuations in the coupling appropriately. The resulting dynamics are shown in Figure 4-4(b)—showcasing very appreciable diabatic population transfer over the first 100 femtoseconds. In the case where the coupling is larger (though still small enough that we can neglect fourth-order effects), non-Condon effects prevent 5% of the population from switching diabats by the time a steady-state decay to equilibrium is reached at approximately 55 fs—a non-negligible amount. This suggests that a substantial fraction of *adiabatic* charge transfer is facilitated by bath-induced fluctuations in the coupling.

We conclude our discussion with one important observation from this study: while non-Condon effects can change the *instantaneous* rate of relaxation towards equilibrium, they do not change the *overall* rate of electron transfer. Figure 4-4(c) contains a plot of the rate of change of the diabatic populations with time for both the Condon case and the non-Condon case. While the two curves do not align at short and intermediate times, they are identical at long times. While it is certainly true in this case, it is likely to be true in the general case that non-Condon effects will have a small impact on rates. To second order (and with a slow-bath, high-temperature approximation), that rate is the Marcus rate; to higher orders, it is more complicated. Nevertheless, this observation is important for rate processes and should be noted.

4.5 Conclusions

In this chapter, we have asserted that even in simple electron transfer systems, the Condon approximation will often result in short-time dynamics that are not quantitatively accurate. We have shown that for hexaaquairon self-exchange in water, the coupling is expected to fluctuate significantly on short (~10-100 fs) timescales. In more complex systems, this fluctuation in the coupling is necessary in order to predict photochemical dynamics accurately, including such phenomina as conical intersections. By developing a formalism based on the linear vibronic coupling Hamiltonian, we show that in iron self-exchange, for reasonable values of $\langle V \rangle_{rms}$, non-Condon effects are expected to substantially alter the amount of initial nonequilibrium charge transfer that occurs before the system reaches steady-state.

We hope to extend our work to provide more accurate dynamics by going to higher-orders in perturbation theory, so that we can safely tackle the intermediate- and strong-coupling regimes with conviction. We also wish to examine the effect of using polarizable force fields on the resulting spectral densities, as polarizable force fields are necessary for quantitatively-accurate solvent reorganization and thus photochemical dynamics [279].

4.6 Appendix

4.6.1 Computing the overlap between d-orbitals

According to crystal field theory, the electron transfer in this problem is from the t_{2g} manifold of one iron to the t_{2g} manifold of another iron; thus, the d-orbitals overlaps relevant to our problem are the overlaps of d_{xy}, d_{xz}, and d_{yz} on one iron atom with those of d_{xy}, d_{xz}, and d_{yz} on the other iron atom. Since there are manifolds of orbitals and thus 9 relevant overlaps involves in this electron transfer process, we choose to use as S in equation 4.23 the magnitude of the largest eigenvalue of the 3x3 overlap matrix in the subspace of the t_{2g} manifolds.

Evaluation of these overlaps not simple: it is confounded by the rotation of one iron with respect to the other. The process by which we arrive at the eigenvalue of the $t_{2g} - t_{2g}$ subspace of the overlap matrix can be enumerated as follows:

1. Using a STO-16g basis set which we parameterized to fit a Slater orbital with an exponent of 6.25 (as determined by Slater's Rules [89]), compute the 36 overlaps of the *unrotated* Cartesian d-orbitals d_{xx},d_{xy},d_{yy},d_{xz},d_{yz}, and d_{zz} on one iron atom with the other, and build the untransformed cartesian overlap matrix $S_{ij} = \langle d_i^{Fe(II)} | d_j^{Fe(III)} \rangle$.

2. Build the two rotation matrices $\mathbf{R_1^{'}}$ and $\mathbf{R_2^{''}}$ that transform the Cartesian basis vectors into the principle axes of molecule 1 and the principle axes of molecule 2, respectively. The principle axes can be determined from diagonalization of the inertia tensors for each hexaaquairon molecule. Special care must be taken to reorder the principle axes at each simulation step to ensure, e.g., that the rotated x axis remains in the x position and do not flip to the y or z position.

3. Build the matrices $\mathbf{T_{d1}^{'}}$ and $\mathbf{T_{d2}^{''}}$ that transform the Cartesian d-orbitals in the lab frame to the rotated frame for each molecule. These are 6x6 matrices for quadratic and bilinear coordinates which can be constructed using appropriate combinations of elements from the linear rotation matrices $\mathbf{R_1^{'}}$ and $\mathbf{R_2^{''}}$.

4. Build the matrix $\mathbf{Y}$ that transforms the Cartesian d-orbitals into the spherical d-orbitals

5. The rotated overlaps in the spherical harmonic basis can then be computed as

$$\mathbf{S}_{rot} = \mathbf{Y}^T \left[\mathbf{T_{d1}^{'}}\right]^T \mathbf{S} \mathbf{T_{d2}^{''}} \mathbf{Y} \tag{4.25}$$

Once the 6x6 $\mathbf{S}_{rot}$ is computed, the 3x3 block corresponding to the t_{2g} subspace, $\mathbf{S}_{rot}^{t2g}$, can be excised. The numerical value S to be used in equation 4.23 can be computed as

$$S = \max\left(\text{abs}\left(\text{eig}\left(\mathbf{S}_{rot}^{t2g}\right)\right)\right) \tag{4.26}$$

4.7 Acknowledgement

The work in this chapter was carried out jointly with Diptarka Hait.

Chapter 5

Fractional Charge Transfer and CDFT-CI Couplings

5.1 Introduction

As discussed in Section 1.1.1, working in a diabatic basis is appealing for numerous problems in chemistry, including electron transfer [47, 58], proton transfer [280], and valence bond theory [281]. Of central interest in any diabatic picture are the off-diagonal matrix elements of the Hamiltonian: the diabatic couplings. As many contemporary problems in chemistry such as electron transfer are often more tractable to study in a diabatic basis, various methods have been proposed to efficiently and accurately compute diabatic couplings [282, 283, 284, 285, 286, 287]. Constrained density functional theory with configuration interaction (CDFT-CI) has emerged as one such tool that, with proper application of chemical intuition, can provide an accurate approximation to the couplings with minimal computational cost [106, 288, 77, 289].

Unfortunately, CDFT-CI occasionally seems to be ill-behaved, especially at short distances [290]; in some cases, the coupling is hypersensitive to the choice of exchange-correlation functional, and it others it does not decay exponentially with distance, as it should [53]. Without running a large number of calculations, it can be difficult to determine whether the CDFT-CI coupling for a particular system is trustworthy, or if a alternative method must be used. In this chapter, we do two things: We first explain one reason why CDFT-CI fails in certain situations; we then present a metric that shows when the coupling predicted by CDFT-CI can be trusted and when it should be treated with suspicion.

5.2 Theory

5.2.1 Motivation of the Problem

An overview of CDFT and CDFT-CI has been provided in Section 1.2.1. In summary, CDFT can be used to construct approximate diabats, $|D\rangle$ and $|A\rangle$ with energies E_D and E_A (respectively) by using an effective Kohn-Sham potential to solve the Kohn-Sham equations subject to a constraint with weighting function $w_C(\mathbf{r})$ and Lagrance multiplier V_C,

$$V_{KS}^{eff} = V_{KS} + V_C w_C(\mathbf{r}) \tag{5.1}$$

By using the states $|D\rangle$ and $|A\rangle$ as the basis of a configuration-interaction calculation, the coupling V between these two states can be estimated as

$$\begin{aligned} V &= \left[\frac{E_D + E_A}{2} + \frac{V_{CD}w_{CD} + V_{CA}w_{CA}}{2}\right]\langle D|A\rangle \\ &\quad -V_{CD}\langle D|w_{CD}|A\rangle - V_{CA}\langle D|w_{CA}|A\rangle \end{aligned} \tag{5.2}$$

where w Of particular note is that this estimate of the coupling decays as states $|D\rangle$ and $|A\rangle$—which, in typical applications of CDFT-CI, are often separated from each other spatially—get further apart from one another. CDFT-CI couplings should even exhibit exponential decay (as one would expect a diabatic coupling would behave)[53], since, as can be seen in equation 5.2, the major component of the coupling is proportional to a wavefunction overlap.

Figure 5-1(a) shows the ideal case where we expect CDFT-CI to predict physical couplings. In this case, each CDFT state is localized on one molecular center. As the distance between the constraint centers goes to zero, the overlap, $\langle D|A\rangle$, and the matrix elements of the constraint potentials, $\langle D|w_{CA}|A\rangle$ and $\langle D|w_{CD}|A\rangle$, decay exponentially, as expected. For charge-transfer states, $|D\rangle$ describes a state where the extra electron is localized on one center, and $|A\rangle$ describes a state where the extra electron is localized on the other center.

Occasionally, we and others [290] have observed that the CDFI-CI coupling behaves unphysically. As part of the work in Chapter 4, we attempted to compute diabatic couplings for hexaaquairon(II) / hexaaquairon(III) self-exchange; the couplings are plotted in Figure 5-2. It can be seen in the figure that the couplings typically do not decay exponentially with distance. The question naturally arises: How can we explain this? Similarly, we occasionally observe a hypersensitivity of the CDFT-CI coupling to the percent Hartree-Fock exchange present in the exchange-correlation functional; in extreme cases, like in Figure 5-2, the coupling can span 5 orders of magnitude as the amount of exact exchange increases from 0% to 100%. We must also ask ourselves: how can we explain this effect, and is it related to the non-exponential decay of the coupling with distance?

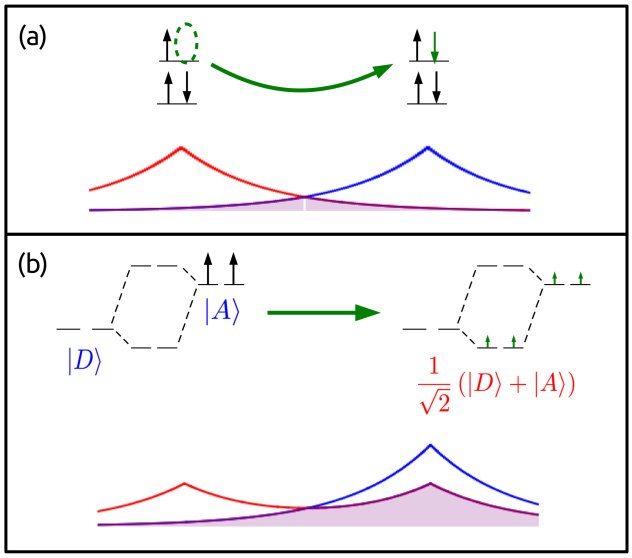

Figure 5-1: (a) In systems without degeneracies or near-degeneracies, the donor and acceptor wavefunctions (depicted in red and blue, respectively) are localized on the donor and acceptor, respectively. As the donor and acceptor are pulled apart, the wavefunction overlap (depicted in purple) and thus the coupling decays exponentially to zero. (b) In systems with degenerate electronic states near the HOMO, such as transition metal complexes, donor and acceptor wavefunctions can be delocalized and their overlap may not decay to zero at large distances. While the physical process typically involves transfer of a single electron from a single orbital, in this situation CDFT often describes the transfer of several fractions of an electron from several nearly-degenerate orbitals.

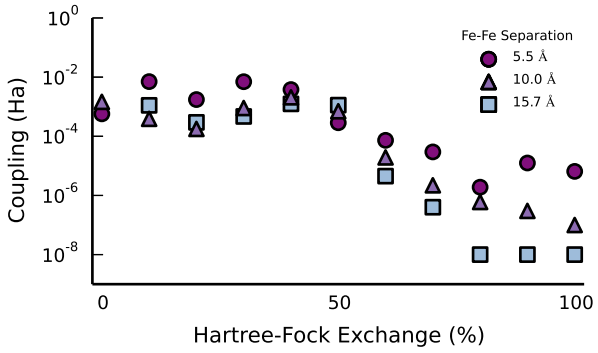

Figure 5-2: Diabatic couplings in atomic units as a function of percent Hartree-Fock exchange (x in equation 5.5) for hexaaquairon(II) / hexaaquairon(III) electron self-exchange in water. Different data series represent different iron-iron separation distances. Geometries were sampled as described in Chapter 4; one solvation shell past the coordination waters was included in the QM calculation. Depending on what fraction of Hartree-Fock exchange is used, the coupling computed spans five orders of magnitude, and does not decay exponentially (or at all) with distance.

We can answer these questions with a thought experiment. The constrained density states $|D\rangle$ and $|A\rangle$ can often be pictured as being comprised of single orbitals, $|\phi_D\rangle$ and $|\phi_A\rangle$. The electron transfer process simulated by CDFT-CI takes an electron from $|\phi_D\rangle$ and puts it in $|\phi_A\rangle$, as pictured in Figure 5-1(a). In this case, as $|D\rangle$ and $|A\rangle$ are separated to infinity, the overlap $\langle D|A\rangle$ (and thus the CDFT-CI coupling) decays exponentially to zero.

This ansatz may or may not actually be the case, since a CDFT calculation constrains the density and not the Kohn-Sham orbitals. Indeed, for systems with degenerate (or nearly degenerate) frontier orbitals, such as iron, one could easily imagine the donor and acceptor states being comprised of *multiple* orbitals, some of which are spatially delocalized. An example may be that $|D\rangle = |\phi_{D1}\phi_{D2}\rangle$ and $|A\rangle = \frac{1}{2}|\phi_{D1+A1}\phi_{D2+A2}\rangle$, where $|\phi_{D1+A1}\rangle = |\phi_{D1}\rangle + |\phi_{A1}\rangle$, and the subscripts D and A notate whether the orbital is localized on donor or acceptor, respectively. This scenario is depicted in Figure 5-1(b). This corresponds to transferring *parts* of *multiple* electrons to each of *several* different orbitals. In this case, the overlap $\langle D|A\rangle$ is non-zero even when the donor and acceptor are very far apart: for the present example,$\langle D|A\rangle = \frac{1}{2}$ at infinity. The resulting coupling thus does not decay to zero, as observed in the case of hexaaquairon self-exchange; it also depends heavily on the percentage of Hartree-Fock exchange, as this determines how favorable fractional spins are. Based on this logic, we hypothesize that the transfer of multiple fractional charges largely explains the unusual results which we sometimes observe from CDFT-CI.

5.2.2 Proposed diagnostic tool

If we can detect when partial charge transfer occurs, we should be able to diagnose when CDFT-CI gives reliable estimates of the coupling and when it does not. Fortunately, this information exists in the output of a CDFT-CI calculation: it is encoded in the difference density matrix between state $|D\rangle$ and $|A\rangle$,

$$\mathbf{P}_{diff} = \mathbf{P}_{|D\rangle} - \mathbf{P}_{|A\rangle} \tag{5.3}$$

When a whole electron is transferred, $\mathbf{P}_{diff}$ has exactly one eigenvalue of -1 (corresponding to an electron being transferred from an orbital on the donor to an orbital on the acceptor) and exactly one eigenvalue of +1 (corresponding to a hole being transferred from an orbital on the acceptor to an orbital on the donor). The rest of the eigenvalues are very small, corresponding to small amounts of valence orbital relaxation due to the electron transfer process, or numerically zero, corresponding to core orbitals unaffected by the electron transfer.

For the situation depicted in Figure 5-1(b), we expect the eigenvalues of $\mathbf{P}_{diff}$ to be quite different. In this scenario, most eigenvalues are still either 0 or ± 1, but in addition we expect a few significant eigenvalues between 0 and 1, reflecting partial charge transfer between donor and acceptor. These eigenvalues

Table 5.1: Summary of Results. $p^{(\alpha)}$ and $p^{(\beta)}$ are averaged over all distances and fractions of Hartree-Fock exchange studied (except where noted). Where $p^{(\alpha)}$ and $p^{(\beta)}$ are bolded, we expect CDFT-CI to be unreliable. Exponential fit R^2 computed using 20% Hartree-Fock exchange (except where noted).

System	$p^{(\alpha)}$	$p^{(\beta)}$	Exponential fit R^2
$[\text{Cyclohexane}]_2^+$	0.01	0.01	0.97
Ne_2^+	0.02	0.01	0.98
Zn_2^+	0.02	**0.16**; 0.01*	0.998
$\text{Hexaaquairon}^{2+/3+}$	**0.28**	**0.27**	0.48
$Fe^{2+/3+}$	**0.15**	0.01	0.41†
Polyene	0.02	**0.13**	0.28

*$p^{(\beta)} = 0.16$ at 2 Å and 0.01 at 4.5 Å

†R^2 computed using 10% Hartree-Fock exchange

are too big for orbital relaxation, but too small for whole electron transfer. Thus, if $\mathbf{P}_{diff}$ has a few significant eigenvalues between around 0 and 1, we would expect that CDFT-CI should give unreliable couplings.

In order to avoid having to explicitly look at every eigenvalue of $\mathbf{P}_{diff}$, we can instead look at the sum

$$p = \frac{1}{4}\sum_j \lambda_j^2 - \lambda_j^4 \tag{5.4}$$

where the λ_j are the eigenvalues of the difference density matrix $\mathbf{P}_{diff}$. If the eigenvalues are only +1, -1, or 0, this metric will be 0; for any other values, it will be a finite number greater than 0. Our metric p is small if we have whole charge transfer, as only the very small orbital relaxation eigenvalues contribute. Thus, in order to test whether or not CDFT-CI couplings are reliable, we can compute p as in equation 5.4. A small value of p indicates whole charge transfer whereas a large value of p indicates partial charge transfer, giving us a quantitative metric with which to test our hypothesis.

5.3 Results for test systems

We now tabulate results for several sample systems. All calculations were performed in a modified version of Q-Chem 4.2 [172] using the 6-31g* basis set and a modified version of the PBE0 functional:

$$E_{xc} = xE_{HF}^x + (1-x)E_{PBE}^x + E_{PBC}^c \tag{5.5}$$

where, unless otherwise noted, $x = 0.2$. All calculations were unrestricted and performed with symmetry off, with a grid of 74 radial points and 302 angular points. Since unrestricted calculations were performed, we examined the difference density matrix for alpha and beta electrons, $\mathbf{P}_{diff}^{(\alpha)}$ and $\mathbf{P}_{diff}^{(\beta)}$, separately, to compute $p^{(\alpha)}$ and $p^{(\beta)}$. Table 5.1 summarizes the main results of this study. Figure 5-3 summarizes the distance dependence of CDFT-CI couplings for all test systems studied.

5.3.1 "Good" systems

To begin with, we examine some simple examples where the frontier orbitals are non-degenerate; in these systems, we expect CDFT-CI to behave sensibly. In order to determine whether this is true, and, more importantly, whether our metric p informs us that this is true, we study the cyclohexane cation dimer. This electron transfer system has little degeneracy, so we expect good behavior. The constraints are applied such that state $|D\rangle$ has the hole constrained to one molecule in the dimer, and state $|A\rangle$ has the hole constrained to the other molecule. Both $p^{(\alpha)}$ and $p^{(\beta)}$ are equal to 0.01. Such small values of p indicate whole electron transfer; as such, we expect the CDFT-CI coupling to be well-behaved. This is indeed the case: as we separate the cyclohexane cation dimer from 5 Å to 8 Å, the coupling decreases exponentially with a decay exponent of -1.0 ($R^2 = 0.97$).

We extend our study to some very simple systems which could potential exhibit s-p or s-d degenracy: diatomic cations. The cation of the Ne dimer, Ne_2^+ is the simplest many-electron electron transfer; if CDFT-CI is unreliable for such a system, there is no hope that it will work for more complicated systems. We construct our diabatic states such that the excess hole is localized on a single atom: $|D\rangle = [Ne^+]Ne$ and $|A\rangle = Ne[Ne^+]$. Fortunately, CDFT-CI predicts exponential decay of the coupling with distance: As the dimer is separated from 2.5 Å to 4 Å with a CDFT-CI calculation performed every 0.5 Å, the logarithm of the coupling decays linearly with a slope of -1.47 ($R^2 = 0.98$). For each distance, $p^{(\alpha)} = 0.02$ and $p^{(\beta)} = 0.009$; our metric correctly predicts that CDFT-CI works.

Slightly more complicated is the Zn cation dimer, Zn_2^+. CDFT-CI was benchmarked against this system [105], so we again expect the results to be reliable. Again, we separated the dimer from 2.5 Å to 4.5 Å, and again, as expected, the coupling decays exponentially with distance (decay exponent of -0.39, $R^2 = 0.998$). Cave and Newton report couplings of ~10 mHa at a separation distance of 5 Å [291], which is roughly what we observe at our largest separation distance of 4.5 Å. Averaged over distance, $p^{(\alpha)} = 0.02$ for this system. $p^{(\beta)}$ is less well-behaved: the metric gets as high as 0.16 at 2 Å, though it get progressively smaller at larger distances until it drops to 0.01 at 4.5 Å. Unfortunately, this represents a false positive of our metric. While the CDFT-CI coupling is well-behaved here, we assert that a large value of $p^{(\beta)}$ at short distances indicates that there is substantial fractional charge transfer between the CDFT states and thus the CDFT-CI succeeds only through fortuitous cancellation of errors.

5.3.2 "Bad" systems

CDFT-CI does not work well for all classes of charge-transfer systems; our primary motivation for developing the metric p was to be able to determine *a priori* which systems CDFT-CI fails for. Figure 5-2 summarizes perhaps the biggest failing of CDFT-CI we have observed to date, in the computation of a coupling for electron self-exchange of hexaaquairon(II) / hexaaquairon(III) in water. As shown in the figure, the computed coupling spans 5 orders of magnitude as the fraction of Hartree-Fock exchange is

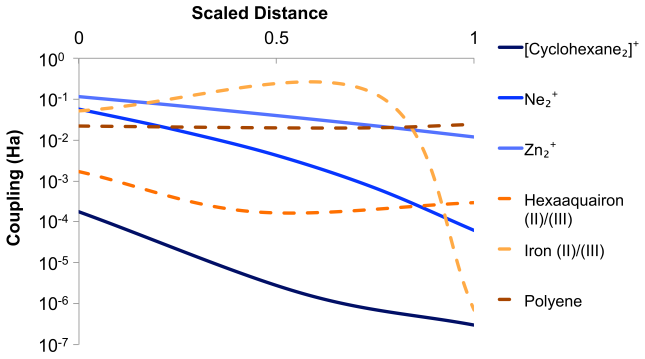

Figure 5-3: CDFT-CI coupling (in Hartree) as a function of distance for each system studied. For the purposes of this figure, all distances were translated by the shortest distance studied, such that the shortest distance is reported as "0". Additionally, all other distances studied are reported as a fraction of the largest distance studied (which is designated as "1"). The three systems plotted in blue decay roughly exponentially; the three in orange do not decay.

increased—behavior which is not observed for any of the "good" cases. Additionally, the coupling does not decay exponentially as the irons are separated; in some cases (such as 20% Hartree-Fock exchange), the coupling does not decay with distance at all. Averaged across both percent Hartree-Fock exchange and distance, $p^{(\alpha)} = 0.28$ and $p^{(\beta)} = 0.27$, with neither metric dropping below 0.1 for any calculation performed; based on this, we conclude that significant partial charge transfer is occluding the accurate prediction of the coupling for this system. The likely cause of this partial charge transfer is d-orbital near-degeneracy caused by the solvent crystal field splitting, though solvent-mediated superexchange may also be at play [292]. Other have estimated the coupling matrix element for this system at ~0.1 mHa [292, 256], which we can recover with 20-30% Hartree-Fock exchange.

In order to strip out the possibility of superexchange, we repeated the coupling calculation for iron(II)/iron(III) self-exchange with all solvent stripped out. The oxygen atoms were replaced by point charges with magnitude $q = -0.25$ atomic units in order to qualitatively preserve the crystal field splitting. Again, the couplings do not decay exponentially with distance (of the available data, the best fit is $R^2 = 0.41$ at 10% Hartree-Fock exchange); nor are they stable as the fraction of Hartree-Fock exchange increases, varying as much as 4 orders of magnitude. Somewhat disturbingly, at short distances (2 Å), the difference density metrics $p^{(\alpha)}$ and $p^{(\beta)}$ do not predict the failure of CDFT-CI: the average value of $p^{(\alpha)}$ at this distance is 0.03, and that of $p^{(\beta)}$ is 0.01. At larger distances (4 Å), the metric *does* predict the observed catastrophic failure of CDFT-CI, with $p^{(\alpha)} = 0.15$, indicating significant partial charge transfer. Thus it should be noted that while quite useful, this metric is not perfect. While superexchange may be partially to blame for poor CDFT-CI couplings in the hexaaquairon self-exchange system, CDFT-CI still fails to predict stable couplings when sources of superexchange are removed, leaving orbital degeneracy as the primary cause of partial charge transfer.

CDFT-CI fails not only for certain classes of transition metal systems, but also for certain organic

systems, including polyenes. Polyenes have small band gaps and thus nearly degenerate frontier orbitals; as a result, we expect CDFT-CI to predict couplings for these molecules poorly. To demonstrate this effect, we examine hole transfer from perhydroxylbenzene to perfluorobenzene connected by a polyene chain of varying length. Geometries were optimized with 6-31g*/PBE0. The couplings behave as expected: As a function of fraction Hartree-Fock exchange, they span approximately one order of magnitude; and as the polyene chain gets longer, the couplings do not decay exponentially (and for some fractions of Hartree-Fock exchange, even increase as donor-acceptor distance increases!). The density difference diagnostic behaves as expected: $p^{(\alpha)} = 0.02$ and $p^{(\beta)} = 0.13$ averaged over all distances and fractions of Hartree-Fock exchange studied, again indicating partial charge transfer from nearly-degenerate orbitals.

5.4 Conclusions

In this chapter, we have indicated that CDFT-CI can sometimes predict couplings which do not decay exponentially with distance and/or show hypersensitivity to the amount of exact exchange in the exchange-correlation functional. We have hypothesized that this problem is present in electron transfer systems where fractions of electrons are transmitted from donor to acceptor. Fractional electrons indeed have a long history in density functional theory [293] and are especially problematic in cases with large amounts of static correlation, or orbital degeneracy [294, 295].

We have examined cases where we expect small amounts of static correlation, such as noncovalent organic dimers, and cases where we expect large amounts of static correlation, such as transition metal complexes. Based on our data, the best rule of thumb seems to be that when $p < 0.05$, CDFT-CI couplings typically decay exponentially with distance and are stable with respect to fraction of exact exchange. When $p \geq 0.05$, the couplings are typically not reliable. This metric is not perfect, but it fits well with most of the data.

While not perfect, the metric p is generally good for predicting whether or not to trust CDFT-CI couplings. When p is large and CDFT-CI couplings cannot be trusted, it is unclear how reliable couplings can be extracted. In such cases, any method based on orbital overlaps, such as CDFT-CI, will fail. It is important to note that it is not equation 5.2 that is erroneous, but rather that in these cases the CDFT states (or at least ones that come from approximate functionals) have the wrong physical character. In such a situation, it is hard to imagine any coupling formula working well; instead, to predict accurate couplings, one would need a better description of the electronic structure of the monomers. Based on this diagnostic, we observe that there is room for figuring out ways to improve CDFT-CI, or better ways to compute couplings. Recent work on local scaling corrections in DFT [296] may show promise. In the meantime, we hope that the metric communicated in this contribution helps determine when the couplings computed from CDFT-CI can be trusted.

Chapter 6

Conclusion

Electron transfer in solvent is a very challenging problem for computers due to the large number of degrees of freedom that must be accounted for quantum-mechanically, but it has very important technological and environmental applications. In this thesis we have examined in detail one of these important applications, artificial catalytic water splitting, using several DFT-based methods. We additionally examined the detailed short-time dynamics of electron transfer for some model systems in the context of system-bath models based on the spin-boson Hamiltonian. We developed a dynamics approach based on high-order resummations of generalized master equation memory kernels, showing that at a high enough order and with the appropriate resummation, the dynamics are convergent; additionally, we extended our formalism to treat fluctuations in electronic couplings, showing that these fluctuations could enhance population transfer between adiabats at short times. We finally examined critically the reliability of the computation of CDFT-CI couplings, which are used in a variety of condensed-phase electron transfer applications.

The density functional thermochemistry and polarizable QM/MM methodologies applied in Chapter 2 allowed us to make various predictions about artificial catalytic water splitting. We showed that thermochemical screens of catalyts based on the stability of their mechanistic intermediates can open up regions of design space not yet explored. We additionally showed that very accurate redox potentials can be computed using polarizable QM/MM simulations with explicit solvent, an accuracy which can be used as a gateway into studying barrier heights, reorganization energies, and redox kinetics. Our detailed analysis [19] reviews the sorts of computational methods that can be used to address open questions in redox catalytic.

Efforts to harness DFT models of structure and reactivity for computational screening of materials are already underway [31, 297, 298], and water oxidation catalysis is a natural target to include in such studies [36]. By combining electronic structure calculations with cheminformatic approaches, the necessary machinery for high-throughput screening of candidate materials is within reach and will likely produce useful leads in the near future. But neither cheminformatic approaches nor mechanistic studies

will attain their full potential without vigorous experimental collaboration. Input from experiments will help refine informatic approaches and will continue to push the limits of our mechanistic models. Together, theoretical and experimental mechanistic studies will continue to drive advances in artificial water oxidation catalysis.

Open questions in this area still remain. We limited our analysis in this thesis to small-molecule first-row metal dimers in octahedral coordination geometries with a very particular selection of oxidation and spin states. It remains to be seen how this analysis holds up (or changes) if any of these constraints are relaxed. Of particular interest is an extension of this work to ternary compounds, as catalysts containing more than 2 metals are a region of design space that we have yet left unexplored. Additionally, we mainly focused our work on a single mechanism; while we have shown that our conclusions should be applicable to chemically-similar mechanisms, it remains to be seen how these conclusions will change if we look at chemically dissimilar mechanisms. In particular, mechanisms involving intramolecular proton-coupled electron transfer (or just proton transfer) have been shown to potentially alter observed overpotentials [299]; modeling of related mechanistic intermediates may reveal helpful aspects of catalytic design not yet considered.

Moving towards the underlying theory of electron transfer in solvent, Chapter 3 outlined a methodology that can be used to study two-state systems interacting with a bath of harmonic modes. We showed that adding in corrections to fourth-order in time-dependent perturbation theory in the diabatic coupling to dynamical memory kernels in generalized master equations gave semi-quantitative to quantitative short-time dynamics for model baths [250]. The theory outlined in this chapter is not perfect; there exists room for improved resummation schemes, as well as for resummations involving kernels to even higher orders. We outline one resummation scheme based on constructing a Dyson-like series for the memory kernels in the Appendix. We believe that this resummation scheme may have a natural extension to higher-order perturbative effects, the inclusion of which will allow us to compute spin-boson dynamics numerically-exactly. We also believe that this resummation may be of use in extending our theory to N-level systems interacting with harmonic baths, to allow us to study electron-transfer processes involving multiple states.

Chapter 4 saw us extending and applying this memory kernel formalism to study a chemical electron transfer problem: iron self-exchange in water. We showed that allowing diabatic couplings to fluctuate—as is the case in the linear vibronic coupling model Hamiltonian—slowed down electron transfer in the diabatic basis, speeding it up in the adiabatic basis. We assert on the basis of this work that these model Hamiltonians are the simplest feasible model of condensed-phase conical intersections—phenomena of paramount importance in photochemistry.

Ultimately, we hope to use our formalism to study chemical systems with conical intersections. Many chemical systems contain conical intersections that can be directly modeled [300, 301, 43, 44, 302].

Direct observation of molecular relaxation through conical intersections via a mapping on to the linear vibronic coupling Hamiltonian will allow us to make predictions about nonradiative decay rates in photochemistry—an essential component to first-principles prediction of quantum yields. Even an approximate description of such photochemical dynamics will be invaluable towards predicting the photochemical properties of small molecules in the condensed phase.

Unfortunately, as we showed in Chapter 5, a key component in computing conical intersection dynamics—namely, dynamical trajectories of diabatic couplings—is still a challenge for electronic structure theory [274]. While CDFT-CI is an excellent tool for computing couplings in many cases, it sometimes fails, meaning we must rely on alternative methods [284, 291]. An avenue of research remains to develop a computational method that reliably predicts electronic couplings of both diabats and DFT approximate adiabats. We are presently exploring the possibility of using an alternative solution of the Hartree-Fock solutions to approximate coupling matrix elements directly from the transition density matrix.

The progress made in condensed-phase electron transfer dynamics outlined in this thesis has several important applications. We see several avenues for interesting exploration in electrochemistry. Because of its interesting electronic structure, redox catalysts based on graphene [303] have recently been discovered that could provide efficient routes towards producing hydrogen fuel cells. The work presented in this thesis could be used to understand how these novel catalysts work mechanistically, in order to refine their efficiency. Additionally, graphene can act as both a source and sink of electrons; studying the dynamics of electron transfer to and from this continuum of states may reveal insight into its catalytic nature.

Perhaps most excitingly, work on electron transfer dynamics beyond the Condon approximation provides an avenue for predicting quantum yields from first principle. Quantum yield prediction is a very difficult problem with a wealth of applications both in academia and industry [304, 305, 306]. As Marcus theory comes from a particular limit of the memory kernels for the spin-boson Hamiltonian, so too could a version of Marcus theory accounting for fluctuating couplings (and thus conical intersections) come from the same limit of the linear vibronic coupling Hamiltonian; such a rate theory may provide an avenue towards *ab initio* prediction of nonradiative rates and thus quantum yields [263].

Applications are not limited to molecules in solution: solid-phase charge-transfer dynamics can also be modeled using system-bath Hamiltonians. Of particular interest is charge transfer across organic-organic interfaces, essential for the development of novel organic photovoltaic devices. Non-Condon rate and dynamics calculations can be applied to such systems to predict their nonradiative relaxation rates and thus quantum yields, which could provide a computational screen for their use in solar cells.

Finally, we hope that some of the theoretical developments outlined in this thesis will see experimental realization. In particular, we see an avenue for materials science to design water oxidation catalysts based on some of the design principles outlined in Chapter 2, and for spectroscopists to model quantum coherences through condensed-phase conical intersections using some of the theoretical models outlined

in Chapters 3 and 4. Fluctuating couplings are a hallmark of condensed-phase electron transfer systems as others in our group have previously observed [117]. A critical examination of the applicability of the Condon approximation in problems of this class may have a lot to teach us about the electronic properties and electron dynamics of condensed-phase compounds, leading to innumerable innovations in solar energy materials in the decades to come.

Appendix A

Derivation of Spin-Boson Memory Kernels

A.1 Derivation of general expressions for $K_{11}^{(2)}$ and $K_{11}^{(4)}$ from time-dependent perturbation theory

Our starting point is time-dependent perturbation theory for the density matrix, $\rho(t)$. We're interested in deriving an expression for $K_{11}^{(2n)}$ and $K_{22}^{(2n)}$—quantities related to $\dot{p}_1$ and $\dot{p}_2$, the time derivatives of the populations of the two states. We shall examine $K_{11}^{(2n)}$ and p_1 in particular, but the steps in this derivation can easily be repeated with p_2 as the starting point to arrive at an expression for $K_{22}^{(2n)}$. Additionally, we will specifically derive the expressions for $K_{11}^{(2)}$ and $K_{11}^{(4)}$, but the result can easily be generalized to derive higher-order rate kernels.

In the interaction representation, we can write the population in state 1 as

$$p_1(t) = \mathrm{T}r_b \left[U(t)\rho(0)U^\dagger(t)|1\rangle\langle 1|\right] \tag{A.1}$$

where $U(t)$ is the time evolution operator $U(t) \equiv \exp\left[-i\hat{H}t\right]$, and the subscript "b" on the trace indicated a trace over all bath coordinates. To 4th order,

$$\begin{aligned} p_1(t) &= 1 + \mathrm{T}r_b \left[2\mathrm{Re}\left[U^{(2)}(t)\rho(0)\right]|1\rangle\langle 1|\right] \\ &\quad + \mathrm{T}r_b \left[2\mathrm{Re}\left[U^{(4)}(t)\rho(0)\right]|1\rangle\langle 1| \right. \\ &\quad \left. + U^{(2)}(t)\rho(0)U^{\dagger(2)}(t)|1\rangle\langle 1|\right] + ... \\ &\equiv 1 + V^2 p_1^{(2)}(t) + V^4 p_1^{(4)}(t) + ... \end{aligned}$$

where we have defined $p_1^{(2n)}$ in the last line and used the operator identity $\hat{O} + \hat{O}^\dagger = 2\mathrm{Re}\left[\hat{O}\right]$. Taking a time derivative and working through some algebra, one can show that

$$\dot{p}_1^{(2)}(t) = -2\int_0^t \mathrm{Re}\left[f_2^+(s_1)\right] ds_1 \tag{A.2}$$

$$\begin{aligned}\dot{p}_1^{(4)}(t) &= 2\int_0^t ds_1 \int_0^{t-s_1} ds_2 \\ &\left[\int_0^{t-s_1-s_2} ds_3 \mathrm{Re}\left[f_4^+(s_1,s_2,s_3)\right]\right. \\ &\left.+\int_{-s_1-s_2}^{t-s_1-s_2} dt_3 \mathrm{Re}\left[f_4^+(-s_1-s_2-s_3,s_1,s_2)\right]\right]\end{aligned} \tag{A.3}$$

where we have introduced two functions $f_2^+(s_1)$ and $f_4^+(s_1,s_2,s_3)$ defined as

$$f_2^+(s_1) \equiv V^2 \mathrm{Tr}_b\left[\hat{O}(s_1)\rho(0)\right] \tag{A.4}$$

$$f_4^+(s_1,s_2,s_3) \equiv V^4 \mathrm{Tr}_b\left[\hat{O}(s_1)\hat{O}^\dagger(s_2)\hat{O}(s_3)\rho(0)\right] \tag{A.5}$$

where we have defined $\hat{O}(t) \equiv e^{i\hat{h}_1 t}e^{-i\hat{h}_2 t}$, and $\hat{h}_1$ and $\hat{h}_2$ are defined through equation 3.2.

We can perform a similar expansion on equation 3.3 (using $p_1^{(0)} = 1 - p_2^{(0)} = 1$) to show that

$$\dot{p}_1^{(2)}(t) = -\int_0^t K_{11}^{(2)}(t-s)ds \tag{A.6}$$

$$\begin{aligned}\dot{p}_1^{(4)}(t) &= -\int_0^t \Big(K_{11}^{(2)}(t-s)p_1^{(2)}(s) \\ &\quad + K_{11}^{(4)}(t-s) + K_{22}^{(2)}(t-s)p_1^{(2)}(s)\Big) ds\end{aligned} \tag{A.7}$$

Comparing equations A.2 to A.6 and equations A.3 to A.7 (doing some algebra in the latter case) allows us to arrive at equations 3.6 and 3.7, the equations for $K^{(2)}$ and $K^{(4)}$ in terms of equations f_2^+ and f_4^+; all that remains is to work out the functional forms of these traces (i.e., prove the equality between equations 3.8 and A.4, and also equations 3.9 and A.5) . This result is general for any two-level system coupled to a bath, so long as the electronic coupling is constant; we have not yet specified the bath to be harmonic.

A.2 Derivation of the bath correlation functions f_2 and f_4 for the spin-boson problem using Gaussian coherent states

We now compute the traces in equations A.4 and A.5 for the special case of a harmonic bath. In order to make computation simple, we shall assume that the reduced density matrix describing the system initially contains no populations in state 2 and no coherences (i.e. its (1,1) element is unity, and all other elements are zero). We shall additionally assume that the bath is in equilibrium with a thermal heat reservoir of inverse temperature $\beta \equiv 1/k_B T$. This brings our list of assumptions up to 3:

1. The electronic coupling is constant;
2. The bath is harmonic and coupled to the system linearly to the system; and
3. The full density matrix at time t=0 can be represented as $\rho(0) = e^{-\beta \hat{h}_1} / \text{ Tr}\left[e^{-\beta \hat{h}_1}\right]$

Of particular importance is that *we have not assumed anything about the bath other than its harmonicity*, which should manifest in the form of our equations depending on a *general* spectral density function $J(\omega)$. In passing, we will also note that it should be possible to repeat this derivation relaxing assumption 1, though we shall leave this to future work.

In the position representation, a Gaussian coherent state $|p, q; \phi\rangle$ parameterized by average position q and average momentum p with phase ϕ can be written

$$\langle x|p, q; \phi\rangle = \left(\frac{\omega}{\pi}\right)^{1/4} \exp\left[-\frac{\omega}{2}(x-q)^2 + ip(x-q) + i\phi\right] \tag{A.8}$$

Note that for a harmonic oscillator, the phase $\phi(t)$ does not depend explicitly on t, only on $p(t)$ and $q(t)$ [307]; thus, phase space integration over p and q will eliminate ϕ as well. Nevertheless, we include it in the definition of our Gaussian coherent state for clarity, as will be made evident over the next few steps in the derivation.

Using these Gaussian coherent states as a basis, we can work out the traces. For brevity, we shall work out the fourth-order trace (equation A.5), as it is more related to the general case and the second-order trace has been previously computed elsewhere. The trace can be written as

$$f_4^+(s_1, s_2, s_3) = \frac{V^4}{Z} \int \langle p, q; \phi|\hat{O}(s_1)\hat{O}^\dagger(s_2)\hat{O}(s_3)e^{-\beta \hat{h}_1}|p, q; \phi\rangle dp_0 dq_0$$

where $Z \equiv \int \langle p, q; \phi|e^{-\beta \hat{h}_1}|p, q; \phi\rangle dpdq$ is the partition function, and the phase space integral is over all initial positions and momenta.

In order to compute this integral, we can utilize the property of Gaussian coherent states that their average position, momentum, and phase evolve classically in time. We can also exploit the fact that $\hat{h}_1$ and $\hat{h}_2$ are related by symmetry: since the bath is (by assumption) significantly larger than the system, the

bath Hamiltonians contain identical spectra, and only differ by some displacement δ along one coordinate. These two facts allow us to compute the action of the operator $e^{i\hat{h}_1 t}e^{-i\hat{h}_2 t}$ on the state $|p,q;\phi\rangle$ mode-by-mode. We shall perform this deconstruction, and then "reassemble" the complete bath in the final step. The two states of the system see a bath mode of frequency ω as the same one-dimensional harmonic well displaced horizontally by a distance δ and vertically by a distance ϵ, the energy bias between the states. The time evolution due to the (constant) energy bias ϵ can be factored out; the rest of the time evolution can be evaluated analytically according to the classical equations of motion for a harmonic oscillator [308]

$$\begin{aligned} e^{i\hat{h}_1 t}e^{-i\hat{h}_2 t}|p,q;\phi\rangle &= e^{i\epsilon t}|p(t),q(t);\phi(t)\rangle \\ q(t) &= q_0 - \delta\omega\left(\cos(\omega t)-1\right) \\ p(t) &= p_0 - \delta\omega\sin(\omega t) \\ \phi(t) &= \frac{\delta^2\omega}{2}\left(\cos(\omega t)-1\right)\sin(\omega t) - \delta\omega q_0\sin(\omega t) \end{aligned}$$

Acting the real time evolution operators to the left, and the imaginary time evolution operator to the right, we obtain

$$f_4^+(s_1,s_2,s_3) = \frac{V^4}{Z}\int\langle P(s_1,s_2,s_3),Q(s_1,s_2,s_3);\Phi(s_1,s_2,s_3)|p(-i\beta),q(-i\beta);\phi(-i\beta)\rangle dp_0 dq_0$$

definining

$$P(s_1,s_2,s_3) \equiv -p(s_1)+p(s_2)-p(s_3)$$

$$Q(s_1,s_2,s_3) \equiv -q(s_1)+q(s_2)-q(s_3)$$

$$\Phi(s_1,s_2,s_3) \equiv -\phi(s_1)+\phi(s_2)-\phi(s_3)$$

which is just the integral of the overlap of two Gaussians over all possible initial values of position and momentum. This can be computed analytically (inserting a resolution of the identity and using equation A.8) to derive an explicit form for $f_4(s_1,s_2,s_3)$ for a single bath mode. We were able to verify that equation 3.7 together with equation A.7 gives the correct fourth-order population for the one mode problem by solving the for the populations of this problem numerically-exactly through brute-force time propagation of the full density matrix.

A spectral density can be incorporated noting that a spectral density is just a way of specifying exactly what the harmonic displacement δ that each state "sees" at each frequency of the bath ω:

$$J(\omega) = \frac{\pi}{2} \sum_j \omega_j^3 \delta_j^2 \delta(\omega - \omega_j)$$

Putting all of this together, one arrives at equation 3.9. A similar (simpler) derivation can be used to arrive at equation 3.8, and the extension to calculate bath correlation functions involving five-time events, seven-time events, and higher is straightforward.

A.3 Derivation of the Photochemical Kernels to Fourth-order $K^{(2)}$ and $K^{(4)}$

We present here an explicit derivation of the photochemical memory kernels for the linear vibronic coupling Hamiltonian to fourth-order in perturbation theory. The lack of explicit time dependence in $\hat{H}_{LVC}$ implies that the overall density matrix of the system $\rho(t)$ evolves as

$$\rho(t) = e^{-it\hat{H}_{LVC}} \rho(0) e^{it\hat{H}_{LVC}} \tag{A.9}$$

Since we are only interested in the populations in states $|1\rangle$ and $|2\rangle$, we can trace out the bath modes and write:

$$p_1(t) = \mathrm{Tr}_{bath} \left[\rho(t)|1\rangle\langle 1|\right] \tag{A.10}$$

$$p_2(t) = \mathrm{Tr}_{bath} \left[\rho(t)|2\rangle\langle 2|\right] = 1 - p_1(t) \tag{A.11}$$

Treating the off-diagonal elements of $\hat{H}_{LVC}$ as perturbations allows us to expand $p_1(t)$ as a power series in terms of the off-diagonal elements. If we start purely at state $|1\rangle$, we have:

$$\rho(0) = \begin{pmatrix} \rho_B & 0 \\ 0 & 0 \end{pmatrix} \tag{A.12}$$

where ρ_B is the initial bath density matrix. We discuss two initial conditions:

1. The photochemical initial condition, $\rho_B = \dfrac{e^{-\beta \hat{h}_2}}{\mathrm{Tr}\left[e^{-\beta \hat{h}_2}\right]}$, where the system has been electronically excited from $|2\rangle$ to $|1\rangle$, but the bath modes have not yet had an opportunity to relax from their initial thermal equilibrium with $|2\rangle$.

2. The thermal initial condition, $\rho_B = \dfrac{e^{-\beta\hat{h}_1}}{\mathrm{Tr}\left[e^{-\beta\hat{h}_1}\right]}$, where the system starts in State 1 ($p_1(0) = 1$) in equilibrium with the bath.

We focus most of our discussion on the photochemical initial condition. This initial condition implies $p_1(0) = 1$ and so we have

$$p_1(t) = 1 + p_1^{(2)}(t) + p_1^{(4)}(t) \dots \tag{A.13}$$

where $p_1^{(2n)}(t)$ is the $2n^{\text{th}}$ order term in the series (odd order terms are zero with these initial conditions), which are all zero at $t = 0$ and can be determined using time-dependent perturbation theory.

We then define $\hat{h}_1, \hat{h}_2, \hat{O}(t)$ and $F_{2n}(t_1, t_2)$ such that

$$\hat{H}_{LVC} = \begin{pmatrix} \hat{h}_1 & V_0 + \sum_j V_j \hat{x}_j \\ V_0 + \sum_j V_j \hat{x}_j & \hat{h}_2 \end{pmatrix} \tag{A.14}$$

$$\hat{O}(t) \equiv e^{i\hat{h}_1 t} \left(V_0 + \sum_j V_j \hat{x}_j \right) e^{-i\hat{h}_2 t} \tag{A.15}$$

$$F_{2n}(t_1, t_2 \dots t_{2n}) \equiv \mathrm{Tr}\left[\prod_{i=1}^{n} \left(O(t_{2i-1}) O^\dagger(t_{2i}) \right) \rho_B(0) \right] \tag{A.16}$$

The populations $p^{(2n)}(t)$ can be obtained by integrating traces $F_{2n}(t_1, t_2 \dots t_{2n})$, which can be evaluated using a Gaussian coherent state basis as described in the previous section of this Appendix. Consequently, we find that for photochemical ρ_B we have:

$$\begin{aligned} F_2(t_1, t_2) &= \left((V_0 + \alpha(t_1, t_2)) (V_0 + \beta(t_1, t_2)) \right. \\ &\quad \left. + \gamma(t_1 - t_2) \right) f_2(t_1, t_2) \end{aligned} \tag{A.17}$$

where

$$f_2(t_1, t_2) = \exp\left[-i\epsilon(t_1 - t_2) - Q'(t_1 - t_2) - i\phi(t_1, t_2) \right] \tag{A.18}$$

and we define

$$\phi(t_1, t_2) \equiv Q''(t_1 - t_2) - 2Q''(t_1) + 2Q''(t_2) \tag{A.19}$$

$$\alpha(t_1, t_2) \equiv 2R'(t_1) - R'(t_1 - t_2) + iR''(t_1 - t_2) \tag{A.20}$$

$$\beta(t_1, t_2) \equiv 2R'(t_2) - R'(t_1 - t_2) + iR''(t_1 - t_2) \tag{A.21}$$

$$\gamma(t) \equiv S'(t) - iS''(t) \tag{A.22}$$

Here, $Q'(t)$, $Q''(t)$, $R'(t)$, $R''(t)$, $S'(t)$, and $S''(t)$ have been defined previously, in Equations 3.10 – 4.14. Note that for the spin-boson Hamiltonian, when the coupling is a constant (V_0), $\alpha = \beta = \gamma = 0$. In the case where we can neglect the cross-correlation, $R'(t) = R''(t) = 0$ and the above equations simplify:

$$F_2(t_1, t_2) \approx T_2(t_1, t_2) f_2(t_1, t_2) \tag{A.23}$$

where $f_2(t_1, t_2)$ is defined in Equation A.18 and we define

$$\begin{aligned} T_2(t_1, t_2) &\equiv \left(V_0^2 + \gamma(t_1 - t_2)\right) \\ &= \left(\langle V^2 \rangle + \gamma(t_1 - t_2) - \gamma(0)\right) \end{aligned} \tag{A.24}$$

When we can neglect cross-correlation, we can analogously write the fourth-order bath correlation function F_4 as

$$F_4(t_1, t_2, t_3, t_4) = T_4(t_1, t_2, t_3, t_4) f_4(t_1, t_2, t_3, t_4) \tag{A.25}$$

where

$$f_4(t_1, t_2, t_3, t_4) = \frac{f_2(t_1, t_2) f_2(t_2, t_3) f_2(t_3, t_4) f_2(t_1, t_4)}{f_2(t_1, t_3) f_2(t_2, t_4)} \tag{A.26}$$

and

$$\begin{aligned} T_4(t_1, t_2, t_3, t_4) = {} & T_2(t_1, t_2) T_2(t_3, t_4) + T_2(t_1, t_3) T_2(t_2, t_4) \\ & + T_2(t_1, t_4) T_2(t_2, t_3) - 2V_0^4 \end{aligned} \tag{A.27}$$

All that remains is to connect the bath correlation functions F_2 and F_4 to the memory kernels $K^{(2)}$ and $K^{(4)}$. From perturbation theory, these bath correlation functions are related to the populations by

$$p_1^{(2)}(t) = -2\int_0^t dt_1 \int_0^{t_1} dt_2 \mathrm{Re}\left[F_2(t_1,t_2)\right] \tag{A.28}$$

$$p_1^{(4)}(t) = 2\int_0^t dt_1 \int_0^{t_1} dt_2 \int_0^{t_2} dt_3 \int_0^{t_3} dt_4 \mathrm{Re}\left[F_2(t_1,t_2,t_3,t_4)\right] + \int_0^t dt_1 \int_0^{t_1} dt_2 \int_0^{t} dt_3 \int_0^{t_3} dt_4 F_2(t_2,t_1,t_3,t_4) \tag{A.29}$$

The memory kernels $K^{(2n)}(t,t_1)$ cannot be uniquely determined; however, kernels consistent with Equations A.28 and A.29 can be obtained by expanding the rate equations (Equation 4.6) in the coupling $\hat{V}$ and matching orders in perturbation theory by analogy. This results in the kernels

$$K_1^{(2)}(t,t_1) = 2\mathrm{Re}\left[F_2(t,t_1)\right] \tag{A.30}$$

which is consistent with A.28, and

$$\begin{aligned} K_1^{(4)}(t,t_1) &= -2\mathrm{Re}\left[\int_0^{t_1} dt_2 \int_0^{t_2} F_4(t,t_1,t_2,t_3)dt_3 + \int_0^{t} dt_2 \int_0^{t_2} F_4(t_1,t,t_2,t_3)dt_3\right] \\ &\quad + K_+^{(2)}(t,t_1)\int_0^{t_1} dt_2 \int_0^{t_2} K_1^{(2)}(t_2,t_3)dt_3 \end{aligned} \tag{A.31}$$

which is consistent with A.29.

We briefly consider the thermal initial conditions discussed at the start of this section. Under this set of initial conditions, only the form of f_2 changes on moving from photochemical initial conditions to thermal conditions; thus, all of the equations described in this section can be used to compute memory kernels under thermal initial conditions, making the substitution:

$$f_2(t_1,t_2) \rightarrow f_2^{th}(t_1 - t_2) \tag{A.32}$$

$$f_2^{th}(t) = \exp\left[-i\epsilon t - Q'(t) - iQ''(t)\right] \tag{A.33}$$

Importantly, the non-Condon piece of the kernels, T_2, remains the same so long as cross-correlations between energy gap fluctuations and coupling fluctuations can be neglected. The fourth-order kernels can be derived making the same substitution for f_2 and using equations A.26 and A.27.

For reference, the full second-order thermal kernel is

$$K_{th}^{(2)} = K_{th,c}^{(2)} + K_{th,nc}^{(2)}$$

where $K^{(2)}_{th,c}$ is the Condon piece,

$$K^{(2)}_{th,c}(t) = 2V_0^2 \exp\left[-Q'(t)\right] \cos\left[\epsilon t \pm Q''(t)\right] \tag{A.34}$$

and $K^{(2)}_{th,nc}$ is the non-Condon piece,

$$\begin{aligned} K^{(2)}_{th,nc}(t) \quad = \quad & 2\exp\left[-Q'(t)\right]\left[S'(t)\cos(\epsilon t \pm Q''(t)) - S''(t)\sin(\epsilon t \pm Q''(t))\right. \\ & + \left(\left(R'(t)\right)^2 - \left(R''(t)\right)^2\right)\cos(\epsilon t \pm Q''(t)) - 2R''(t)R'(t)\sin(\epsilon t \pm Q''(t)) \\ & \left. -2V_0\left(R'(t)\cos\left(\epsilon t \pm Q''(t)\right) - R''(t)\sin\left(\epsilon t \pm Q''(t)\right)\right)\right] \end{aligned} \tag{A.35}$$

The fourth-order generalization is straightforward.

A.4 A note on the backwards rate kernel, K_{22}

All of the results in the previous two sections can be applied as well to compute K_{22}. Only two things change:

1. We must compute the trace over the equilibrium configuration of state 2, which effectively means $\hat{h}_1 \leftrightarrow \hat{h}_2$ (and thus, by symmetry, $\delta/2 \leftrightarrow -\delta/2$) everywhere
2. The initial condition changes to $p_1(0) = 1 - p_2(0) = 0$, changing $K^{(2)}_{11}(s_2) \rightarrow K^{(2)}_{22}(s_2)$ in equation 3.7

Otherwise, the derivation proceeds virtually identically.

Bibliography

[1] J.-L. Brédas, D. Beljonne, V. Coropceanu, and J. Cornil. Charge-Transfer and Energy-Transfer Processes in π-Conjugated Oligomers and Polymers: A Molecular Picture. *Chem. Rev.*, 104(11):4971–5004, 2004.

[2] M. Grätzel. Solar Energy Conversion by Dye-Sensitized Photovoltaic Cells. *Inorg. Chem.*, 44(20):6841–6851, 2005.

[3] K. V. Wong, N. Perilla, and A. Paddon. Nanoscience and nanotechnology in solar cells. *J. Energy Resour. Technol.*, 136:14001, 2013.

[4] D. Li, H. Lv, Y. Kang, N. M. Markovic, and V. R. Stamenkovic. Recent Advances in the Development of Oxygen Reduction Reaction Catalysts for Low Temperature Fuel Cells. *Annu. Rev. Chem. Biol. Eng.*, 7(1):annurev–chembioeng–080615–034526, 2016.

[5] A. Kudo and Y. Miseki. Heterogeneous photocatalyst materials for water splitting. *Chem. Soc. Rev.*, 38(1):253–278, jan 2009.

[6] D. G. Nocera. The Artificial Leaf. *Acc. Chem. Res.*, 45(5):767–776, may 2012.

[7] J. J. Concepcion, J. W. Jurss, J. L. Templeton, and T. J. Meyer. One site is enough. Catalytic water oxidation by [Ru(tpy)(bpm)(OH2)]2+ and [Ru(tpy)(bpz)(OH2)]2+. *J. Am. Chem. Soc.*, 130(49):16462–16463, dec 2008.

[8] L.-P. Wang, Q. Wu, and T. Van Voorhis. Acid-base mechanism for ruthenium water oxidation catalysts. *Inorg. Chem.*, 49(10):4543–4553, may 2010.

[9] M. W. Kanan and D. G. Nocera. In situ formation of an oxygen-evolving catalyst in neutral water containing phosphate and Co2+. *Science*, 321(5892):1072–5, aug 2008.

[10] J. Suntivich, K. J. May, H. A. Gasteiger, J. B. Goodenough, and Y. Shao-Horn. A perovskite oxide optimized for oxygen evolution catalysis from molecular orbital principles. *Science*, 334(6061):1383–1385, dec 2011.

[11] M. Risch, K. Klingan, F. Ringleb, P. Chernev, I. Zaharieva, A. Fischer, and H. Dau. Water oxidation by electrodeposited cobalt oxides–role of anions and redox-inert cations in structure and function of the amorphous catalyst. *ChemSusChem*, 5(3):542–549, mar 2012.

[12] Y. Wang and H.-P. Cheng. Oxygen Reduction Activity on Perovskite Oxide Surfaces: A Comparative First-Principles Study of LaMnO3 , LaFeO3 , and LaCrO3. *J. Phys. Chem. C*, 117(5):2106–2112, feb 2013.

[13] L. Dou, J. You, Z. Hong, Z. Xu, G. Li, R. A. Street, and Y. Yang. 25th anniversary article: A decade of organic/polymeric photovoltaic research. *Adv. Mater.*, 25(46):6642–6671, 2013.

[14] J.-L. Brédas, J. E. Norton, J. Cornil, and V. Coropceanu. Molecular understanding of organic solar cells: the challenges. *Accounts Chem. Res.*, 42(11):1691–1699, 2009.

[15] A. P. Kulkarni, C. J. Tonzola, A. Babel, and S. A. Jenekhe. Electron transport materials for organic light-emitting diodes. *Chem. Mater.*, 16(23):4556–4573, 2004.

[16] Wolfgang Domcke, David R. Yarkony, and Horst Koppel, editors. *Conical Intersections: Theory, Computation and Experiment*. World Scientific Publishing Co. Pte. Ltd., Singapore, 2011.

[17] W. Domcke and D. R. Yarkony. Role of Conical Intersections in Molecular Spectroscopy and Photoinduced Chemical Dynamics. *Annu. Rev. Phys. Chem.*, 63(1):325–352, 2012.

[18] D. Balcells. *Insight into Metal-Catalyzed Water Oxidation from a DFT Perspective*. Elsevier Inc., 1 edition, 2016.

[19] M. G. Mavros, T. Tsuchimochi, T. Kowalczyk, A. Mcisaac, L.-P. Wang, and T. Van Voorhis. What Can Density Functional Theory Tell Us about Artificial Catalytic Water Splitting? *Inorg. Chem.*, 53:6386–6397, 2014.

[20] A. A. Peterson. Activity Descriptors for CO 2 Electroreduction to Methane on Transition-Metal Catalysts. *J. Phys. Chem. Lett.*, 3:251–258, 2012.

[21] J. P. McEvoy, J. A. Gascon, V. S. Batista, and G. W. Brudvig. The mechanism of photosynthetic water splitting. *Photoch. Photobio. Sci.*, 4(12):940–949, dec 2005.

[22] J. P. McEvoy and G. W. Brudvig. Water-splitting chemistry of photosystem II. *Chem. Rev.*, 106(11):4455–4483, nov 2006.

[23] E. M. Sproviero, J. A. Gascón, J. P. McEvoy, G. W. Brudvig, and V. S. Batista. Quantum mechanics/molecular mechanics study of the catalytic cycle of water splitting in photosystem II. *J. Am. Chem. Soc.*, 130(11):3428–3442, 2008.

[24] J. Cao and R. J. Silbey. Optimization of exciton trapping in energy transfer processes. *J. Phys. Chem. A*, 113(50):13825–13838, 2009.

[25] A. Ishizaki and G. R. Fleming. Quantum Coherence in Photosynthetic Light Harvesting. *Annu. Rev. Cond. Mat.*, 3(1):333–361, 2012.

[26] S. Curtarolo, G. L. W. Hart, M. B. Nardelli, N Mingo, S. Sanvito, and O. Levy. The high-throughput highway to computational materials design. *Nat. Mater.*, 12(3):191–201, 2013.

[27] G. Ceder, G. Hauthier, A. Jain, and S. P. Ong. Recharging lithium battery research with first-principles methods. *Mater. Res. Soc. Bull.*, 36:185–191, 2011.

[28] M. Boero, M. Parrinello, H. Weiss, and S. Huffer. A First Principles Exploration of a Variety of Active Surfaces and Catalytic Sites in Ziegler-Natta Heterogenous Catalysis. *J. Phys. Chem. A*, 105(21):5096–5105, 2001.

[29] L.-C. C. Lin, A. H. Berger, R. L. Martin, J. Kim, J. A. Swisher, K. Jariwala, C. H. Rycroft, A. S. Bhown, M. W. Deem, M. Haranczyk, and B. Smit. In silico screening of carbon-capture materials. *Nat. Mater.*, 11(7):633–641, 2012.

[30] L. Yu and A. Zunger. Identification of potential photovoltaic absorbers based on first-principles spectroscopic screening of materials. *Phys. Rev. Lett.*, 108:068701, 2012.

[31] J. Hachmann, R. Olivares-Amaya, S. Atahan-Evrenk, C. Amador-Bedolla, R. S. Sánchez-Carrera, A. Gold-Parker, L. Vogt, A. M. Brockway, and A. Aspuru-Guzik. The Harvard Clean Energy Project: Large-scale computational screening and design of organic photovoltaics on the World Community Grid. *J. Phys. Chem. Lett.*, 2(17):2241–2251, 2011.

[32] R. Olivares-Amaya, C. Amador-Bedolla, J. Hachmann, S. Atahan-Evrenk, R. S. Sánchez-Carrera, L. Vogt, and A. Aspuru-Guzik. Accelerated computational discovery of high-performance materials for organic photovoltaics by means of cheminformatics. *Energ. Environ. Sci.*, 4(12):4849, 2011.

[33] V. Viswanathan, H. A. Hansen, J. Rossmeisl, and J. K. Norskov. Universality in Oxygen Reduction Electrocatalysis on Metal Surfaces. *ACS Catal.*, 2:1654–1660, 2012.

[34] I. C. Man, H.-Y. Su, F. Calle-Vallejo, H. A. Hansen, J. I. Martínez, N. G. Inoglu, J. Kitchin, T. F. Jaramillo, J. K. Norskov, and J. Rossmeisl. Universality in Oxygen Evolution Electrocatalysis on Oxide Surfaces. *ChemCatChem*, 3(7):1159–1165, jul 2011.

[35] S. Diego, L. D. Carter, V. L. Pease, J. W. Hillhouse, O. G. N. Andersen, Y. Herman, J. Stroeve, M. M. Holland, W. Meier, T. Scambos, A. E. Oleinik, K. B. Barinov, E. Vermote, N. Saleous,

R. Simmon, and D. Herring. Identification of Non-Precious Metal Alloy Catalysts for Selective Hydrogenation of Acetylene. *Science*, 320:1320–1322, 2008.

[36] J. Greeley, T. F. Jaramillo, J. Bonde, I. B. Chorkendorff, and J. K. Norskov. Computational high-throughput screening of electrocatalytic materials for hydrogen evolution. *Nat. Mater.*, 5(11):909–13, nov 2006.

[37] M. Garcia-Mota, A. Vojvodic, H. Metiu, I. C. Man, H. Y. Su, J. Rossmeisl, and J. K. Norskov. Tailoring the activity for oxygen evolution electrocatalysis on rutile TiO2(110) by transition-metal substitution. *ChemCatChem*, 3(10):1607–1611, 2011.

[38] J. Greeley, I. E. L. Stephens, A. S. Bondarenko, T. P. Johansson, H. A. Hansen, T. F. Jaramillo, J. Rossmeisl, I. Chorkendorff, and J. K. Norskov. Alloys of platinum and early transition metals as oxygen reduction electrocatalysts. *Nat. Chem.*, 1(7):552–556, 2009.

[39] S. Chrétien and H. Metiu. Density functional study of the CO oxidation on a doped rutile TiO 2(110): Effect of ionic Au in catalysis. *Catal. Lett.*, 107(3-4):143–147, 2006.

[40] H. Y. Kim, H. M. Lee, R. G. S. Pala, V. Shapovalov, and H. Metiu. CO oxidation by rutile TiO2(110) doped with V, W, Cr, Mo, and Mn. *J. Phys. Chem. C*, 112(32):12398–12408, 2008.

[41] M. Mikkelsen, M. Jorgensen, and F. C. Krebs. The teraton challenge. A review of fixation and transformation of carbon dioxide. *Energ. Environ. Sci.*, 3(1):43, 2010.

[42] A. Warshel. Dynamics of reactions in polar solvents. Semiclassical trajectory studies of electron-transfer and proton-transfer reactions. *J. Phys. Chem.*, 86(7):2218–2224, 1982.

[43] S. Lobsiger, M. A. Trachsel, H. M. Frey, and S. Leutwyler. Excited-state structure and dynamics of keto-amino cytosine: The $1\pi\pi^*$ state is nonplanar and its radiationless decay is not ultrafast. *J. Phys. Chem. B*, 117(20):6106–6115, 2013.

[44] A. Nakayama, S. Yamazaki, and T. Taketsugu. Quantum chemical investigations on the nonradiative deactivation pathways of cytosine derivatives. *J. Phys. Chem. A*, 118(40):9429–9437, 2014.

[45] S. Shim, P. Rebentrost, S. Valleau, and A. Aspuru-Guzik. Atomistic study of the long-lived quantum coherences in the Fenna-Matthews-Olson complex. *Biophys. J.*, 102(3):649–660, 2012.

[46] U. Rau. Reciprocity relation between photovoltaic quantum efficiency and electroluminescent emission of solar cells. *Phys. Rev. B*, 76(8):1–8, 2007.

[47] T. Van Voorhis, T. Kowalczyk, B. Kaduk, L.-P. Wang, C.-L. Cheng, and Q. Wu. The Diabatic Picture of Electron Transfer, Reaction Barriers, and Molecular Dynamics. *Annu. Rev. Phys. Chem.*, 61(1):149–170, 2010.

[48] R. A. Marcus. On the Theory of Oxidation-Reduction Reactions Involving Electron Transfer. I. *J. Chem. Phys.*, 24(5):966, 1956.

[49] R. A. Marcus. On the Theory of Electron-Transfer Reactions. VI. Unified Treatment for Homogeneous and Electrode Reactions. *J. Chem. Phys.*, 43(2):679, 1965.

[50] R. A. Marcus. Electron Transfer Reactions in Chemistry: Theory and Experiment (Nobel Lecture). *Angew. Chem. Int. Ed. (English)*, 32(8):1111–1121, aug 1993.

[51] A. Nitzan. *Chemical Dynamics in Condensed Phases: Relaxation, Transfer, and Reactions in Condensed Molecular Systems.* Oxford Univ. Press, Oxford, 2006.

[52] F. A. Carey and R. J. Sundberg. *Advanced Organic Chemistry Part A: Structure and Mechanisms.* Spring Science+Business Media, LLC, New York, 5th edition, 2007.

[53] M. D. Newton and N. Sutin. Electron Transfer Reactions in Condensed Phases. *Annu. Rev. Phys. Chem.*, 35(1):437–480, 1984.

[54] G. L. Closs, L. T. Calcaterra, N. J. Green, K. W. Penfield, and J. R. Miller. Distance, stereoelectronic effects, and the Marcus inverted region in intramolecular electron transfer in organic radical anions. *J. Phys. Chem.*, 90(16):3673–3683, 1986.

[55] G. J. Kavarnos and N. J. Turro. Photosensitization by reversible electron transfer: theories, experimental evidence, and examples. *Chem. Rev.*, 86(2):401–449, 1986.

[56] D. Y. Yang and R. I. Cukier. The transition from nonadiabatic to solvent controlled adiabatic electron transfer: Solvent dynamical effects in the inverted regime. *J. Chem. Phys.*, 91(1):281, 1989.

[57] E. Akesson, G. C. Walker, and P. F. Barbara. Dynamic solvent effects on electron-transfer rates in the inverted regime: Ultrafast studies on the betaines. *J. Chem. Phys.*, 95(6):4188–4194, 1991.

[58] P. F. Barbara, T. J. Meyer, and M. A. Ratner. Contemporary Issues in Electron Transfer Research. *J. Phys. Chem.*, 100(31):13148–13168, jan 1996.

[59] G. Ramakrishna and H. N. Ghosh. Emission from the charge transfer state of xanthene dye-sensitized TiO2 nanoparticles: A new approach to determining back electron transfer rate and verifying the marcus inverted regime. *J. Phys. Chem. B*, 105(29):7000–7008, 2001.

[60] J. S. Kretchmer and T. F. Miller. Tipping the Balance between Concerted versus Sequential Proton-Coupled Electron Transfer. *Inorg. Chem.*, 55(3):1022–1031, feb 2016.

[61] P Song, Y. Li, F. Ma, T. Pullerits, and M. Sun. Photoinduced Electron Transfer in Organic Solar Cells. *Chem. Rec.*, 00:1–20, feb 2016.

[62] A. O. Caldeira and A. J. Leggett. Quantum tunnelling in a dissipative system. *Ann. Phys.*, 149(2):374–456, sep 1983.

[63] A. Leggett, S. Chakravarty, A. Dorsey, M. Fisher, A. Garg, and W. Zwerger. Dynamics of the dissipative two-state system. *Rev. Mod. Phys.*, 59(1):1–85, jan 1987.

[64] S. Chakravarty and A. Leggett. Dynamics of the Two-State System with Ohmic Dissipation. *Phys. Rev. Lett.*, 52(1):5–8, jan 1984.

[65] D. R. Reichman, F. L. H. Brown, and P. Neu. Cumulant expansions and the spin-boson problem. *Phys. Rev. E*, 55(3):2328–2337, mar 1997.

[66] N. Makri. Numerical path integral techniques for long time dynamics of quantum dissipative systems. *J. Math. Phys.*, 36(5):2430, 1995.

[67] N. Makri. Path integral methods. *Enc. Comput. Chem.*, pages 1–17, 1998.

[68] M. Thoss, H. Wang, and W. H. Miller. Self-consistent hybrid approach for complex systems: Application to the spin-boson model with Debye spectral density. *J. Chem. Phys.*, 115(7):2991, 2001.

[69] H. Wang, M. Thoss, and W. H. Miller. Systematic convergence in the dynamical hybrid approach for complex systems: A numerically exact methodology. *J. Chem. Phys.*, 115(7):2979, 2001.

[70] X. Song, H. Wang, and T. Van Voorhis. A Langevin equation approach to electron transfer reactions in the diabatic basis. *J. Chem. Phys.*, 129(14):144502, oct 2008.

[71] A. Ishizaki and Y. Tanimura. Quantum Dynamics of System Strongly Coupled to Low-Temperature Colored Noise Bath: Reduced Hierarchy Equations Approach. *J. Phys. Soc. Jpn.*, 74(12):3131–3134, dec 2005.

[72] Y. Tanimura. Stochastic Liouville, Langevin, Fokker-Planck, and Master Equation Approaches to Quantum Dissipative Systems. *J. Phys. Soc. Jpn.*, 75(8):082001, aug 2006.

[73] J. von Neumann and E. P. Wigner. Uber das Verhalten von Eigenwerten bei adiabatischen Prozessen. *Phys. Z.*, 30:467–470, 1929.

[74] G. A. Worth and L. S. Cederbaum. BEYOND BORN -OPPENHEIMER : Molecular Dynamics Through a Conical Intersection. *Annu. Rev. Phys. Chem.*, 55:127–158, 2004.

[75] B. G. Levine and T. J. Martínez. Isomerization through conical intersections. *Annu. Rev. Phys. Chem.*, 58:613–634, 2007.

[76] B. G. Levine, J. D. Coe, and T. J. Martínez. Optimizing conical intersections without derivative coupling vectors: Application to multistate multireference second-order perturbation theory (MS-CASPT2). *J. Phys. Chem. B*, 112(2):405–413, 2008.

[77] B. Kaduk and T. Van Voorhis. Communication: Conical intersections using constrained density functional theory-configuration interaction. *J. Chem. Phys.*, 133(6):1–5, 2010.

[78] S. Matsika and P. Krause. Nonadiabatic events and conical intersections. *Annu. Rev. Phys. Chem.*, 62:621–643, 2011.

[79] C. Canuel, M. Mons, F. Piuzzi, B. Tardivel, I. Dimicoli, and M. Elhanine. Excited states dynamics of DNA and RNA bases: Characterization of a stepwise deactivation pathway in the gas phase. *J. Chem. Phys.*, 122:074316, 2005.

[80] M. S. de Vries and P. Hobza. Gas-phase spectroscopy of biomolecular building blocks. *Annu. Rev. Phys. Chem.*, 58:585–612, 2007.

[81] J. S. Lim and S. K. Kim. Experimental probing of conical intersection dynamics in the photodissociation of thioanisole. *Nat. Chem.*, 2(8):627–632, 2010.

[82] M. Chachisvilis and A. H. Zewail. Femtosecond Dynamics of Pyridine in the Condensed Phase: Valence Isomerization by Conical Intersections. *J. Phys. Chem. A*, 26:7408–7418, 1999.

[83] A. Toniolo, G. Granucci, and T. J. Martínez. Conical intersections in solution: A QM/MM study using floating occupation semiempirical configuration interaction wave functions. *J. Phys. Chem. A*, 107(19):3822–3830, 2003.

[84] A. Toniolo, S. Olsen, L. Manohar, and T. J. Martínez. Conical intersection dynamics in solution: the chromophore of Green Fluorescent Protein. *Faraday Discuss.*, 127(0):149–163, 2004.

[85] D. Polli, P. Altoè, O. Weingart, K. M. Spillane, C. Manzoni, D. Brida, G. Tomasello, G. Orlandi, P. Kukura, R. A. Mathies, M. Garavelli, and G. Cerullo. Conical intersection dynamics of the primary photoisomerization event in vision. *Nature*, 467(7314):440–443, 2010.

[86] F. Bernardi, M. Olivucci, and M. A. Robb. Potential energy surface crossings in organic photochemistry. *Chem. Soc. Rev.*, 25(5):321–328, 1996.

[87] S. Matsika. Radiationless decay of excited states of uracil through conical intersections. *J. Phys. Chem. A*, 108(37):7584–7590, 2004.

[88] J. K. Norskov, J. Rossmeisl, A. Logadottir, L. Lindqvist, J. R. Kitchin, T. Bligaard, and H. Jónsson. Origin of the Overpotential for Oxygen Reduction at a Fuel-Cell Cathode. *J. Phys. Chem. B*, 108(46):17886–17892, nov 2004.

[89] A. Szabo and N. Ostlund. *Modern Quantum Chemistry*. Dover Publications, Mineola, 1996.

[90] P. Hohenberg and W. Kohn. Inhomogeneous Electron Gas. *Phys. Rev.*, 136(3B):B864–B871, nov 1964.

[91] W. Kohn and L. J. Sham. Self-Consistent Equations Including Exchange and Correlation Effects. *Phys. Rev.*, 140(4A):A1133–A1138, nov 1965.

[92] J. D. Jackson. *Classical Electrodynamics*. Wiley, New York, 3rd edition, jan 1999.

[93] J. P. Perdew and K. Schmidt. Jacob's ladder of density functional approximations for the exchange-correlation energy. *AIP Conference Proceedings*, 577(Density Functional Theory and Its Application to Materials):1–20, 2001.

[94] E. Fermi. Un metodo statistico per la determinazione di alcune prioprieta dell'atome. *Rend. Accad. Naz. Lincei*, 6(6):602–607, 1927.

[95] S. H. Vosko, L. Wilk, and M. Nusair. Accurate spin-dependent electron liquid correlation energies for local spin density calculations: a critical analysis. *Can. J. Phys.*, 58(8):1200–1211, aug 1980.

[96] J. P. Perdew, K. Burke, and M. Ernzerhof. Generalized Gradient Approximation Made Simple. *Phys. Rev. Lett.*, 77(18):3865–3868, oct 1996.

[97] A. D. Becke. Density-functional thermochemistry. III. The role of exact exchange. *J. Chem. Phys.*, 98(7):5648, 1993.

[98] C. Adamo and V. Barone. Toward reliable density functional methods without adjustable parameters: The PBE0 model. *J. Chem. Phys.*, 110(13):6158, 1999.

[99] O. A. Vydrov and T. Van Voorhis. Nonlocal van der Waals density functional: the simpler the better. *J. Chem. Phys.*, 133(24):244103, dec 2010.

[100] C. A. Mead and D. G. Truhlar. Conditions for the definition of a strictly diabatic electronic basis for molecular systems. *J. Chem. Phys.*, 77(12):6090–6098, 1982.

[101] M. Baer and R. Englman. A Study of the Diabatic Electronic Representation within the Born-Oppenheimer Approximation. *Mol. Phys.*, 75(2):293–303, 1992.

[102] Q. Wu and T. Van Voorhis. Direct optimization method to study constrained systems within density-functional theory. *Phys. Rev. A*, 72(2):24502, aug 2005.

[103] Q. Wu and T. Van Voorhis. Direct Calculation of Electron Transfer Parameters through Constrained Density Functional Theory. *J. Phys. Chem. A*, 110(29):9212–9218, 2006.

[104] Q. Wu and T. Van Voorhis. Extracting electron transfer coupling elements from constrained density functional theory. *J. Chem. Phys.*, 125(16):164105, oct 2006.

[105] Q. Wu and T. Van Voorhis. Constrained Density Functional Theory and Its Application in Long-Range Electron Transfer. *J. Chem. Theory Comput.*, 2(3):765–774, may 2006.

[106] Q. Wu, C.-L. Cheng, and T. Van Voorhis. Configuration interaction based on constrained density functional theory: a multireference method. *J. Chem. Phys.*, 127(16):164119, oct 2007.

[107] B. Kaduk, T. Kowalczyk, and T. Van Voorhis. Constrained density functional theory. *Chem. Rev.*, 112:321–370, 2012.

[108] J. Tomasi, B. Mennucci, and R. Cammi. Quantum mechanical continuum solvation models. *Chem. Rev.*, 105(8):2999–3093, 2005.

[109] A. Klamt and G. Schuurmann. COSMO: A new approach to dielectric screening in solvents with explicit expressions for the screening energy and its gradient. *J. Chem. Soc. Perk. T. 2*, 2:799–805, 1993.

[110] M. Cossi, N. Rega, G. Scalmani, and V. Barone. Energies, structures, and electronic properties of molecules in solution with the C-PCM solvation model. *J. Comput. Chem.*, 24(6):669–681, 2003.

[111] Y. Takano and K. N. Houk. Benchmarking the conductor-like polarizable continuum model (CPCM) for aqueous solvation free energies of neutral and ionic organic molecules. *J. Chem. Theory Comput.*, 1(1):70–77, 2005.

[112] C. J. Cramer and D. G. Truhlar. A Universal Approach to Solvation Modeling. *Accounts Chem. Res.*, 41:760–768, 2008.

[113] A. Klamt, B. Mennucci, J. Tomasi, V. Barone, C. Curutchet, M. Orozco, and F. J. Luque. On the Performance of Continuum Solvation Methods. A Comment on "Universal Approaches to Solvation Modeling". *Accounts Chem. Res.*, 42(4):489–492, 2009.

[114] D. Frenkel and B. Smit. *Understanding Molecular Simulation: From Algorithms to Applications*. Academic Press, San Diego, 2nd edition, 2001.

[115] L.-P. Wang, J. Chen, and T. Van Voorhis. Systematic Parametrization of Polarizable Force Fields from Quantum Chemistry Data. *J. Chem. Theory Comput.*, 9(1):452–460, jan 2013.

[116] G. Lamoureux and B. Roux. Modeling induced polarization with classical Drude oscillators: Theory and molecular dynamics simulation algorithm. *J. Chem. Phys.*, 119:3025–3039, 2003.

[117] T. Kowalczyk, L.-P. Wang, and T. Van Voorhis. Simulation of solution phase electron transfer in a compact donor-acceptor dyad. *J. Phys. Chem. B*, 115(42):12135–44, oct 2011.

[118] L.-P. Wang and T. Van Voorhis. A Polarizable QM/MM Explicit Solvent Model for Computational Electrochemistry in Water. *J. Chem. Theory Comput.*, 8(2):610–617, feb 2012.

[119] T. Vreven and K. Morokuma. Hybrid Methods: ONIOM(QM:MM) and QM/MM. *Annu. Rep. Comp. Chem.*, 2:35–51, 2006.

[120] E. Rivera, D. Montemayor, M. Masia, and D. F. Coker. Influence of site-dependent pigment-protein interactions on excitation energy transfer in photosynthetic light harvesting. *J. Phys. Chem. B*, 117(18):5510–5521, may 2013.

[121] A. H. Steindal, K. Ruud, L. Frediani, K. Aidas, and J. Kongsted. Excitation energies in solution: The Fully Polarizable QM/MM/PCM method. *J. Phys. Chem. B*, 115:3027–3037, 2011.

[122] J. J. P. Stewart. *Semiempirical Molecular Orbital Methods*, pages 45–81. John Wiley and Sons, Inc., 2007.

[123] F. Hirata and P. J. Rossky. An extended RISM equation for molecular polar fluids. *Chem. Phys. Lett.*, 83:329–334, 1981.

[124] S. Ten-no, F. Hirata, and S. Kato. A hybrid approach for the solvent effect on the electronic structure of a solute based on the RISM and Hartree-Fock equations. *Chem. Phys. Lett.*, 214:391–396, 1993.

[125] P. E. M. Siegbahn. Structures and energetics for O2 formation in photosystem II. *Acc. Chem. Res.*, 42(12):1871–1880, dec 2009.

[126] J. L. Fillol, Z. Codolà, I. Garcia-Bosch, L. Gómez, J. J. Pla, and M. Costas. Efficient water oxidation catalysts based on readily available iron coordination complexes. *Nat. Chem.*, 3(10):807–13, oct 2011.

[127] K. S. Joya and H. J. M. de Groot. Biomimetic molecular water splitting catalysts for hydrogen generation. *Int. J. Hydrogen Energ.*, 37(10):8787–8799, may 2012.

[128] R. Tagore, R. H. Crabtree, and G. W. Brudvig. Oxygen evolution catalysis by a dimanganese complex and its relation to photosynthetic water oxidation. *Inorg. Chem.*, 47(6):1815–1823, mar 2008.

[129] L.-P. Wang and T. Van Voorhis. Direct-Coupling O2 Bond Forming a Pathway in Cobalt Oxide Water Oxidation Catalysts. *J. Phys. Chem. Lett.*, 2(17):2200–2204, sep 2011.

[130] Y. Surendranath, M. W. Kanan, and D. G. Nocera. Mechanistic studies of the oxygen evolution reaction by a cobalt-phosphate catalyst at neutral pH. *J. Am. Chem. Soc.*, 132(46):16501–16509, nov 2010.

[131] D. K. Bediako, Y. Surendranath, and D. G. Nocera. Mechanistic studies of the oxygen evolution reaction mediated by a nickel-borate thin film electrocatalyst. *J. Am. Chem. Soc.*, 135(9):3662–74, mar 2013.

[132] M. G. Walter, E. L. Warren, J. R. McKone, S. W. Boettcher, Q. Mi, E. A. Santori, and N. S. Lewis. Solar water splitting cells. *Chem. Rev.*, 110(11):6446–6473, nov 2010.

[133] A. Imanishi, T. Okamura, N. Ohashi, R. Nakamura, and Y. Nakato. Mechanism of water photooxidation reaction at atomically flat TiO2 (rutile) (110) and (100) surfaces: dependence on solution pH. *J. Am. Chem. Soc.*, 129(37):11569–78, sep 2007.

[134] P. Sabatier. Hydrogénations et déshydrogénations par catalyse. *Ber. Deut. Chem. Ges.*, 44(3):1984–2001, jul 1911.

[135] J. K. Norskov, T. Bligaard, J. Rossmeisl, and C. H. Christensen. Towards the computational design of solid catalysts. *Nat. Chem.*, 1(1):37–46, apr 2009.

[136] T. A. Betley, Q. Wu, T. Van Voorhis, and D. G. Nocera. Electronic design criteria for O-O bond formation via metal-oxo complexes. *Inorg. Chem.*, 47(6):1849–61, mar 2008.

[137] H. A. Hansen, V. Viswanathan, and J. K. Norskov. Unifying Kinetic and Thermodynamic Analysis of 2 e– and 4 e– Reduction of Oxygen on Metal Surfaces. *J. Phys. Chem. C*, 118(13):6706–6718, mar 2014.

[138] D. Sheppard, G. Henkelman, and O. A. Von Lilienfeld. Alchemical derivatives of reaction energetics. *J. Chem. Phys.*, 133:084104, 2010.

[139] N. Bork, N. Bonanos, J. Rossmeisl, and T. Vegge. Simple descriptors for proton-conducting perovskites from density functional theory. *Phys. Rev. B*, 82(1):1–6, jul 2010.

[140] H Oberhofer and K Reuter. First-principles thermodynamic screening approach to photo-catalytic water splitting with co-catalysts. *J. Chem. Phys.*, 139(4):044710, jul 2013.

[141] A. Vojvodic and J. K. Norskov. Optimizing Perovskites for the Water-Splitting Reaction. *Science*, 334(6061):1355–1356, dec 2011.

[142] J. Suntivich, H. A. Gasteiger, N. Yabuuchi, H. Nakanishi, J. B. Goodenough, and Y. Shao-Horn. Design principles for oxygen-reduction activity on perovskite oxide catalysts for fuel cells and metal-air batteries. *Nat. Chem.*, 3(7):546–50, jul 2011.

[143] J. O. Bockris and T. Otagawa. Mechanism of oxygen evolution on perovskites. *J. Phys. Chem.*, 87(15):2960–2971, jul 1983.

[144] P. Ruetschi and P. Delahay. Influence of Electrode Material on Oxygen Overvoltage - a Theoretical Analysis. *J. Chem. Phys.*, 23(3):556–560, 1955.

[145] J. Rossmeisl, A. Logadottir, and J. K. Norskov. Electrolysis of water on (oxidized) metal surfaces. *Chem. Phys.*, 319(1-3):178–184, dec 2005.

[146] J. Rossmeisl, Z. W. Qu, H. Zhu, G. J. Kroes, and J. K. Norskov. Electrolysis of water on oxide surfaces. *J. Electroanal. Chem.*, 607(1-2):83–89, 2007.

[147] S. Trasatti. Electrocatalysis by oxides - Attempt at a unifying approach. *J. Electroanal. Chem.*, 111(1):125–131, 1980.

[148] B. Zhang, X. Zheng, O. Voznyy, R. Comin, M. Bajdich, M. García-melchor, L. Han, J. Xu, M. Liu, L. Zheng, F. P. G. de Arquer, C. T. Dinh, F. Fan, M. Yuan, E. Yassitepe, N. Chen, T. Regier, P. Liu, Y. Li, P. de Luna, H. L. Xin, H. Yang, A. Vojvodic, and E. H. Sargent. Homogeneously dispersed, multimetal oxygen-evolving catalysts. *Science*, 1525:1–11, 2016.

[149] P. Quaino, F. Juarez, E. Santos, and W. Schmickler. Volcano plots in hydrogen electrocatalysis - uses and abuses. *Beilstein J. Nano.*, 5:846–54, 2014.

[150] M. W. Kanan, Y. Surendranath, and D. G. Nocera. Cobalt-phosphate oxygen-evolving compound. *Chem. Soc. Rev.*, 38(1):109–114, jan 2009.

[151] P. Du, O. Kokhan, K. W. Chapman, P. J. Chupas, and D. M. Tiede. Elucidating the domain structure of the cobalt oxide water splitting catalyst by X-ray pair distribution function analysis. *J. Am. Chem. Soc.*, 134:11096–11099, 2012.

[152] J. M. Mayer. Proton-coupled electron transfer: a reaction chemist's view. *Annu. Rev. Phys. Chem.*, 55(1):363–390, jan 2004.

[153] S. Hammes-Schiffer. Theory of proton-coupled electron transfer in energy conversion processes. *Accounts Chem. Res.*, 42(12):1881–1889, dec 2009.

[154] J. A. Pople, M. Head-Gordon, D. J. Fox, K. Raghavachari, and L. A. Curtiss. Gaussian-1 theory: A general procedure for prediction of molecular energies. *J. Chem. Phys.*, 90(10):5622, 1989.

[155] L. A. Curtiss, K. Raghavachari, P. C. Redfern, and J. A. Pople. Assessment of Gaussian-2 and density functional theories for the computation of enthalpies of formation. *J. Chem. Phys.*, 106(3):1063, 1997.

[156] G. D. Hawkins, C. J. Cramer, and D. G. Truhlar. Universal Quantum Mechanical Model for Solvation Free Energies Based on Gas-Phase Geometries. *J. Phys. Chem. B*, 5639(97):3257–3271, 1998.

[157] R. C. Rizzo, T. Aynechi, D.A. Case, and I. D. Kuntz. Estimation of Absolute Free Energies of Hydration Using Continuum Methods: Accuracy of Partial Charge Models and Optimization of Nonpolar Contributions. *J. Chem. Theory Comput.*, 2(1):128–139, jan 2006.

[158] X. F. Yang and M. H. Baik.

[159] X. F. Yang and M. H. Baik. cis,cis-$[(bpy)_2Ru^{V}O]_2O^{4+}$ Catalyzes Water Oxidation Formally via in Situ Generation of Radicaloid Ru^{IV}-O·. *J. Am. Chem. Soc.*, 128:7476–7485, 2006.

[160] X. F. Yang and M. H. Baik. The Mechanism of Water Oxidation Catalysis Promoted by $[tpyRu(IV)=O]_2L^{3+}$: A Computational Study. *J. Am. Chem. Soc.*, 130:16231–16240, 2008.

[161] L. A. Curtiss, K. Raghavachari, G. W. Trucks, and J. A. Pople. Gaussian-2 theory for molecular energies of first- and second-row compounds. *J. Chem. Phys.*, 94(11):7221, 1991.

[162] C. A. Jiménez-Hoyos, B. G. Janesko, and G. E. Scuseria. Evaluation of range-separated hybrid density functionals for the prediction of vibrational frequencies, infrared intensities, and Raman activities. *Phys. Chem. Chem. Phys.*, 10(44):6621–9, nov 2008.

[163] M. W. Chase. *NIST-JANAF Thermochemical Tables*. American Institute of Physics, Woodbury, New York, 4th edition, 1998.

[164] J. N. Harvey. DFT Computation of Relative Spin-State Energetics of Transition Metal Compounds. *STruct. Bond.*, 112:151–183, 2004.

[165] C. J. Cramer and D. G. Truhlar. Density functional theory for transition metals and transition metal chemistry. *Phys. Chem. Chem. Phys.*, 11(46):10757–10816, dec 2009.

[166] M. Swart. Metal–ligand bonding in metallocenes: Differentiation between spin state, electrostatic and covalent bonding. *Inorg. Chim. Acta*, 360(1):179–189, jan 2007.

[167] T. F. Hughes and R. A. Friesner. Development of Accurate DFT Methods for Computing Redox Potentials of Transition Metal Complexes: Results for Model Complexes and Application to Cytochrome P450. *J. Chem. Theory Comput.*, 8(2):442–459, feb 2012.

[168] M W Palascak and G C Shields. Accurate Experimental Values for the Free Energies of Hydration of H+, OH-, and H3O+. *J. Phys. Chem. A*, 108(16):3692–3694, 2004.

[169] D. M. Camaioni and C. A. Schwerdtfeger. Comment on "Accurate experimental values for the free energies of hydration of H+, OH-, and H3O+". *J. Phys. Chem. A*, 109(47):10795–7, dec 2005.

[170] C. P. Kelly, C. J. Cramer, and D. G. Truhlar. Aqueous solvation free energies of ions and ion-water clusters based on an accurate value for the absolute aqueous solvation free energy of the proton. *J. Phys. Chem. B*, 110(32):16066–16081, aug 2006.

[171] S. J. Konezny, M. D. Doherty, O. R. Luca, R. H. Crabtree, G. L. Soloveichik, and V. S. Batista. Reduction of Systematic Uncertainty in DFT Redox Potentials of Transition-Metal Complexes. *J. Phys. Chem. C*, 116(10):6349–6356, mar 2012.

[172] Y. Shao, Z. Gan, E. Epifanovsky, A. T. B. Gilbert, M. Wormit, J. Kussmann, A. W. Lange, A. Behn, J. Deng, X. Feng, D. Ghosh, M. Goldey, P. R. Horn, L. D. Jacobson, I. Kaliman, R. Z. Khaliullin, T. Kus, A. Landau, J. Liu, E. I. Proynov, Y. M. Rhee, R. M. Richard, M. A. Rohrdanz, R. P. Steele, E. J. Sundstrom, H. L. Woodcock, P. M. Zimmerman, D. Z. B. Albrecht, E. Alguire, B. Austin, G. J. O. Beran, Y. A. Bernard, E. Berquist, K. Brandhorst, K. B. Bravaya, S. T. Brown, D. Casanova, C.-M. Chang, Y. Chen, S. H. Chien, K. D. Closser, D. L. Crittenden, M. Diedenhofen, R. A. DiStasio, H. Do, A. D. Dutoi, R. G. Edgar, S. Fatehi, L. Fusti-Molnar, A. Ghysels, A. Golubeva-Zadorozhnaya, J. Gomes, M. W. D. Hanson-Heine, P. H. P. Harbach, A. W. Hauser, E. G. Hohenstein, Z. C. Holden, T.-C. Jagau, H. Ji, B. Kaduk, K. Khistyaev, J. Kim, R. a. King, P. Klunzinger, D. Kosenkov, T. Kowalczyk, C. M. Krauter, K. U. Lao, A. Laurent, K. V. Lawler, S. V. Levchenko, C. Y. Lin, F. Liu, E. Livshits, R. C. Lochan, A. Luenser, P. Manohar, S. F. Manzer, S.-P. Mao, N. Mardirossian, A. V. Marenich, S. A. Maurer, N. J. Mayhall, C. M. Oana, R. Olivares-Amaya, D. P. O'Neill, J. A. Parkhill, T. M. Perrine, R. Peverati, A. Prociuk, D. R. Rehn, E. Rosta, N. J. Russ, S. M. Sharada, S. Sharma, D. W. Small, A. Sodt, T. Stein, D. Stück, Y.-C. Su, A. J. W. Thom, T. Tsuchimochi, V. Vanovschi, L. Vogt, O. Vydrov, T. Wang, M. A. Watson, J. Wenzel, A. White, C. F. Williams, S. Yeganeh, S. R. Yost, Z.-Q. You, I. Y. Zhang, X. Zhang, Y. Zhao, B. R. Brooks, G. K. L. Chan, D. M. Chipman, C. J. Cramer, W. A. Goddard, M. S. Gordon, W. J. Hehre, A. Klamt, H. F. Schaefer, M. W. Schmidt, C. D. Sherrill, D. G. Truhlar, A. Warshel, X. Xuaf, A. Aspuru-Guzik, R. Baer, A. T. Bell, N. A. Besley, J.-D. Chai, A. Dreuw, B. D. Dunietz, T. R. Furlani, S. R. Gwaltney, C.-P. Hsu, Y. Jung, J. Kong, D. S. Lambrecht, W. Liang, C. Ochsenfeld, V. A. Rassolov, L. V. Slipchenko, J. E. Subotnik, T. Van Voorhis, J. M. Herbert, A. I. Krylov, P. M. W. Gill, and M. Head-Gordon. Advances in Molecular Quantum Chemistry Contained in the Q-Chem 4 Program Package. *Mol. Phys.*, 113(2):37–41, 2014.

[173] D. R. Lide. *CRC Handbook of Chemistry and Physics, 88th Edition (CRC Handbook of Chemistry & Physics)*. CRC Press, 88 edition, jun 2007.

[174] A. Bondi. Van der Waals Volumes and Radii. *J. Phys. Chem.*, 68(3):441–451, mar 1964.

[175] S. S. Batsanov. Van der Waals Radii of Elements. *Inorg. Mater.*, 37(9):871–885, 2001.

[176] M. T. M. Koper. Thermodynamic theory of multi-electron transfer reactions: Implications for electrocatalysis. *J. Electroanal. Chem.*, 660(2):254–260, sep 2011.

[177] X. Liu and F. Wang. Transition metal complexes that catalyze oxygen formation from water: 1979–2010. *Coordin. Chem. Rev.*, 256:1115–1136, 2012.

[178] J. J Concepcion, M.-K. Tsai, J. T. Muckerman, and T. J. Meyer. Mechanism of water oxidation by single-site ruthenium complex catalysts. *J. Am. Chem. Soc.*, 132(5):1545–1557, feb 2010.

[179] X. Yang and M. B. Hall. Mechanism of water splitting and oxygen-oxygen bond formation by a mononuclear ruthenium complex. *J. Am. Chem. Soc.*, 132(1):120–30, jan 2010.

[180] A. Fujishima, T. N. Rao, and D. A. Tryk. Titanium dioxide photocatalysis. *J. Photoch. Photobio. C*, 1(1):1–21, 2000.

[181] C. C. L. McCrory, S. Jung, J. C. Peters, and T. F. Jaramillo. Benchmarking heterogeneous electrocatalysts for the oxygen evolution reaction. *J. Am. Chem. Soc.*, 135(45):16977–16987, 2013.

[182] J. Law and I. T. Jolliffe. Principal Component Analysis. *Statistician*, 36(4):432, 1987.

[183] M. W. Kanan, J. Yano, Y. Surendranath, M. Dinca, V. K. Yachandra, and D. G. Nocera. Structure and valency of a cobalt-phosphate water oxidation catalyst determined by in situ X-ray spectroscopy. *J. Am. Chem. Soc.*, 132:13692–13701, 2010.

[184] L. Li, C. Li, Z. Zhang, and E. Alexov. On the Dielectric "Constant" of Proteins: Smooth Dielectric Function for Macromolecular Modeling and Its Implementation in DelPhi. *J. Chem. Theory Comput.*, 9(4):2126–2136, apr 2013.

[185] G. Mattioli, M. Risch, A. A. Bonapasta, H. Dau, and L. Guidoni. Protonation states in a cobalt-oxide catalyst for water oxidation: fine comparison of {\em ab initio} molecular dynamics and X-ray absorption spectroscopy results. *Phys. Chem. Chem. Phys.*, 13:15437–15441, 2011.

[186] X. C. Zeng, H. Hu, X. Q. Hu, and W. Yang. Calculating solution redox free energies with ab initio quantum mechanical/molecular mechanical minimum free energy path method. *J. Chem. Phys.*, 130:164111, 2009.

[187] I. Chiorescu, D. V. Deubel, V. B. Arion, and B. K. Keppler. Computational electrochemistry of ruthenium anticancer agents. Unprecedented benchmarking of implicit solvation models. *J. Chem. Theory Comput.*, 4:499–506, 2008.

[188] D. J. Tannor, B. Marten, R. Murphy, R. A. Friesner, D. Sitkoff, A. Nicholls, B. Honig, M. Ringnalda, and W.˜A. Goddard III. Accurate first principles calculation of molecular charge distributions and solvation energies from ab initio quantum mechanics and continuum dielectric theory. *J. Am. Chem. Soc.*, 116:11875–11882, 1994.

[189] G. Mattioli, P. Giannozzi, A. A. Bonapasta, and L. Guidoni. Reaction pathways for oxygen evolution promoted by cobalt catalyst. *J. Am. Chem. Soc.*, 135:15353–15363, 2013.

[190] A. Schaefer, C. Huber, and R. Ahlrichs. Fully optimized contracted Gaussian-basis sets of triple zeta valence quality for atoms Li to Kr. *J. Chem. Phys.*, 100:5829–5835, 1994.

[191] H. J. C. Berendsen, J. R. Grigera, and T. P. Straatsma. The Missing Term in Effective Pair Potentials. *J. Phys. Chem.*, 91(24):6269–6271, 1987.

[192] J. Aaqvist, A. Warshel, and J. Aqvist. Simulation of enzyme reactions using valence bond force fields and other hybrid quantum/classical approaches. *Chem. Rev.*, 93(7):2523–2544, 1993.

[193] A. K. Rappe, C. J. Casewit, K. S. Colwell, W. A. Goddard III, and W. M. Skiff. UFF, a full periodic table force field for molecular mechanics and molecular dynamics simulations. *J. Am. Chem. Soc.*, 114:10024–10035, 1992.

[194] H. L. Woodcock, M. Hodoscek, A. T. B. Gilbert, P. M. W. Gill, H. F. Schaefer, and B. R. Brooks. Interfacing Q-Chem and CHARMM to perform QM/MM reaction path calculations. *J. Comput. Chem.*, 28(9):1485–502, jul 2007.

[195] J. P. Ryckaert, G. Ciccotti, and H. J. C. Berendsen. Numerical integration of the cartesian equations of motion of a system with constraints: molecular dynamics of n-alkanes. *J. Comput. Phys.*, 23(3):327–341, 1977.

[196] M. Neumann. Dielectric relaxation in water. Computer simulations with the TIP4P potential. *J. Chem. Phys.*, 85:1567, 1986.

[197] R. P. Feynman and F. L. Vernon. The Theory of a General Quantum System Interacting with a Linear Dissipative System. *Ann. Phys.*, 173:118–173, 1963.

[198] J. C. Tully. Mixed quantum-classical dynamics. *Faraday Discuss.*, 110:407–419, 1998.

[199] R. Kapral and G. Ciccotti. Mixed quantum-classical dynamics. *J. Chem. Phys.*, 110(18):8919, 1999.

[200] P. Pechukas. Time-Dependent Semiclassical Scattering Theory. II. Atomic Collisions. *Phys. Rev.*, 181(1):174–185, may 1969.

[201] H.-D. Meyer, U. Manthe, and L.S. Cederbaum. The multi-configurational time-dependent Hartree approach. *Chem. Phys. Lett.*, 165(1):73–78, jan 1990.

[202] U. Manthe, H.-D. Meyer, and L. S. Cederbaum. Wave-packet dynamics within the multiconfiguration Hartree framework: General aspects and application to NOCl. *J. Chem. Phys.*, 97(5):3199, 1992.

[203] M. H. Beck, A. Jackle, G. A. Worth, and H.-D. Meyer. The multiconfiguration time-dependent Hartree (MCTDH) method: a highly efficient algorithm for propagating wavepackets. *Phys. Rep.*, 324(1):1–105, jan 2000.

[204] J. M. Moix and J. Cao. A hybrid stochastic hierarchy equations of motion approach to treat the low temperature dynamics of non-Markovian open quantum systems. *J. Chem. Phys.*, 139(13):134106, oct 2013.

[205] A. G. Redfield. The Theory of Relaxation Processes. In John S. Waugh, editor, *Adv. Magn. Reson.*, pages 1–32. Academic Press, 1965.

[206] J. M. Jean, R. A. Friesner, and G. R. Fleming. Application of a multilevel Redfield theory to electron transfer in condensed phases. *J. Chem. Phys.*, 96(8):5827, 1992.

[207] T. Holstein. Studies of polaron motion. *Ann. Phys. (New York)*, 8(3):325–342, nov 1959.

[208] C. Aslangul, N. Pottier, and D. Saint-James. Quantum ohmic dissipation : coherence vs. incoherence and symmetry-breaking. a simple dynamical approach. *J. Phys. (Paris)*, 46(12):2031–2045, 1985.

[209] C. Aslangul, N. Pottier, and D. Saint-James. Quantum ohmic dissipation: Transition from coherent to incoherent dynamics. *Phys. Lett. A*, 110(5):249–252, jul 1985.

[210] R. A. Harris and R. Silbey. Variational calculation of the tunneling system interacting with a heat bath. II. Dynamics of an asymmetric tunneling system. *J. Chem. Phys.*, 83(3):1069, 1985.

[211] R. Silbey and R. A. Harris. Variational calculation of the dynamics of a two level system interacting with a bath. *The Journal of Chemical Physics*, 80(6):2615, 1984.

[212] R. Silbey and R. A. Harris. Tunneling of molecules in low-temperature media: an elementary description. *The Journal of Physical Chemistry*, 93(20):7062–7071, oct 1989.

[213] S. Jang, Y.-C. Cheng, D. R. Reichman, and J. D. Eaves. Theory of coherent resonance energy transfer. *J. Chem. Phys.*, 129(10):101104, sep 2008.

[214] A. Nazir, D. P. S. McCutcheon, and A. W. Chin. Ground state and dynamics of the biased dissipative two-state system: Beyond variational polaron theory. *Phys. Rev. B*, 85(22):224301, jun 2012.

[215] J. Cao. Effects of bath relaxation on dissipative two-state dynamics. *J. Chem. Phys.*, 112(15):6719, 2000.

[216] S. Jang, J. Cao, and R. J. Silbey. Fourth-order quantum master equation and its Markovian bath limit. *J. Chem. Phys.*, 116(7):2705, 2002.

[217] J. Wu and J. Cao. Higher-order kinetic expansion of quantum dissipative dynamics: mapping quantum networks to kinetic networks. *J. Chem. Phys.*, 139(4):044102, jul 2013.

[218] M. Sparpaglione and S. Mukamel. Dielectric friction and the transition from adiabatic to nonadiabatic electron transfer. I. Solvation dynamics in Liouville space. *J. Chem. Phys.*, 88(5):3263, 1988.

[219] M. Cho and R. J. Silbey. On the transition from nonadiabatic to adiabatic rate kernel: Schwinger's stationary variational principle and Padé approximation. *J. Chem. Phys.*, 106(7):2654, 1997.

[220] D. R. Reichman and R. J. Silbey. On the relaxation of a two-level system: Beyond the weak-coupling approximation. *J. Chem. Phys.*, 104(4):1506, 1996.

[221] D. Reichman, R. J. Silbey, and A. Suarez. On the nonperturbative theory of pure dephasing in condensed phases at low temperatures. *J. Chem. Phys.*, 105(23):10500, 1996.

[222] B. B. Laird, J. Budimir, and J. L. Skinner. Quantum-mechanical derivation of the Bloch equations: Beyond the weak-coupling limit. *J. Chem. Phys.*, 94(6):4391, 1991.

[223] R. Zwanzig. Ensemble Method in the Theory of Irreversibility. *J. Chem. Phys.*, 33(5):1338, 1960.

[224] R. Zwanzig. Memory Effects in Irreversible Thermodynamics. *Phys. Rev.*, 124(4):983–992, nov 1961.

[225] R. Zwanzig. On the identity of three generalized master equations. *Physica*, 30(6):1109–1123, jun 1964.

[226] F. Dyson. Divergence of Perturbation Theory in Quantum Electrodynamics. *Phys. Rev.*, 85(4):631–632, feb 1952.

[227] J. Fischer. The Use of Power Expansions in Quantum Field Theory. *Int. J. Mod. Phys. A*, 12(21):3625–3663, aug 1997.

[228] U. D. Jentschura, J. Becher, E. J. Weniger, and G. Soff. Resummation of QED perturbation series by sequence transformations and the prediction of perturbative coefficients. *Phys. Rev. Lett.*, 85(12):2446–2449, sep 2000.

[229] J. O. Andersen and M. Strickland. Resummation in hot field theories. *Ann. Phys. (New York)*, 317(2):281–353, jun 2005.

[230] E. Caliceti, M. Meyer-Hermann, P. Ribeca, A. Surzhykov, and U. D. Jentschura. From useful algorithms for slowly convergent series to physical predictions based on divergent perturbative expansions. *Phys. Rep.*, 446(1-3):1–96, jul 2007.

[231] R. Bartlett and M. Musial. Coupled-cluster theory in quantum chemistry. *Rev. Mod. Phys.*, 79(1):291–352, feb 2007.

[232] Q. Shi and E. Geva. A new approach to calculating the memory kernel of the generalized quantum master equation for an arbitrary system–bath coupling. *J. Chem. Phys.*, 119(23):12063, 2003.

[233] M.-L. Zhang, B. J. Ka, and E. Geva. Nonequilibrium quantum dynamics in the condensed phase via the generalized quantum master equation. *J. Chem. Phys.*, 125(4):44106, jul 2006.

[234] G. A. Baker and P. Graves-Morris. *Padé Approximants*. Cambridge University Press, New York, 1996.

[235] B. Lippmann and J. Schwinger. Variational Principles for Scattering Processes. I. *Phys. Rev.*, 79(3):469–480, aug 1950.

[236] L. D. Zusman. Outer-sphere electron transfer in polar solvents. *Chem. Phys.*, 49(2):295–304, jul 1980.

[237] A. A. Golosov and D. R. Reichman. Reference system master equation approaches to condensed phase charge transfer processes. I. General formulation. *J. Chem. Phys.*, 115(21):9848, 2001.

[238] A. A. Golosov and D. R. Reichman. Reference system master equation approaches to condensed phase charge transfer processes. II. Numerical tests and applications to the study of photoinduced charge transfer reactions. *J. Chem. Phys.*, 115(21):9862, 2001.

[239] H. Sumi. Energy Transfer between Localized Electronic States – From Non-Adiabatic to Adiabatic Hopping Limits –. *J. Phys. Soc. Jpn.*, 49(5):1701–1712, may 1980.

[240] H.-T. Chen, T. C. Berkelback, and D. R. Reichman. On the accuracy of the Padé-resummed master equation approach to dissipative quantum dynamics. *J. Chem. Phys.*, 144:154106, 2016.

[241] D. Thirumalai, E. J. Bruskin, and B. J. Berne. An iterative scheme for the evaluation of discretized path integrals. *J. Chem. Phys.*, 79(10):5063, 1983.

[242] B. J. Berne and D. Thirumalai. On the Simulation of Quantum Systems: Path Integral Methods. *Annu. Rev. Phys. Chem.*, 37(1):401–424, oct 1986.

[243] T. A. Burton. *Volterra Integral and Differential Equations*. Elsevier, 2nd edition, 2005.

[244] H. Liu, L. Zhu, S. Bai, and Q. Shi. Reduced quantum dynamics with arbitrary bath spectral densities: hierarchical equations of motion based on several different bath decomposition schemes. *J. Chem. Phys.*, 140(13):134106, apr 2014.

[245] D. Chandler. Electron transfer in water and other polar environments, how it happens. In B. J. Berne, G. Ciccotti, and D. F. Coker, editors, *Classical and Quantum Dynamics in Condensed Phase Simulations*, chapter 2, pages 25–49. World Scientific, Singapore, 1998.

[246] Q. Shi and E. Geva. A semiclassical generalized quantum master equation for an arbitrary system-bath coupling. *J. Chem. Phys.*, 120(22):10647–10658, jun 2004.

[247] J. L. Skinner. Semiclassical approximations to golden rule rate constants. *J. Chem. Phys.*, 107(20):8717, 1997.

[248] S. A. Egorov and J. L. Skinner. Semiclassical approximations to quantum time correlation functions. *Chem. Phys. Lett.*, 293(5-6):469–476, sep 1998.

[249] S. Valleau, A. Eisfeld, and A. Aspuru-Guzik. On the alternatives for bath correlators and spectral densities from mixed quantum-classical simulations. *J. Chem. Phys.*, 137(22):224103, dec 2012.

[250] M. G. Mavros and T. Van Voorhis. Resummed memory kernels in generalized system-bath master equations. *J. Chem. Phys.*, 141(5):054112, aug 2014.

[251] R. A. Kuharski, J. S. Bader, D. Chandler, M. Sprik, M. L. Klein, and R. W. Impey. Molecular model for aqueous ferrous–ferric electron transfer. *J. Chem. Phys.*, 89(5):3248, 1988.

[252] J. S. Bader and D. Chandler. Computer simulation of photochemically induced electron transfer. *Chem. Phys. Lett.*, 157(6):501–504, may 1989.

[253] J. S. Bader, R. A. Kuharski, and D. Chandler. Role of nuclear tunneling in aqueous ferrous–ferric electron transfer. *J. Chem. Phys.*, 93(1):230, 1990.

[254] K. Ando. Quantum energy gap law of outer-sphere electron transfer reactions: A molecular dynamics study on aqueous solution. *J. Chem. Phys.*, 106(1):116, 1997.

[255] K. Ando. Solvent nuclear quantum effects in electron transfer reactions. III. Metal ions in water. Solute size and ligand effects. *J. Chem. Phys.*, 114(21):9470, 2001.

[256] K. M. Rosso, D. M. A. Smith, and M. Dupuis. Aspects of aqueous iron and manganese (II/III) self-exchange electron transfer reactions. *J. Phys. Chem. A*, 108:5242–5248, 2004.

[257] Agostino Migliore and Michael L Klein. Systems Using DFT : Application to the Hexa-Aquo Ferric - Ferrous Redox Couple. *J. Chem. Theory Comput.*, 5:307–323, 2009.

[258] C. Drechsel-Grau and M. Sprik. Activation energy for a model ferrous-ferric half reaction from transition path sampling. *J. Chem. Phys.*, 136(3):034506, jan 2012.

[259] P. Zarzycki, S. Kerisit, and K. Rosso. Computational methods for intramolecular electron transfer in a ferrous-ferric iron complex. *J. Colloid Interf. Sci.*, 361(1):293–306, sep 2011.

[260] R. L. Fulton and M. Gouterman. Vibronic Coupling. I. Mathematical Treatment for Two Electronic States. *J. Chem. Phys.*, 35(3):1059, 1961.

[261] R. D. Coalson and D. G. Evans. Condensed phase vibrational relaxation: calibration of approximate relaxation theories with analytical and numerically exact results. *Chem. Phys.*, 296(2-3):117–127, jan 2004.

[262] S. Jang and M. D. Newton. Theory of torsional non-Condon electron transfer: A generalized spin-boson Hamiltonian and its nonadiabatic limit solution. *J. Chem. Phys.*, 122(2), 2005.

[263] A. F. Izmaylov, D. Mendive-Tapia, M. J. Bearpark, M. A. Robb, J. C. Tully, and M. J. Frisch. Nonequilibrium Fermi golden rule for electronic transitions through conical intersections. *J. Chem. Phys.*, 135(2011), 2011.

[264] R. Borrelli and A. Peluso. Quantum Dynamics of Radiationless Electronic Transitions Including Normal Modes Displacements and Duschinsky Rotations: A Second-Order Cumulant Approach. *J. Chem. Theory Comput.*, 11(2):415–422, feb 2015.

[265] Z. Gong, Z. Tang, S. Mukamel, J. Cao, and J. Wu. A continued fraction resummation form of bath relaxation effect in the spin-boson model. *J. Chem. Phys.*, 142(8):084103, 2015.

[266] W. R. Cook, D. G. Evans, and R. D. Coalson. Exact solution of a model of condensed-phase electron transfer with non-Condon effects. *Chem. Phys. Lett.*, 420(4-6):362–366, mar 2006.

[267] Y. Dahnovsky. Modulating electron dynamics: Modified spin-boson approach. *Phys. Rev. B*, 73(14):1–9, 2006.

[268] W. R. Cook, R. D. Coalson, and D. G. Evans. Effectiveness of perturbation theory approaches for computing non-condon electron transfer dynamics in condensed phases. *J. Phys. Chem. B*, 113(33):11437–11447, aug 2009.

[269] Y. Zhao, Y. Yao, and V. Chernyak. Communication: Spin-boson model with diagonal and off-diagonal coupling to two independent baths: Ground-state phase transition in the deep sub-Ohmic regime. *J. Chem. Phys.*, 140(16):161105, apr 2014.

[270] B. Hess, C. Kutzner, D. Van Der Spoel, and E. Lindahl. GROMACS 4: Algorithms for highly efficient, load-balanced, and scalable molecular simulation. *J. Chem. Theory Comput.*, 4(3):435–447, 2008.

[271] W. L. Jorgensen, J. Chandrasekhar, J. D. Madura, R. W. Impey, and M. L. Klein. Comparison of simple potential functions for simulating liquid water. *J. Chem. Phys.*, 79(2):926, 1983.

[272] T. Darden, D. York, and L. Pedersen. Particle mesh Ewald: An N log(N) method for Ewald sums in large systems. *J. Chem. Phys*, 98(12):10089–10092, 1993.

[273] I. G. Tironi, R. Sperb, P. E. Smith, and W. F. Van Gunsteren. A generalized reaction field method for molecular dynamics simulations. *J. Chem. Phys.*, 102(13):5451–5459, 1995.

[274] M. G. Mavros, D. Hait, and T. Van Voorhis. Condensed Phase Electron Transfer Beyond the Condon Approximation. *J. Chem. Phys.*, Submitted, 2016.

[275] A. Jarzecki, A. Anbar, and T. Spiro. DFT analysis of Fe(H2O)$_6 ^{3+}$ and Fe(H2O)$_6 ^{2+}$ structure and vibrations; implications for isotope fractionation. *J. Phys. Chem. A*, 108(14):2726–2732, 2004.

[276] S. A. Welch, B. L. Beard, C. M. Johnson, and P. S. Braterman. Kinetic and equilibrium Fe isotope fractionation between aqueous Fe(II) and Fe(III). *Geochim. Cosmochim. Ac.*, 67(22):4231–4250, 2003.

[277] P. Sit, M. Cococcioni, and N. Marzari. Realistic Quantitative Descriptions of Electron Transfer Reactions: Diabatic Free-Energy Surfaces from First-Principles Molecular Dynamics. *Phys. Rev. Lett.*, 97(2):028303, jul 2006.

[278] R. P. Matthews and K. J. Naidoo. Experimentally consistent ion association predicted for metal solutions from free energy simulations. *J. Phys. Chem. B*, 114:7286–7293, 2010.

[279] A. Warshel, M. Kato, and A. V. Pisliakov. Polarizable force fields: History, test cases, and prospects. *J. Chem. Theory Comput.*, 3(6):2034–2045, 2007.

[280] S. Hammes-Schiffer and J. C. Tully. Proton transfer in solution: Molecular dynamics with quantum transitions. *J. Chem. Phys.*, 101(6):4657, 1994.

[281] A. Warshel and R. M. Weiss. An empirical valence bond approach for comparing reactions in solutions and in enzymes. *J. Am. Chem. Soc.*, 102(20):6218–6226, 1980.

[282] R. S. Mulliken. Molecular Compounds and their Spectra. II. *J. Am. Chem. Soc.*, 64:811, 1952.

[283] N. S. Hush. Intervalence-Transfer Absorption. Part 2. Theoretical Considerations and Spectroscopic Data. *Prog. Inorg. Chem.*, 8:391, 1967.

[284] R. J. Cave and M. D. Newton. Generalization of the Mulliken-Hush treatment for the calculation of electron transfer matrix elements. *Chem. Phys. Lett.*, 249(1-2):15–19, 1996.

[285] O. V. Prezhdo, J. T. Kindt, and J. C. Tully. Perturbed ground state method for electron transfer. *J. Chem. Phys.*, 111(17):7818–7827, 1999.

[286] A. A. Voityuk and N. Rösch. Fragment charge difference method for estimating donor-acceptor electronic coupling: Application to DNA π-stacks. *J. Chem. Phys.*, 117(12):5607–5616, 2002.

[287] S.-J. Lee, H.-C. Chen, Z.-Q. You, K.-L. Liu, T. J. Chow, I-C. Chen, and C.-P. Hsu. Theoretical characterization of photoinduced electron transfer in rigidly linked donor-acceptor molecules: the fragment charge difference and the generalized Mulliken-Hush schemes. *Mol. Phys.*, 108(19-20):2775–2789, 2010.

[288] Q. Wu, B. Kaduk, and T. Van Voorhis. Constrained density functional theory based configuration interaction improves the prediction of reaction barrier heights. *J. Chem. Phys.*, 130(3):34109, 2009.

[289] B. Kaduk, T. Tsuchimochi, and T. Van Voorhis. Analytic energy gradients for constrained DFT-configuration interaction. *J. Chem. Phys.*, 140(18):18A503, may 2014.

[290] A. Kubas, F. Hoffmann, A. Heck, H. Oberhofer, M. Elstner, and J. Blumberger. Electronic couplings for molecular charge transfer: benchmarking CDFT, FODFT, and FODFTB against high-level ab initio calculations. *J. Chem. Phys.*, 140(10):104105, mar 2014.

[291] R. J. Cave and M. D. Newton. Calculation of electronic coupling matrix elements for ground and excited state electron transfer reactions: Comparison of the generalized Mulliken–Hush and block diagonalization methods. *J. Chem. Phys.*, 106(22):9213, 1997.

[292] M. D. Newton. Electronic structure analysis of electron-transfer matrix elements for transition-metal redox pairs. *J. Phys. Chem.*, 92(11):3049–3056, 1988.

[293] J. P. Perdew, R. G. Parr, M. Levy, and J. L. Balduz. Density-Functional Theory for Fractional Particle Number: Derivative Discontinuities of the Energy. *Phys. Rev. Lett.*, 49(23):1691–1694, dec 1982.

[294] A. J. Cohen, P. Mori-Sánchez, and W. Yang. Fractional spins and static correlation error in density functional theory. *J. Chem. Phys*, 129:121104, 2008.

[295] P. Mori-Sánchez, A. J. Cohen, and W. Yang. Discontinuous nature of the exchange-correlation functional in strongly correlated systems. *Phys. Rev. Lett.*, 102(6):1–4, 2009.

[296] C. Li, X. Zheng, A. J. Cohen, P. Mori-Sánchez, and W. Yang. Local scaling correlation for reducing delocalization error in density functional approximations. *Phys. Rev. Lett.*, 114:053001, 2015.

[297] G. Hautier, C. C. Fischer, A. Jain, T. Mueller, and G. Ceder. Finding nature's missing ternary oxide compounds using machine learning and density functional theory. *Chem. Mater.*, 22:3762–3767, 2010.

[298] I. Y. Kanal, S. G. Owens, J. S. Bechtel, and G. R. Hutchison. Efficient computational screening of organic polymer photovoltaics. *J. Phys. Chem. Lett.*, 4:1613–1623, 2013.

[299] N. B. Halck, V. Petrykin, P. Krtil, and J. Rossmeisl. Beyond the volcano limitations in electrocatalysis - oxygen evolution reaction. *Phys. Chem. Chem. Phys.*, 16:13682–13688, 2014.

[300] M. A. Robb, F. Bernardi, and M. Olivucci. Conical intersections as a mechanistic feature of organic photochemistry. *Pure Appl. Chem.*, 67(5):783–789, 1995.

[301] D. A. Horke, Q. Li, L. Blancafort, and J. R. R. Verlet. Ultrafast above-threshold dynamics of the radical anion of a prototypical quinone electron-acceptor. *Nat. Chem.*, 5(8):711–717, 2013.

[302] A. J. Musser, M. Liebel, C. Schnedermann, T. Wende, T. B. Kehoe, A. Rao, and P. Kukura. Evidence for conical intersection dynamics mediating ultrafast singlet exciton fission. *Nat. Phys.*, 11(4):352–357, 2015.

[303] T. Fukushima, W. Drisdell, J. Yano, and Y. Surendranath. Graphite-Conjugated Pyrazines as Molecularly Tunable Heterogeneous Electrocatalysts. *J. Am. Chem. Soc.*, 137(34):10926–10929, 2015.

[304] J. R. Sheats, H. Antoniadis, M. Hueschen, W. Leonard, J. Miller, R. Moon, D. Roitman, and A. Stocking. Organic Electroluminescent Devices. *Science*, 273(5277):884–888, 1996.

[305] P. R. Callis and J. T. Vivian. Understanding the variable fluorescence quantum yield of tryptophan in proteins using QM-MM simulations. Quenching by charge transfer to the peptide backbone. *Chem. Phys. Lett.*, 369(3-4):409–414, 2003.

[306] D. N. Congreve, J. Lee, N. J. Thompson, E. Hontz, S. R. Yost, P. D. Reusswig, M. E. Bahlke, S. Reineke, T. Van Voorhis, and M. A. Baldo. External Quantum Efficiency Above 100% in a Singlet-Exciton-Fission–Based Organic Photovoltaic Cell. *Science*, 340:334–337, 2013.

[307] H. Goldstein. *Classical Mechanics*. Addison-Wesley Publishing Company, Reading, MA, 2nd edition, 1980.

[308] E. J. Heller. Frozen Gaussians: A very simple semiclassical approximation. *J. Chem. Phys.*, 75(6):2923–2931, 1981.